EIE лектротехніка і лектромеханіка

Electrical Engineering & Electromechanics

Електричні машини та апарати
Електротехнічні комплекси та системи
Силова електроніка
Теоретична електротехніка
Техніка сильних електричних та магнітних полів.
    Інженерна електрофізика
Електричний транспорт
Безпека електрообладнання
Ювілеї

«ELECTRICAL ENGINEERING & ELECTROMECHANICS»

SCIENTIFIC & PRACTICAL JOURNAL
Journal was founded in 2002

ISSUE 5 / 2020
TABLE OF CONTENTS

E.I. Baida, B.V. Klymenko, M.G. Pantelyat, Yu.A. Yelanskyi, D. Trichet, G. Wasselynck

CHALLENGES OF DYNAMIC SIMULATION OF HIGH-SPEED ELECTROMAGNETIC VALVES OF GAS DISTRIBUTION DEVICES

High-speed electromagnetic valves of gas distribution devices are used in modern missile and space technology as jet micro-motors of the executive elements of missile stabilization systems, as well as to control the movement of spacecrafts in space. The problem of creating such valves which are simple and reliable in the operation is relevant. In this work, it is proposed at the development and design stage to perform computer modelling of mutually coupled electromechanical processes, such as: distribution of transient electromagnetic field, transients in an electric circuit, and movement of an electromagnet armature. Besides, the calculation of the force with which the compressed gas acts on the corresponding structural elements of the valve is proposed to be performed by solving the system of Navier-Stokes equations. All problems are solved by numerical methods in axisymmetrical formulation with the corresponding initial and boundary conditions. Improvement of the accuracy of electromagnetic calculations and taking into account the movement of the armature of an electromagnet in the process of multiphysics numerical simulation is achieved using so-called tunable elastic meshes. The paper presents a comparative analysis of the numerical results obtained for several designs of electromagnets. The features of the dynamics of high-speed electromagnets of gas distribution valves during on and off operations are analyzed, the corresponding dynamic characteristics calculated using the proposed technique are presented. References 17, table 1, figures 10.
Key words: **high-speed electromagnets, dynamics, Finite Element Method, multiphysics, elastic mesh.**

Быстродействующие электромагнитные клапаны газораспределительных устройств применяются в современной ракетно-космической технике в качестве реактивных микродвигателей исполнительных органов систем стабилизации ракет, а также для управления движением космическими летательными аппаратами в пространстве. Проблема создания простых в эксплуатации и надежных в работе указанных клапанов является актуальной. В настоящей работе предлагается на стадии разработки и проектирования выполнять компьютерное моделирование взаимосвязанных электромеханических процессов, таких как: распределение нестационарного электромагнитного поля, переходные процессы в электрической цепи, движение якоря электромагнита. При этом расчет силы, с которой сжатый газ действует на соответствующие конструктивные элементы клапана, предлагается выполнять путем решения системы уравнений Навье-Стокса. Все задачи решаются численными методами в осесимметричной постановке с соответствующими начальными и граничными условиями. Повышение точности электромагнитных расчетов и учет движения якоря электромагнита в процессе мультифизического численного моделирования достигается благодаря использованию так называемых перестраиваемых упругих сеток. В работе приведен сравнительный анализ численных результатов, полученных для нескольких конструкций электромагнитов. Проанализированы особенности динамики быстродействующих электромагнитов газораспределительных клапанов при выполнении операций включения и отключения, приведены соответствующие динамические характеристики, рассчитанные по предложенной методике. Библ. 17, табл. 1, рис. 10.
Ключевые слова: **быстродействующие электромагниты, динамика, метод конечных элементов, мультифизика, упругая сетка.**

Introduction. The use of jet micro-motors as the executive elements of missile stabilization systems [1] imposes stringent requirements on their dynamic characteristics. The range of control forces of such motors is much smaller than the forces created by missile engines designed to bring the spacecraft to a given flight path. To ensure the operation of micro-motors, a special power system and automation units (valves, regulators, starting devices) are required. Micro-motors with a power system form an autonomous system to obtain a control force due to the reaction of gas outflow from the nozzles of the motors.

Among the main problems of improving the gas-jet executive elements described above, it is necessary to note the problem of creating easy-to-operate and reliable in operation high-speed electromagnetic valves of gas distribution devices. As mentioned above, such valves are used, in particular, in modern missile and space technology in the system of executive devices to control the movement of spacecrafts in space (orientation, stabilization, orbit correction, maneuver, etc.) [1, 2].

In the vast majority of DC electromagnets, including the electromagnets of the drive of high-speed gas distribution valves, shunt windings [3] are used, which are

connected in parallel to the control circuit power sources.

At the stage of development and design of objects with DC electromagnets, including those used in space and missile technology, it is necessary to carry out numerical solution of the multiphysics problem including computer simulation of the following coupled phenomena and processes: distribution of transient electromagnetic field, transient current changes in the winding, and the movement of the armature of an electromagnet. Here, numerical solution of the problem of calculation of the force with which compressed gas acts on the corresponding structural elements of the valve should be obtained by solving the system of Navier-Stokes equations for the valve model. Despite the large number of publications on the calculation of DC electromagnets, there are no publications on complex computer modelling of these interrelated multiphysical processes.

A feature of the dynamics of electromagnets used in micro-motors of control systems for orienting spacecrafts is a small (about 0.3 mm) change in the size of the working gap at the displacement of its movable system, high speed of the order of 10-15 ms and short travel time of the order of 1-1.5 ms. Therefore, improvement of the

accuracy of electromagnetic calculations and reducing the time required to perform calculations in the process of multiphysical modelling in such cases can be achieved by the use of so-called tunable elastic meshes. This should also be implemented when developing an algorithm for numerical solution of the problem.

The goal of the paper is to develop a mathematical model of coupled multiphysics processes in high-speed DC electromagnets, to construct a numerical algorithm for calculation of the dynamics of high-speed DC electromagnets based on the technique of tunable elastic meshes as well as to apply the developed mathematical model and algorithm for numerical analysis of the dynamics of high-speed electromagnets of gas distribution valves of micro-motors of missile and space technology.

Problem definition. This paper presents a technique and results of the calculation of the dynamics of a high-speed armored-type electromagnet used in missile and space technology, in particular, in micro-motors of control systems for the orientation of rockets [3, 4].

Figure 1 shows a sketch of one of the designs of an electromagnet gas distribution valve with a switching ball as a locking element. Compressed high-pressure gas (7.5 MPa), which enters the valve through the inlet orifice, tends to lift the ball and direct the gas flow into the Laval nozzle, which provides the creation of reactive force, but this is prevented by a compression spring located in the electromagnet. This spring, with one side resting on a fixed stop, with the other side acts on the armature and, through the rod, pressed into the armature, on the ball. The spring is designed so that the force of its initial compression surpasses the force with which the compressed gas acts on the ball, which is pressed against the locking saddle, as a result of which the gas does not enter the nozzle.
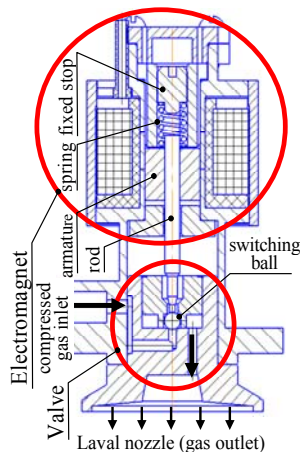
Fig. 1. Sketch of the electromagnetic valve

If a current is passed through the electromagnet winding, the armature is attracted to the stop, the rod moves together with the armature and stops exerting pressure on the ball, which, under the action of compressed gas, moves to the drainage (upper) saddle, releasing the locking (lower) saddle and the gas begins to flow into the Laval nozzle, creating the necessary reactive force.

One of the key parameters for electromagnetic valves is its switch-on speed. The operation time of these

valves, controlled by short-stroke high-speed electromagnets, is a few milliseconds. In the process of designing valves, it is necessary to calculate a variety of design options. For example, in the original version (Fig. 2,*a*) there is a zone of possible saturation of the magnetic core, so it is important to compare the results of the calculation of the dynamics in the original version and in the modified one (Fig. 2,*b*), where such a zone is absent. In the process of calculations, a different combination of materials (non-corrosive steel / «Armco» steel) is tested, as well as various conditions during the switch-on operation (cold winding / heated winding, maximum allowable voltage / minimum allowed voltage, etc.). For such calculations, it is necessary to use numerical methods for calculating dynamics that adequately reflect real processes in the electromagnet. The basis of such techniques is mathematical computer codes aimed at solving the problems of electromagnetic fields calculations.
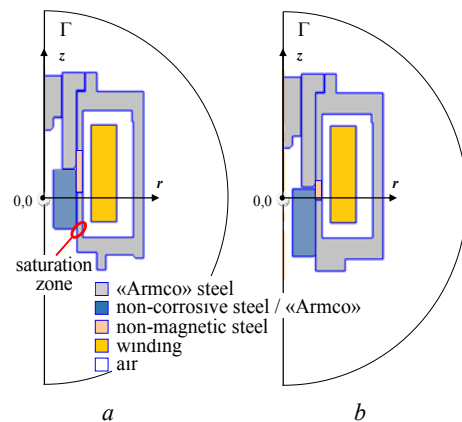
Fig. 2. Sketches of geometrical models of electromagnet for gas distribution valve: on the left (*a*) – the initial version, on the right (*b*) – the modified version

In gas distribution valves, armor electromagnets with penetrating armature are usually used, which with a high degree of adequacy can be considered as 2D axisymmetrical objects in a cylindrical coordinate system [5, 6], which greatly simplifies the technique and speeds up the calculation.

A technique proposed.

Geometry description (development of a geometric model). The use of computer codes in which the Finite Element Method is used requires careful preparatory work related to the description of the problem being solved, namely, the description of the geometry of the electromagnet on the *r-z* plane passing through the axis of its symmetry; a dividing of the cross-section of the electromagnet and the environment approximated to it (in the aggregate – the calculation domain) into subdomains that can be considered homogeneous in terms of physical properties; specifying the boundaries of these subdomains and differential equations describing the processes in these subdomains; as well as specifying the initial and boundary conditions.

The geometry description (development of a geometric model) of an electromagnet, taking into account the axisymmetrical nature of the calculation problem, is carried out on a plane passing through its axis of symmetry. This axis is located vertically, forming the *z*

axis in a cylindrical coordinate system, and its positive direction must coincide with the direction of movement of the armature of the electromagnet. One of the points on the z axis should be designated as the origin of the calculation domain, then the straight line passing through the point (0, 0) perpendicular to the z axis is the r axis in this coordinate system.

On a specified plane in the preprocessor environment of the corresponding code (FEMM or another code that uses the Finite Element Method), it is necessary to specify the coordinates of the nodal points of the «imprint» of a half axial section of the electromagnet and connect them with straight lines or arcs. The result should be a combination of closed figures that correspond to different parts of the electromagnet. For each of these closed figures, it is necessary to designate the material of which the corresponding part of the electromagnet is made, and in the material library of the corresponding computer code to prescribe the physical properties of this material to be used in the calculations.

The process of preparing a geometric model of an electromagnet described above is quite labor-intensive, however, it can be significantly accelerated if using one CAD software (AutoCAD, SolidWorks, etc.) to draw the mentioned «imprint» without dimensioning, shading, pouring, etc. In this case, this drawing must be placed on a computer «board» so that the origin of coordinates on the drawing and on the computer «board» coincide. If such a fragment of the drawing is saved in the .dxf format, then the resulting file can be imported into the appropriate mathematical computer code, which uses the Finite Element Method. One use this technique of preparing geometric models.

A mathematical model and problem solution.

The defined task is solved as a multiphysics problem involving computer simulation of the following coupled phenomena: transient electromagnetic field distribution in axisymmetrical formulation, transients of current change in the winding, and the movement of the armature of the electromagnet. Attempts of generalization and techniques of various multiphysics problems numerical solution are presented in [7-13].

Electromagnetic calculation is carried out by numerical solution of a system of partial differential equations describing transient magnetic field within the computational domain. The number of equations in the system is equal to the number of subdomains (including the outer space). One of these subdomains, namely the subdomain that corresponds to the cross-section of the winding, differs from the others in that it is influenced by external electric field. All subdomains filled with non-ferromagnetic and non-conductive materials have almost the same electric and magnetic characteristics as air or vacuum. If such subdomains are located nearby, they can be combined into one subdomain. In subdomains filled with non-ferromagnetic, but conductive materials, eddy currents arise, which ones depend on the specific resistance of the material of which the corresponding part is made. Therefore, each of these subdomains must be described separately.

When calculating transient magnetic field, the system of partial differential equations in terms of the magnetic vector potential A is solved, which, provided that all subregions in the calculation region remain fixed, has the following form [14]:

$$\sigma_k \cdot \frac{\partial \boldsymbol{A}}{\partial t} + \mathrm{curl}((\mu_0 \cdot \mu_{\mathrm{r}k})^{-1} \cdot \mathrm{curl}\,\boldsymbol{A}) = \sigma_k \cdot \boldsymbol{E}_k, \\ k = 1, 2, ..., n, \tag{1}$$

where k is the number of the subdomain; σ_k is the electrical conductivity of the material of the k-th subdomain; n is the total number of subdomains, including the outer space; μ_0 is the magnetic constant; $\mu_{\mathrm{r}k}(H)$ is the relative magnetic permeability of the material of the k-th subdomain depending on the magnetic field strength H; $\boldsymbol{E}_k$ is the vector of the external electric field strength created by an external field source in the k-th subdomain; $\boldsymbol{J}_k$ is the current density vector in the k-th subdomain; t is time.

In electromagnets, external sources act only on the winding, in which the vectors of the external electric field strength and current density have only azimuthal components, therefore the right-hand side of (1) for the subdomain of the winding does not depend on the electrical conductance of its conductive part

$$\sigma_k \cdot \boldsymbol{E}_k = \boldsymbol{J}_k = (i \cdot N / S) \cdot \mathbf{1}_\theta, \tag{2}$$

where i is the current in the winding; N is the number of turns of the winding; S is the area of the winding window indicated in the initial data: the winding's filling rate (the ratio of the cross-sectional area of copper conductors and the total cross-sectional area of the winding, i.e. the total cross-sectional area of the conductors and insulation) of the winding under consideration is 0.65; $\mathbf{1}_\theta$ is the azimuthal ort – a unit vector directed perpendicular to the plane of the calculation domain.

Since the winding consists of many insulated coils and its electrical conductance in the directions r and z is equal to zero, the equivalent electrical conductance of the winding is usually assigned a zero value and equation (1) for the subdomain of the winding acquires the following form:

$$\mathrm{curl}\,(\mathrm{curl}\,\boldsymbol{A}) = \mu_0 \cdot (i \cdot N / S) \cdot \mathbf{1}_\theta. \tag{3}$$

In other subdomains, external sources of electric field strength are absent, and in them $\boldsymbol{E}_k = 0$, and in subdomains occupied by air, also $\sigma_k = 0$, so the equations for sections of the magnetic core are the following:

$$\sigma_k \cdot \frac{\partial \boldsymbol{A}}{\partial t} + \mathrm{curl}\,((\mu_0 \cdot \mu_{\mathrm{r}k})^{-1} \cdot \mathrm{curl}\,\boldsymbol{A}) = 0; \\ k = 1, 2, ..., n_{\mathrm{m}} \tag{4}$$

and in the subdomains occupied by air or insulation:

$$\mathrm{curl}\,(\mathrm{curl}\,\boldsymbol{A}) = 0, \quad k = 1, 2, ..., n_{\mathrm{a}}, \tag{5}$$

where n_{m} and n_{a} are the numbers of subdomains of the magnetic core and air, respectively.

Since vector $\boldsymbol{A}$ has only an azimuthal component $\boldsymbol{A} = A_\theta = A$, equations (3)-(5) can be represented in scalar form, but the corresponding mathematical expressions are very cumbersome and are not given here.

One assume that by the time of the beginning of the transient ($t = 0$ s) the electromagnet is at rest. This means that there is some initial air gap δ_0 between the armature and the stop, the winding is not powered and there is no

magnetic field at all points of the computational domain, which corresponds to the zero initial condition for the magnetic vector potential:

$$A(r,z)|_{t=0} = A(r,z,0) = 0. \qquad (6)$$

To obtain a solution to the system of equations (3)-(5), it is also necessary to formulate conditions at the boundaries of the calculation domain. A natural geometric boundary is the axis of symmetry, at which the magnetic vector potential is zero. Considering the electromagnet as an object located in infinite space, then in solving such problems, one can use the Kelvin transform [15]. At the same time, experience shows that as the distance from the electromagnet moves away, the field attenuates very quickly, so with minor error this problem can be considered with a closed external area, limited in the *r-z* plane in a semicircle centered at the origin of coordinates. The radius of the semicircle should be 1.5-2 times the distance from the origin of coordinates to the farthest point of the «imprint» of the cross-section of the electromagnet. Thus, the calculation domain is a closed area, divided into *n* closed subdomains corresponding to individual parts of the electromagnet and the surrounding space within the calculation domain. Due to the fact that the magnetic field is very rapidly weakened, approaching zero with distance from the electromagnet with a practically closed magnetic core, the nature of the boundary conditions practically does not affect the calculation results, therefore zero conditions can be set at all points of the boundary Γ (see Fig. 2) of the calculation domain for the azimuthal component of the magnetic vector potential *A* (Dirichlet zero conditions) [14]:

$$A|_{\Gamma} = 0. \qquad (7)$$

Provided that all parts of the electromagnet remain fixed, for some given law of current *i* variation in time, using well-known numerical methods, it is possible to obtain a solution of the system of equations (2)-(4) taking into account the initial condition (5) and the boundary condition (6). In this work, the problem is solved by the Finite Element Method, and for discretization in time domain the implicit multistep Adams-Moulton method of the 4th order with adaptive selection of time step values is used. On each time step the system of equations (2)-(4) and the problem of dynamics of motion descrbed below are solved sequentially with the same numerical value of the time step for both indicated problems. The numerical solution is obtained in the form of a table of values of the magnetic vector potential at different points in time at the nodal points of the mesh, covering the of calculation domain, however, using various methods of interpolation, numerical differentiation and integration, it is possible to build a graphical picture of the force lines at different temporal points, as well as to calculate the values of a number of physical quantities, in particular, the values of magnetic flux density, magnetic flux, the force acting on individual subdomains, etc. at these times.

The solution of the system of equations (3)-(5) for a given law of current variation in the winding corresponds to the problem of calculation of the electromagnets with serial windings, which are used, for example, in current relays. In the absolute majority of electromagnets, including in the driving electromagnets of gas distribution valves, shunt windings are used, which are connected in parallel to the power sources of control circuits. When solving the problem of calculating the transient magnetic field of such electromagnets, provided that all its parts remain fixed, the system of equations (2)-(4) should be supplemented with a non-linear differential equation describing the transient of current change in the winding:

$$U + e = R \cdot i + L \cdot \frac{di}{dt}, \qquad (8)$$

where *U* is the winding power source voltage; *R* is the resistance of the winding circuit; *L* is the inductance of the external circuit; *e* is the back EMF arising in the winding:

$$e = -2 \cdot \pi \cdot \frac{N}{S} \cdot \int_S \frac{dA}{dt} \cdot r \cdot dr \cdot dz, \qquad (9)$$

When solving the system of equations (2)-(4), (7), taking into account dependence (8), zero boundary conditions (initial conditions (5) and conditions (6) on the boundary of the calculation domain) are used for the azimuthal component of the magnetic vector potential, and for the current *i* in the winding zero initial condition should be set:

$$i|_{t=0} = i(0) = 0. \qquad (10)$$

If the power source of the shunt winding is a capacitor with a capacitance *C*, pre-charged to the voltage U_{C0}, then in equation (7) the value *U* must be replaced by the current value of the voltage u_C on the capacitor:

$$u_C + e = R \cdot i + L \cdot \frac{di}{dt}, \qquad (11)$$

and the system (2)-(4), (10) with regard to (8) must be supplemented by additional differential equation:

$$C \cdot \frac{du_C}{dt} = -i. \qquad (12)$$

In the process of solving the system (3)-(5), (8) taking into account dependence (9) or system (3)-(5), (11), (12) taking into account (9), it is necessary to control the value of the traction force *F*, acting on the fixed armature of the electromagnet, and compare it with the initial value of the opposing force F_{r0}. Until the force *F* is less than the opposing force F_{r0}, the electromagnet is at rest and the armature is remain fixed.

The gas distribution valve is a precision device – the full stroke of its armature is 0.26 mm, and the stroke of the switching ball, from the stop saddle to the drainage one, is 0.19 mm. The characteristic of opposing forces acting on the electromagnet armature is shown in Fig. 3. The initial force of compression of the spring is equal to $F_{s0} = 40$ N, and the initial opposing force is only $F_{r0} = 21$ N, since the force created by the compressed gas and acting on the ball «pushes» it upwards and reduces the force opposing the movement of the armature. Thus, the valve will not operate if the electromagnetic force is less than 21 N in the presence of compressed gas at the valve inlet or when the force is less than 40 N without gas.

The numerical solution of the problem of calculating the force with which the compressed gas acts on the ball at its different positions is obtained by the Finite Element Method based on solving the Navier-Stokes system of equations for the valve model (see below). Compressed air heated to temperature of 1200 °C is considered as a moving

medium. The boundary conditions are the zero speed on the surface of the ball, the rod and on the inner walls of the valve, as well as the value of air pressure at the valve inlet (7.5 MPa) and exit to the atmosphere (0.1 MPa).
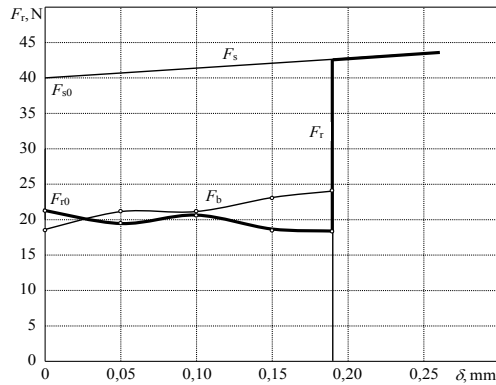

Fig. 3. Characteristics of the opposing forces acting on the electromagnet armature: F_s is the opposing force of the spring; F_b is the force with which the compressed gas acts on the switching ball; F_r is the total opposing force that occurs when gas is supplied to the valve inlet (in the absence of gas at the valve inlet, only the spring with the initial force F_{s0} opposes the movement of the armature)

The system of Navier–Stokes equations in the absence of volumetric forces has the following form in the matrix representation:

$$\rho \cdot (\boldsymbol{u} \cdot \nabla) \cdot \boldsymbol{u} = \nabla \cdot [-p \cdot \mathrm{I} + \eta \cdot (\nabla \cdot \boldsymbol{u} + (\nabla \cdot \boldsymbol{u})^{\mathrm{T}}) - \left(\frac{2}{3} \cdot \eta\right) \cdot (\nabla \cdot \boldsymbol{u}) \cdot \mathrm{I}]; \tag{13}$$

$$\nabla(\rho \boldsymbol{u}) = 0; \quad \rho = \rho(p, \vartheta); \quad \eta = \eta(\vartheta), \tag{14}$$

where ρ is the gas density; $\boldsymbol{u}$ is the gas speed vector matrix; p is the pressure; I is the unit matrix; η is the gas viscosity; ϑ is the temperature (here and above units of all quantities are used in the SI system).

Equation (13) is the equation for the steady flow of a gas stream, and expressions (14) are conditions for continuity of flow.

The boundary conditions for equations (13), (14) are: zero speed values on the walls of the elements, the condition of axial symmetry is that the normal speed component is zero, and the pressure values on inlet (7.5 MPa – compressed gas pressure) and outlet (0.1 MPa – atmospheric pressure).

The thermophysical characteristics of a gas (density and viscosity) substantially depend on temperature, therefore the system of equations (13), (14) must be supplemented with the equation of heat conduction for a gas in a stationary mode. Since gas is a compressible medium, it is necessary to take into account pressure work in the heat conduction equation – the ability of a gas to produce work by pressure, which significantly affects the temperature of the medium. The corresponding heat conduction equation in this case has the following form:

$$\nabla \cdot (\lambda \cdot \nabla \cdot \vartheta) = \rho \cdot C_p \cdot \boldsymbol{u} \cdot \nabla \cdot \vartheta + \left(\frac{\vartheta}{\rho}\right) \cdot \left(\frac{\partial p}{\partial \vartheta}\right)_p \cdot (\boldsymbol{u} \cdot \nabla \cdot p), \tag{15}$$

where λ is the thermal conductivity of gas; C_p is the heat capacity at constant pressure.

The boundary conditions for equation (15) are: the absence of heat transfer along the boundaries of the gas flow channel, the axial symmetry conditions, the inlet temperature which is assumed to be 1200 °C, and the open boundary condition at the outlet:

$$k \cdot \nabla \cdot \vartheta = \rho \cdot C_p \cdot \boldsymbol{u} \cdot \vartheta. \tag{16}$$

The force acting on the switching ball is defined as the surface integral of the forces caused by pressure, viscosity and speed pressure:

$$F_z = \int_S \begin{pmatrix} -\boldsymbol{n}_z p + \boldsymbol{n}_r \eta \left(\dfrac{\partial u_z}{\partial r} + \dfrac{\partial u_r}{\partial z} \right) + \\ + 2\boldsymbol{n}_z \eta \dfrac{\partial u_z}{\partial z} \end{pmatrix} \cdot dS, \tag{17}$$

where $\boldsymbol{n}$ is the ort of appropriate direction.

A sketch of the valve system and its geometric model are shown in Fig. 4. The outlet in the valve has the shape of a cylinder, and in the model it has the shape of a disk with the same cross-sectional area in the direction of movement of the compressed gas (in the model – in the radial direction).

A specific feature of this problem solution is that the sought quantities (the temperature ϑ, the speed $\boldsymbol{u}$ and pressure p at all nodes of the mesh covering the calculation domain) are complex interdependent functions, and the compressed gas characteristics (the specific heat conductivity λ, the density ρ, the viscosity η, and the specific heat C_p) in individual nodes of the mesh can differ from each other by several orders of magnitude. The use of simple iterative procedures for solution of problems in which the convergence of the iterative process strongly depends on the initial values of the sought quantities, as a rule, does not lead to success. Our problem belongs to the category of exactly such ones: at unsuccessfully selected initial values of the sought values, the iterations do not converge, and at successfully selected ones they converge. Therefore, in the calculations we applied more complex iterative procedures, which, finally, led to the convergence of iterations. The essence of these procedures is that the solution to the problem is divided into two stages: 1) preliminary calculations to determine the initial values of the sought quantities in the iterative process of joint solution of equations (13)-(15), and 2) the iterative process of joint solution of equations (13)-(15) with initial the values of the sought quantities found in step 1). In turn, stage 1) is divided into two sub-stages: 1a) solving the problem of calculating the distribution of the speed and pressure in the calculation domain at a given initial temperature distribution, and 1b) solving the problem of calculating the temperature distribution in the calculation domain at the found distribution of the speed and pressure. With this approach to solving this problem, the calculation algorithm looks like this:

1. We set a fixed temperature distribution (for example, the temperature at all mesh nodes in the computational domain is taken equal to the ambient temperature) and solve equations (13), (14), as a result of which values of the temperature and speed are obtained at all mesh nodes which are considered as new initial values for the next iteration, etc. Here, the results at the previous and subsequent iterations are compared and the calculations continue until the changes in the pressure and speed in the module in all the calculation nodes become smaller than some small positive predefined values.

2. Having fixed the obtained values of the pressure and speed, the heat equation (15) is solved using the iteration method, where at each iteration at each node the compressed gas characteristics are determined (the specific thermal conductivity λ, the density ρ, and specific heat C_p) as a function of temperature values, found in the previous iteration. The results of calculating the temperature at all nodes of the mesh are considered as the initial values for the next iteration and the calculation is repeated until the temperature changes in the module in all the calculation nodes become less than some small positive values given in advance.

3. Having accepted the obtained values of the pressure, speed and temperature at all nodes of the mesh as the initial ones, we solve the equations of gas flow motion and thermal conductivity (13)-(15) jointly using the iteration method, where at each iteration in each node values of compressed gas characteristics (the thermal conductivity λ, the density ρ, the viscosity η, and the specific heat C_p) are determined as a function of pressure, speed and temperature values found at the previous iteration, until the changes in the pressure, speed, and temperature in the module in all calculation nodes become smaller than some small positive values preset in advance.
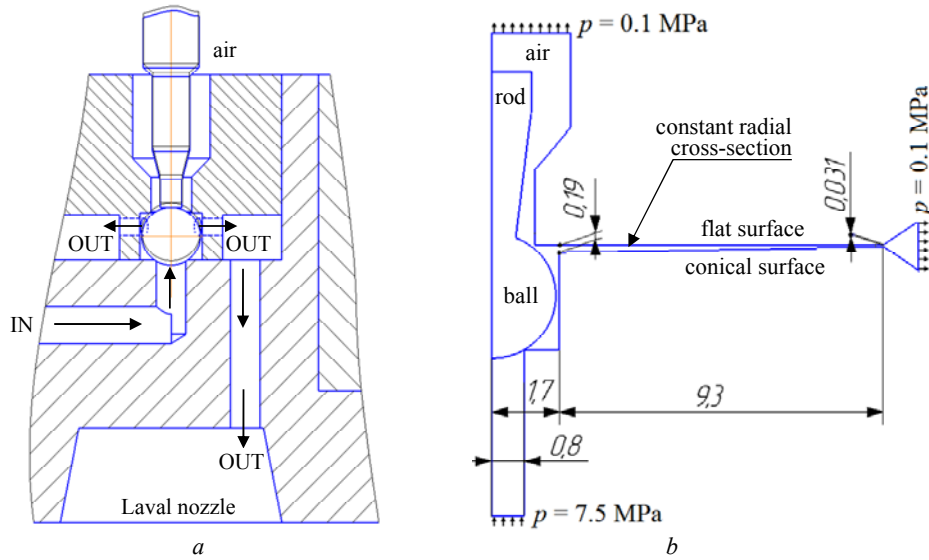
Fig. 4. Sketch of the valve system (a) and its geometric model (b)

The results of the calculation of the forces acting on the ball in its various positions are shown in Table 1.

Table 1
The results of the calculation of the forces acting on the ball

s, mm	0.00	0.05	0.10	0.15	0.19
F, N	18.25	21.46	21.13	23.39	23.45

Notes:
1. The path s is measured from the initial position of the ball.
2. The force F has only the axial component.

Figures 5, 6 illustrate some intermediate results of the calculations: a picture of the pressure field of the compressed gas on the ball and a picture of the speed field of the compressed gas in the nozzle at the outlet of the valve.

When performing calculations of the dynamics with a moving armature for the subdomain corresponding to the armature, equation (4) and expression (9) should be replaced by expressions that take into account the movement of the armature:

$$\sigma_{ar} \cdot \left(\frac{\partial \mathbf{A}}{\partial t} - \mathbf{v}_{arz} \times \mathrm{curl}\mathbf{A} \right) + \tag{18}$$

$$\mathrm{curl}((\mu_0 \cdot \mu_{rar})^{-1} \cdot \mathrm{curl}\mathbf{A}) = 0,$$

$$e = -2 \cdot \pi \cdot \frac{N}{S} \cdot \int\limits_{S} \left(\frac{\partial A}{\partial t} + v_{arz} \cdot \frac{\partial A}{\partial z_a} \right) \cdot r \cdot \mathrm{d}r \cdot \mathrm{d}z, \tag{19}$$

where σ_{ar}, μ_{rar} are the electrical conductance and relative magnetic permeability of the material (steel) of which the armature is made; $\mathbf{v}_{arz}$ is the speed vector of the armature in the direction of z coordinate.
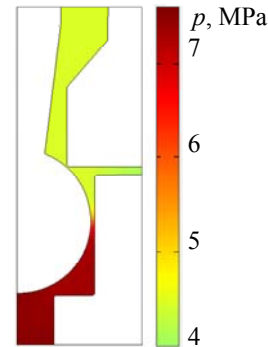
Fig. 5. Picture of pressure field of the compressed gas on the ball at $s = 0.19$ mm (final ball position)
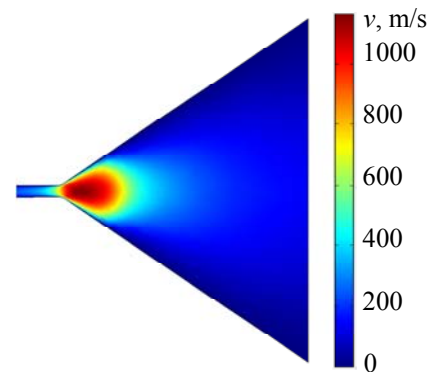
Fig. 6. Picture of the speed field of the compressed gas in the nozzle at the valve outlet at $s = 0.10$ mm (close to the average position of the ball)

When calculating the dynamics in the process of motion, the system of equations describing the magnetic field and current in the winding is supplemented by the equations of motion, which, with a constant moving mass m, has the form:

$$m \cdot \frac{dv_{arz}}{dt} = F - F_r; \qquad (20)$$

$$\frac{ds}{dt} = v_{arz} \qquad (21)$$

with zero initial conditions:

$$v_{arz}(t_0) = 0; \ s(t_0) = 0. \qquad (22)$$

Here, the following notation is used: F is the electromagnetic force that ensures the movement of the armature; F_r is the force opposing the movement of the armature; v_{arz} is the module of the vector $\boldsymbol{v}_{arz}$; s is the path traversed by the armature after the start of the movement; t_0 is the point in time corresponding to the beginning of the movement.

The fixed and moving subdomains appear to be located in a certain elastic space covered with a mesh.

When the position of the moving subdomain changes, the meshes belonging to the fixed and moving parts remain unchanged.

Similar algorithms based on the use of deformed elastic finite element meshes are used in the numerical solution of hydrodynamic problems [16, 17]. The mesh belonging to the elastic subdomain is deformed in accordance with the law of motion of the armature, which is defined by equations (20), (21). With a significant change in the gap, the angles opposite the bases of some mesh cells become close to 180°, which reduces the accuracy of the calculations.

In this work, an algorithm is used that involves monitoring of the angles of the deformable mesh cells and stopping the computation when one of the angles becomes greater than a certain predetermined value (in our case, 170 °C). After stopping, the code rearranges the mesh and continues the calculation.

Figure 7, as an example, shows a fragment of computational subdomains covered with a triangular mesh. As can be seen, the meshes on moving and fixed subdomains, corresponding to different parts of the electromagnet magnetic core, are not deformed during movement of the armature due to the invariance of the shape of these subdomains, and the mesh covering the subdomain surrounding the armature is elastic and significantly deformed.

Fig. 7. A fragment of the calculation domain covered with a triangular mesh:
a – armature in the initial position; b – armature in the end position

Numerical results and their analysis.

Figure 8 shows the results of the calculation of a modified version of an electromagnet corresponding to the geometric model shown in Fig. 2,b. In Fig. 8,a, in addition to the picture of the field distribution, the main dimensions of the electromagnet are shown: the gap δ varies from 0.3 mm in the initial position to 0.04 mm in the final position, thus the armature stroke is 0.26 mm. In Fig. 8,b, in addition to the field distributions, the main subdomains are indicated: 1 – electrical steel, 2 – winding, 3 – insulation («air»), 4 – non-magnetic steel, as well as a scale of values of magnetic flux density B is shown.

Magnetic field distributions presented in Fig. 8, show the process of penetration of the magnetic field into the magnetic core along the entire perimeter, and the magnetic flux density in the area of the working gap reaches large values (1.8 T) within 5 ms after the start of the process.

Figures 9,a,b show the results of the calculation of the basic dynamic characteristics of this electromagnet under the following operating conditions: the armature is made of electrical steel, the number of windings is 1155, the winding is heated to 112 °C, the resistance of the heated winding is 55 Ω, the supply voltage is minimal allowable: 24 V. Figure 9,a shows the calculation results for the case when gas is supplied to the valve inlet, and Fig. 9,b – when the gas is not supplied. In the first case, the operating time is 9 ms, and in the second case 13.5 ms. It can be seen that the modified electromagnet operates in both cases. In the original version of the electromagnet with a saturation zone corresponding to the geometric model shown in Fig. 2,a, the operating time when there is a supply of compressed gas to the valve inlet is 9.5 ms, and without gas supply the electromagnet does not operate.

The requirements for the speed of gas distributors are put forward not only when the winding is switched on, but also when it is switched off. Switching off the winding with the help of contact switching elements is accompanied by their sparking, which can cause radio interference and a negative effect on the electronic

devices of the control object. Switching off the winding using semiconductor switching elements requires overvoltage protection. Typically, such protection is implemented by shunting the winding with an «opposite» diode that does not conduct current when the winding is energized, and automatically opens when the switching element stops energizing the winding. After this moment, the current in the winding, and, consequently, the force of attraction of the armature to the stop, begin to decrease,

but for some time the armature remains in the attracted state until the force of attraction exceeds the opposing force. At the moment when the force of attraction is compared with the opposing force, the movement of the armature begins in the opposite direction. This movement continues until the armature returns to its original position. The time interval from the moment when the winding supply ceases to the moment when the armature movement ends is called the release time.

Fig. 8. Distribution of the magnetic flux density module in 1 ms after the beginning of the transient process (*a*); the same in 5 ms (*b*)

Fig. 9. Basic dynamic characteristics of a modified version of an electromagnet when performing the switching on operation: *a* – when supplying compressed gas to the valve inlet; *b* – the same without gas supply

Calculations of dynamic processes during the operation of switching off the winding, shunted by an «opposite» diode, are performed for the case when the

operation of switching off occurs when there is a supply of compressed gas to the valve inlet. In this case, the release time is 16 ms (Fig. 10,*a*).

Fig. 10. Dynamic characteristics of a modified version of an electromagnet when performing the switching off operation of the winding, shunted by the «opposite» diode: *a* – without additional resistor; *b* – with a resistor with resistance of 56 Ω

It is possible to reduce the release time connecting an additional resistor in series with the diode. This reduces the time constant of the winding circuit, and accelerates the process of reducing current, magnetic flux and force. This is confirmed by the results of the calculations presented on Fig. 10,*b*: in the presence of an additional resistor with resistance of 56 Ω, the release time is reduced from 16 ms to 9.5 ms which corresponds to experimental results.

Conclusions.

A numerical technique and results of the calculation of the dynamics of a high-speed armored-type electromagnet used in micro-motors of control systems for the orientation of rockets are presented. The multiphysics computer simulation involves numerical analysis of the following coupled phenomena: transient electromagnetic field distribution in axisymmetrical formulation, transients of current change in the winding, and the movement of the

armature of the electromagnet. All corresponding differential equations are solved with regard to appropriate initial and boundary conditions as well as taking into account nonlinear material properties for all structural parts of electromagnets. Electromagnetic field calculations are carried out by the Finite Element Method involving the use of so-called tunable elastic meshes. Peculiarities of the numerical algorithms used are described in detail. Comparative analysis of numerical results obtained for a few electromagnet designs is presented.

REFERENCES

1. Olejnik V.P., Yelanskyi Yu.A., Kaluger L.G. Mathematical modelling of a gas distributor of the carrier rocket gas-jet control system. *Space Technology. Missile Weapons*, 2017, iss. 1 (113), pp. 59-66. (Rus).
2. Beliaev N.M., Belik N.P., Uvarov E.I. *Jet Control Systems for Spacecrafts*. Moscow, Mechanical Engineering Publ., 1979. 232 p. (Rus).
3. Bajda Ye.I., Klymenko B.V., Pantelyat M.G., Korol O.G., Yelanskyi Yu.A. Peculiarities of calculating forced electromagnets shunt windings heating in transient modes. *Proceedings of the 18th International IGTE Symposium on Numerical Field Calculation in Electrical Engineering*. Graz, Austria, September 2018, p. 31-36.
4. Bajda Ye.I., Klymenko B.V., Pantelyat M.G., Yelanskyi Yu.A., Trichet D., Wasselynck G. Peculiarities of calculating the dynamics of high-speed electromagnets using tunable elastic meshes. *Proceedings of the 18th International Symposium on Electromagnetic Fields in Mechatronics, Electrical and Electronic Engineering (ISEF'2019)*. Nancy, France, August 2019. 6 p.
5. Zhang J.Z., Cai C.H., Wu C.G. Design and analysis of a new permanent magnet actuator for medium voltage vacuum circuit breakers. *Applied Mechanics and Materials*, 2013, vol. 313-314, pp. 20-26. **doi: 10.4028/www.scientific.net/amm.313-314.20**.
6. Bissal A., Magnusson J., Salinas E., Engdahl G. Multiphysics modeling and experimental verification of ultra-fast electro-mechanical actuators. *International Journal of Applied Electromagnetics and Mechanics*, 2015, vol. 49, no. 1, pp. 51-59. **doi: 10.3233/jae-140176**.
7. Bajda Ye.I., Klymenko B.V., Pantelyat M.G., Trichet D. Wasselynck G. Electromagnetic and thermal transients during induction heating of cylindrical workpieces. *Acta Technica*, 2018, vol. 63, no. 5, pp. 657-682.
8. Pantelyat M.G. Multiphysical numerical analysis of electromagnetic devices: state-of-the-art and generalization. *Electrical Engineering & Electromechanics*, 2013, no. 3, pp. 29-35.
9. Pantelyat M.G. Multiphysics in electromagnetic devices simulation and design: an attempt of generalization. *Acta Technica*, 2012, vol. 57, no. 2, pp. 127-142.
10. Pantelyat M.G., Shulzhenko N.G., Matyukhin Yu.I., Gontarowsky P.P., Doležel I., Ulrych B. Numerical simulation of electrical engineering devices: magneto-thermo-mechanical coupling. *COMPEL: The International Journal for Computation and Mathematics in Electrical and Electronic Engineering*, 2011, vol. 30, no. 4, pp. 1189-1204. **doi: 10.1108/03321641111133127.**
11. Pantelyat M.G., Féliachi M. Magneto-thermo-elastic-plastic simulation of inductive heating of metals. *The European Physical Journal Applied Physics*, 2002, vol. 17, no. 1, pp. 29-33. **doi: 10.1051/epjap:2001001**.
12. Podoltsev O.D., Kucheriava I.M. Multiphysics modeling of electrotechnical devices. *Technical Electrodynamics*, 2015, no. 2, pp. 3-15 (Rus).
13. Podoltsev O.D., Kucheriava I.M. *Multiphysics modeling in electrical engineering*. Kyiv, The Institute of Electrodynamics of the National Academy of Sciences of Ukraine Publ., 2015. 305 p. (Rus).
14. Stratton J.A. *Electromagnetic Theory*. NJ, Wiley, 2007. 640 p.
15. Meeker D. Improvised open boundary conditions for magnetic finite elements. *IEEE Transactions on Magnetics*, 2013, vol. 49, iss. 10, pp. 5243-5247. **doi: 10.1109/tmag.2013.2260348.**
16. Cizmas P.G.A., Gargoloff J.I. Mesh generation and deformation algorithm for aeroelasticity simulations. *Journal of Aircraft*, 2008, vol. 45, no. 3, pp. 1062-1066. **doi: 10.2514/1.30896.**
17. Dwight R.P. Robust mesh deformation using the linear elasticity equations. *Computational Fluid Dynamics*, 2006, pp. 401-406. **doi: 10.1007/978-3-540-92779-2_62.**

E.I. Baida[1], *Doctor of Technical Science, Associate Professor,*
B.V. Klymenko[1], *Doctor of Technical Science, Professor,*
M.G. Pantelyat[1], *Candidate of Physics and Mathematics, Associate Professor,*
Yu.A. Yelanskyi[2],
D. Trichet[3], *Professor,*
G. Wasselynck[3], *Assistant Professor,*
[1] National Technical University «Kharkiv Polytechnic Institute»,
2, Kyrpychova Str., Kharkiv, 61002, Ukraine,
e-mail: baida.kpi@gmail.com, m150462@yahoo.com
[2] Yuzhnoye State Design Office,
3, Krivorozhskaya Str., Dnipro, 49008, Ukraine,
e-mail: yuyelans@gmail.com
[3] IREENA, Polytech'Nantes, University of Nantes,
37 boulevard de l'université BP406,
44600 Saint-Nazaire, France,
e-mail: didier.trichet@univ-nantes.fr,
guillaume.wasselynck@univ-nantes.fr

V.I. Milykh, L.V. Shilkova

CONTROL CURRENT METHOD OF THE CONCENTRATION OF FERROMAGNETIC ELEMENTS IN THE WORKING CHAMBER OF THE TECHNOLOGICAL INDUCTOR OF MAGNETIC FIELD DURING ITS OPERATION

Introduction. A rotating magnetic field three-phase inductor designed for the technological processing of various substances is considered. The processing is carried out by ferromagnetic elements in the form of pieces of iron wire moving with a magnetic field. Problem. The control problem of the concentration of ferromagnetic elements in the working chamber of the inductor is solved. This is necessary in order to replenish the chamber in time with elements that wear out but without interrupting the processing. Methodology. The proposed control method consists in observing the current of the inductor stator winding, which is carried out during its operation and does not require intervention in the technological process of processing. Results. The theoretical substantiation of the method is given and a practical calculation evaluation of its adequacy is made on the example of a specific inductor. The theory and practice of the method are based on numerical calculations of the magnetic field, electromagnetic parameters and the angular characteristics of the inductor. Practical value. The practical use of the method is to automatically determine the time of reloading the chamber with ferromagnetic elements that are worn out during the inductor operation. This increases the performance of the inductor and eliminates its downtime. References 10, figures 8.
Key words: **magnetic field inductor, working chamber, concentration of ferromagnetic elements, current control, numerical field analysis, electromagnetic parameters, angular characteristics.**

Представлений метод визначення концентрації феромагнітних елементів в робочій камері індуктора обертового магнітного поля, призначеного для технологічної обробки різних речовин. Метод полягає в контролі струму обмотки статора індуктора і не вимагає втручання в технологічний процес обробки. Надано теоретичне обґрунтування методу і проведена практична розрахункова оцінка його адекватності на прикладі конкретного індуктора. Теорія і практика методу засновані на чисельних розрахунках магнітного поля, електромагнітних параметрів і кутових характеристик індуктора. Практичне використання методу полягає у визначенні часу додаткового завантаження камери феромагнітними елементами, які стираються в процесі роботи індуктора. Бібл. 10, рис. 8.
Ключові слова: **індуктор магнітного поля, робоча камера, концентрація феромагнітних елементів, контроль струму, чисельно-польовий аналіз, електромагнітні величини, кутові характеристики.**

Представлен метод определения концентрации ферромагнитных элементов в рабочей камере индуктора вращающегося магнитного поля, предназначенного для технологической обработки различных веществ. Метод заключается в контроле тока обмотки статора индуктора и не требует вмешательства в технологический процесс обработки. Дано теоретическое обоснование метода и проведена практическая расчетная оценка его адекватности на примере конкретного индуктора. Теория и практика метода основаны на численных расчетах магнитного поля, электромагнитных параметров и угловых характеристик индуктора. Практическое использование метода заключается в определении времени дозагрузки камеры ферромагнитными элементами, которые истираются в процессе работы индуктора. Библ. 10, рис. 8.
Ключевые слова: **индуктор магнитного поля, рабочая камера, концентрации ферромагнитных элементов, токовый контроль, численно-полевой анализ, электромагнитные величины, угловые характеристики.**

Introduction. In a number of industries, rotating magnetic field inductors (RMFIs) have become widespread for the processing of various substances. Such inductors are part of various mixers, grinders and separators [1-3].

The stator design of the RMFI is similar to the stator of a three-phase asynchronous motor. Inside it is a cylindrical working chamber through which the processed substance is passed in the axial direction. Ferromagnetic elements (FEs) in the form of pieces of iron wire are used for processing. They are ferromagnetic and move with a rotating field, creating a so-called «eddy layer» in the chamber [1, 3]. The chamber shell is made of non-magnetic steel and does not interact with the magnetic field.

The magnetic field in the chamber provides not only the movement of the FEs, but also keeps them on the active length of the inductor, which is approximately equal to the axial length of the stator ferromagnetic core.

For the operation of the inductor, a certain amount of FEs is poured into the working chamber, depending on the properties of the processed substance and the intensity of the processing mode. For various reasons, considered in [1], the filling of the chamber with elements decreases with time, and their periodic replenishment is required, which is done through a special pipe without switching off the inductor.

In this case, the inductor under consideration is intended for an apparatus with an «eddy layer» that treats waste water, as described in [1]. In this case, the wear of FEs is predetermined by the friction of their ends against the chamber shell, which even leads to the appearance of through annular grooves in the shell. There are other wear factors, but they are not significant by comparison. The abrasion of the FE ends in the fundamental work [1] was defined by the term «wear of length».

One of the problems of using the described apparatus is the task of when and in what quantity it is necessary to replenish the chamber with a new portion of the FEs.

A known solution is the installation of measuring coils on the bore of the stator core. An EMF is induced in

them by a rotating magnetic field, which should change with a decrease in the FE concentration and, therefore, a change in the magnetic properties of the medium in the chamber. Thanks to this, the operator or control system receives information that contributes to the solution of the specified task.

However, in practice the described method turns out to be insensitive. And it was not sufficiently substantiated by calculation tests, due to the serious assumptions of the method based on the theory of magnetic circuits used to calculate magnetic fields.

The situation changed with the development of a technique for calculating electromagnetic parameters and characteristics of RMFI based on numerical calculations of magnetic fields, which is presented in the authors' works [4, 5]. Due to this, it was revealed that it is possible to predict the change in the current of the stator winding of the inductor with a change in the concentration of the FEs in the working chamber. This was confirmed in [6] when studying a relatively small experimental model of the inductor.

The goal of this work is a theoretical substantiation and calculation confirmation of the adequacy of the method for predicting the current concentration of FEs in the working chamber of the RMFI based on monitoring the current of its stator winding. This is carried out on the basis of numerical calculations of the magnetic field and electromagnetic parameters of the inductor.

Object of study. The RMFI electromagnetic system is shown in Fig. 1 by its cross section. The rectangular (x, y) and polar (r, α) coordinate systems used are shown.
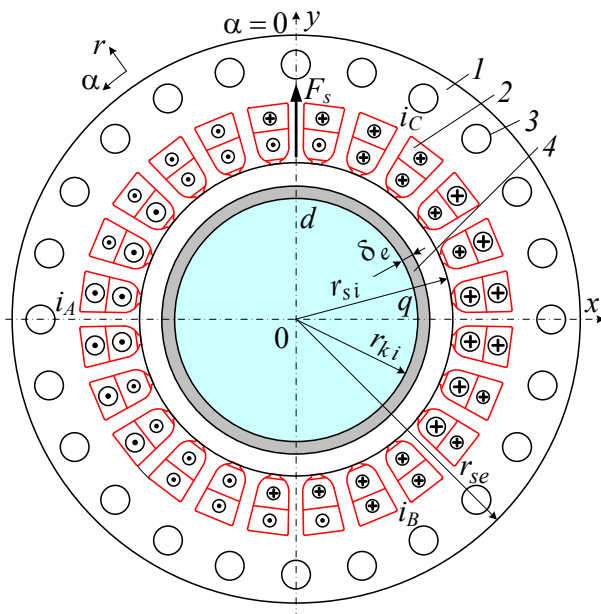

Fig. 1. Electromagnetic system of the RMFI:
1 – laminated stator core; *2* – three-phase winding; *3* – ventilation ducts; *4* – shell of the working chamber with thickness δ_e = 5 mm

The inductor is a three-phase two-pole. For technological reasons, the radius of the inner surface of the chamber r_{ki} = 0.047 m and the axial length of the stator core l_a = 0.25 m are given. The radii of the core bore r_{si} = 0.06 m and its outer surface r_{se} = 0.109 m are

calculated. The inductor winding is two-layer with a relative shortening of 10/12, the connection diagram is «star», there are 72 turns per phase. The core is made of electrical steel grade 2212, sheet thickness 0.5 mm, filling factor K_{Fe} = 0.95.

A fragment of an idealized structure with a uniform FE distribution in the working chamber is shown in Fig. 2. The real structure of the elements will be less strict [6], and idealization, as in [1, 4], is necessary for an accessible organization of calculations.
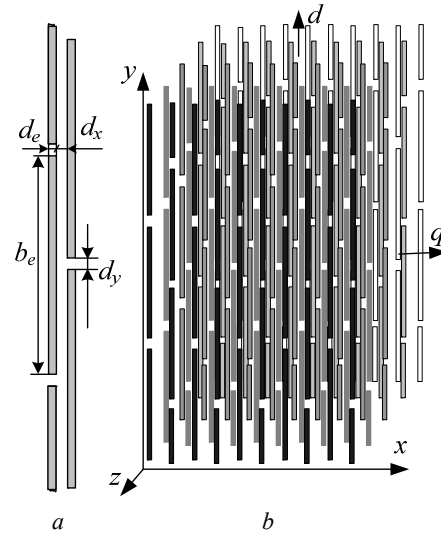

Fig. 2. Fragment of an idealized structure of ferromagnetic elements

FEs are made of steel grade St3. Their dimensions and clearances are taken according to Fig. 2,*a*: d_e = 1 mm; b_e = 20 mm; d_x = 1.5 mm; d_y = 1 mm. In this case, the filling factor of the chamber with them in the xy plane (Fig. 2,*b*) K_{Fes} = 0.322. In the yz plane, the same factor is adopted, and then the volumetric filling factor is 0.104.

In the cross section of the RMFI (see Fig. 1), the magnetic field is considered to be plane-parallel. Therefore, the round sections of the FEs are replaced by square ones with appropriate resizing, as described in [4].

The nominal phase voltage of the stator winding U_{sN} is 100 V at frequency of f_s = 50 Hz. In ideal idle mode, i.e. in the absence of ferromagnetic elements in the working chamber, the average value of the magnetic flux density B_{av} is set and is 0.12 T, which corresponds to practically used inductors.

Basics of numerical field calculations. The source of the rotating magnetic field in the inductor is a three-phase symmetric system of currents of phase stator windings (see Fig. 1):

$$i_A = I_m \cos(\omega_s t + \beta);$$
$$i_B = I_m \cos(\omega_s t - 2\pi/3 + \beta); \tag{1}$$
$$i_C = I_m \cos(\omega_s t + 2\pi/3 + \beta),$$

where t is time; $I_m = \sqrt{2}I_s$ is the amplitude of the phase currents; I_s is their effective value; $\omega_s = 2\pi f_s$ is the angular frequency; β is the initial phase of the currents, which sets the angular displacement of the direction of the MMF of the stator winding F_s from the y axis which is necessary for a particular calculation mode.

Figure 1 shows the directions of currents in the phase windings in the ideal idle mode, at which β = 0, and therefore the MMF vector F_s is directed along the *y*-axis.

The magnetic field of the inductor in its central cross section is described by the well-known 2D differential equation:

$$\text{rot}[\mu_a^{-1}\text{rot}(\vec{k}A_z)] = \vec{k}J_z , \qquad (2)$$

where $\vec{k}$ is the ort along the axial *z*-axis; A_z, J_z are the components of the magnetic vector potential (MVP) and current density; μ_a is the absolute magnetic permeability.

The propagation of the magnetic field is limited by the outer surface of the inductor core, where the Dirichlet boundary condition is set: $A_z = 0$.

The tool of the presented research is the numerical calculations of the magnetic field by the Finite Element Method using the FEMM code [7] with its control by the created Lua script, as in [8].

Moreover, in contrast to [4, 5], here the calculation of the field itself is carried out with direct account of a discrete medium with FEs in the working chamber, instead of replacing it with an equivalent continuous medium. This eliminates the assumptions and additional errors associated with such a replacement.

The assumption of the description of the magnetic field by equation (2) is justified by calculations in [9] and experimentally confirmed in [10], and in this inductor the ratio of the axial length and diameter of the core bore l_a/d_{si} is 2.3 and 3.2 times larger, respectively, which reduces possible calculation error.

When calculating the field, the magnetic permeability μ_a in the laminated steel core and in the FEs is taken into account by a well-known method, taking into account the magnetization curves of steels. The filling factors of the core K_{Fe} and the working chamber K_{Fes} along the *z* axis are set as initial parameters for the FEMM code, and are taken into account by its software.

The phase relations of the electromagnetic quantities of the inductor and the essence of the angle β are considered in detail in [4, 5]. It is shown that when the inductor is operating under load, the angle β is in the range of 0 – 90°, and at extreme values, the electromagnetic torque (EMT) is absent. This corresponds to the mode of the operating idle [5], which differs from the ideal idle by the presence of ferromagnetic elements in the chamber.

Figures 3, 4 show the results of calculating the magnetic field in the mode of operating idle and in the nominal load mode at the indicated values of the stator current I_s and angle *β*. In Fig. 5 the magnetic field in the working chamber is shown on an enlarged scale for the nominal load mode.

In fact, the EMT in the considered inductor is reactive, and its principle of operation corresponds to a synchronous reluctance motor, which is substantiated in [4, 5]. Therefore, in the working chamber, the longitudinal axis *d* is assigned in the direction of the FEs orientation, and the transverse axis *q* is perpendicular to it (see Fig. 1). In the steady-state operating mode, the axes rotate together with these elements and the field with a frequency n_s.
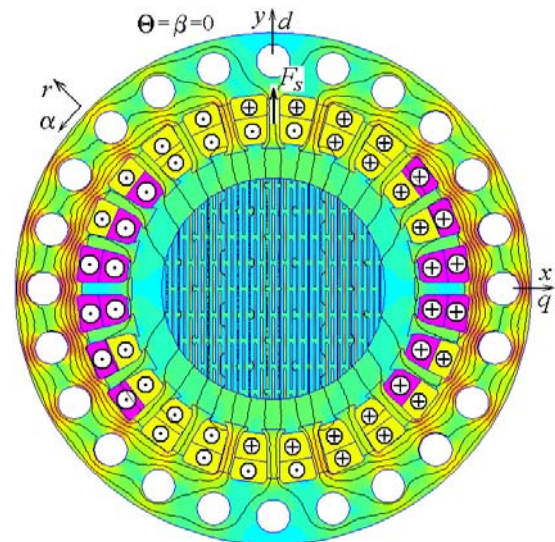
Fig. 3. Magnetic field in the inductor in the mode of the working idle at I_s=35 A and *β*=0
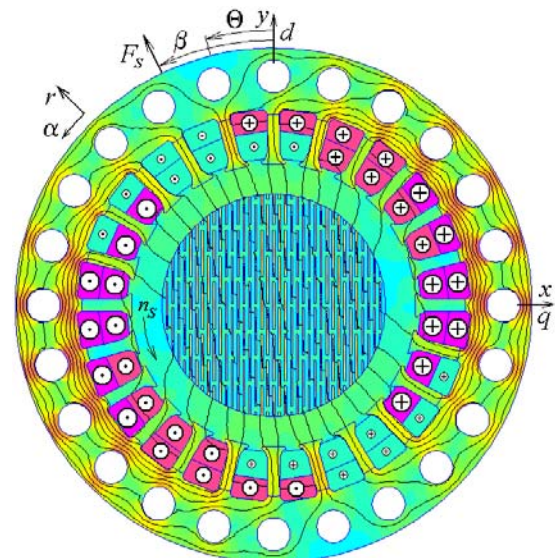
Fig. 4. Magnetic field in the inductor in the nominal load mode at I_s=36 A and β=26.7º

In Fig. 4, 5 the deviation of the field lines from the longitudinal axes of the Fes is shown. This is a condition for the occurrence of the EMT which acts on the entire mass of FEs and sets them in motion. The nature of this moment corresponds to Maxwell's theory of the magnetic tension tensor, which is explained in [5].
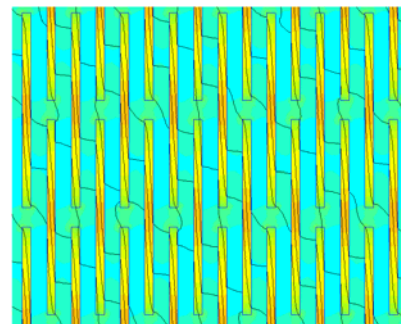
Fig. 5. Fragment of the picture of the magnetic field in the working chamber of the inductor at nominal load

Electromagnetic quantities in the RMFI are determined on the basis of the method described in [5], and for this work the following provisions are in demand from it.

According to the results of calculating the magnetic field using the FEMM code [7], the EMT is obtained through the Maxwell tensor of magnetic tension:

$$M_{em} = \frac{l_a}{\mu_0(r_{si} - r_{ki})} \int_{S_\delta} B_r B_\alpha r dS, \qquad (3)$$

where B_r and B_α are the radial and angular components of the magnetic flux density; S_δ is the cross-sectional area of the gap, limited by circles with radii r_{ki} and r_{si} on the sides of the chamber and stator; μ_0 is the magnetic constant.

According to the MVP distribution, the time function of the first harmonic of the magnetic flux linkage of the phase stator winding is formed:

$$\Psi_a = \Psi_m \cos(\omega_s t + \gamma_{\psi a}). \qquad (4)$$

In accordance with the law of electromagnetic induction, from (4) the EMF of this winding is obtained:

$$e_a = \omega \Psi_m \cos(\omega_s t + \gamma_{\psi a} - \pi/2), \qquad (5)$$

whence its effective value and initial phase:

$$E_a = \sqrt{2} \pi f_s \Psi_m; \quad \gamma_{Ea} = \gamma_{\psi a} - \pi/2. \qquad (6)$$

The balance of voltages in the phase stator winding is represented by the complex equation [4]:

$$\underline{U}_s = -\underline{E}_a + jX_v \underline{I}_s + (R_s + R_{mag})\underline{I}_s, \qquad (7)$$

where on the basis of (1) and (6) the complexes of its current $\underline{I}_s = I_s e^{j\beta}$ and EMF $\underline{E}_a = E_a e^{j\gamma_{Ea}}$ appear.

The formula (7) includes the active resistance R_s of the stator winding and the reactance of its frontal dissipation X_v, which are calculated as in induction motors: $R_s = 0.31$ Ω and $X_v = 0.39$ Ω. The active resistance R_{mag} reflects the power of the magnetic losses and is determined during the iterative calculation of the magnetic field.

By voltage (7), its effective value U_s and phase shift relative to current $\varphi_s = \gamma_{Us} - \beta$ are found in exponential form $\underline{U}_s = U_s e^{j\gamma_{Us}}$.

After calculating the magnetic field and electromagnetic parameters in the considered load mode of the RMFI at $U_s = U_{sN}$ and indicated in Fig. 4 values I_s and β we obtain: $R_{mag} = 0.01207$ Ω; $\Psi_m = 0.376$ Wb; $\gamma_{\Psi a} = 15.08°$; $E_a = 83.6$ V; $\varphi_s = 73.5°$.

In [4, 5] it was revealed that when setting $\beta = 0$, the value $\gamma_{\Psi a}$ turned out to be the same, and this corresponded to the mode of operating idle, since the EMT was equal to zero, too. The angle of rotation of the magnetic flux linkage vector $\underline{\Psi}_a$ from the idle mode to the load mode, according to the theory of synchronous machines, is the load angle Θ. Therefore, the angle $\gamma_{\Psi a}$ in (4) is the load angle of the RMFI, i.e. $\Theta = \gamma_{\Psi a}$. The relationship of the angles β and Θ with each other, as well as with the load torque and other electromagnetic parameters of the inductor are presented in detail in [4, 5].

Determination of the current factor of filling the working chamber with ferromagnetic elements.

As an indicator of the filling of the working chamber, it is proposed to use the current of the stator winding, and more specifically, the change in the current of the phase winding. To identify such a possibility, a series of corresponding calculations of the magnetic field and electromagnetic parameters of the inductor was performed according to the above method with formulae (3) – (7).

The process of wear of ferromagnetic elements in this work is simulated in the simplest version by changing their length, which is already denoted as b_e, and the number of FEs in the chamber is considered unchanged.

Previously, the results of calculations have already been presented for a basic value of the length b_e equal to 20 mm and selected values of the angle β with the corresponding current I_s. Now, to this value of b_e, we add four more values of the FE length as it decreases with a step of 2 mm. And we carry out the calculations for a number of β values in order to obtain the angular characteristics of the inductor. In this case, naturally, the gaps d_y between the elements increase accordingly, and the diameter of the elements d_e and the gaps d_x between them remain the same.

Figure 6 shows the models of the modernized filling of the working chamber (symmetric quarters of the cross section) with the corresponding patterns of magnetic fields. For the basic filling option, a similar full image is shown in Fig. 4 and in the form of a fragment – in Fig. 5.
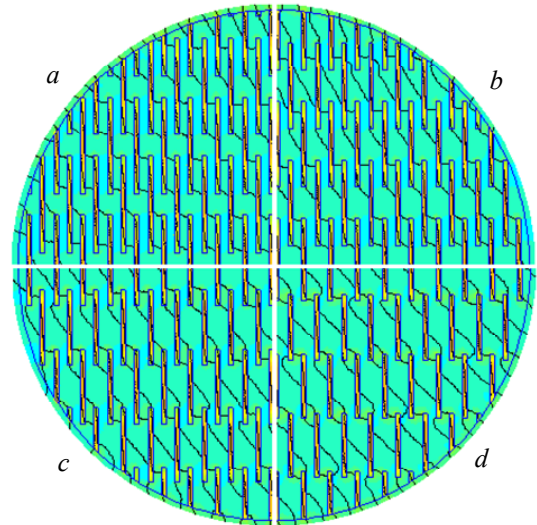
Fig. 6. Working chamber filling options
with a change in the length of the ferromagnetic elements:
$a - b_e$=18 mm; $b - b_e$=16 mm; $c - b_e$=14 mm; $d - b_e$=12 mm

With the accepted modifications of the FEs, the filling factor of the working chamber in the cross section K_{Fes} changes, but the filling factor in the longitudinal section K_{Fesz} remains, as in the basic version – K_{Fesb}. Then the volumetric filling factor of the chamber is defined as $K_{Fev} = K_{Fes} \cdot K_{Fesb}$.

The initial parameters of the five calculation options, namely: b_e, K_{Fes} and K_{Fev}, are given in Table 1.

At the given voltage of the stator winding for five specific options for filling the working chamber, the families of the two angular characteristics of the inductor required in this case were calculated, as in [5]: $I_s(\Theta)$ и $M_{em}(\Theta)$ – they are shown in Fig. 7.

Dependencies of the parameters of the inductor on the length
of ferromagnetic elements

Option	b_e, mm	K_{Fes}	K_{Fev}	I_s, A		E_a, V
				$M_{emo}=0$	M_{emN}	
1	20	0.322	0.104	35.0	36.0	83.6
2	18	0.290	0.094	38.4	39.4	82.6
3	16	0.256	0.082	41.1	42.1	81.1
4	14	0.226	0.073	43.5	44.1	80.1
5	12	0.193	0.062	45.8	46.5	79.1

Fig. 7. Plotting on angular characteristics of the
current I_s and EMT M_{em} to obtain the dependence $I_s(b_e)$
at nominal EMT M_{emN}

The technique for calculating the characteristics was
as follows.

The generalized initial phase of currents β included
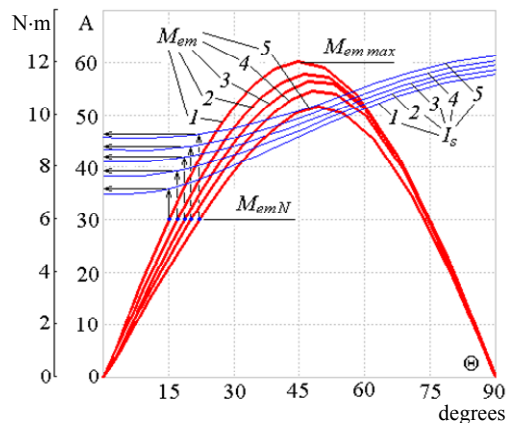in (1), which depends on the load level of the inductor
[4, 5], is taken as a variable value.

At an unchanged voltage U_s, for each value of the
angle β, the inverse problem of calculating the magnetic
field is solved resulting in the required value of the
current I_s. This solution, as shown in [5], is achieved by
the method of successive approximations with the
solution at each iteration of the direct problem – by
calculating the magnetic field for a given value of the
angle β and the selected value of the current I_s, and,
therefore, the known distribution of currents in the
windings according to (1).

At a specific value of the angle β, the initial
approximation of the current I_s is set and the magnetic
field is calculated, and as a result, using (7), the value of
the voltage U_s is obtained. It is compared with the set
value U_{sN} and the current value I_s is corrected depending
on the result. The iterations continue until the coincidence
of U_s and U_{sN} with the desired accuracy, which is
described in [5].

The characteristics of the inductor were calculated in
the range of angle β from 0 to 90° by passing it with a
step of 5°. For each β value, the corresponding values of
the current I_s, EMT M_{em}, EMF E_a and the load angle Θ
were determined, which is further taken as an argument
for the characteristics $I_s(\Theta)$ and $M_{em}(\Theta)$.

To reveal the dependence $I_s(b_e)$ at the nominal
electromagnetic torque M_{emN}, the constructions shown in
Fig. 7 are carried out. The M_{emN} value was 6 N·m, and it

was assumed to be equal to half the maximum torque
M_{emmax} at the base length of the ferromagnetic elements
b_e =20 mm.

The results obtained – the values of the current I_s at
M_{emN} and at the accepted values of b_e are summarized in
Table 1. Here are also given the values of the current I_s at
a zero value of the torque M_{emo}, which corresponds to the
previously described mode of the operating idle at $\beta = 0$.

Available now according to the Table 1 two
dependencies $I_s(b_e)$ at M_{emN} and M_{emo} are shown
graphically in Fig. 8. Obviously, all other permissible
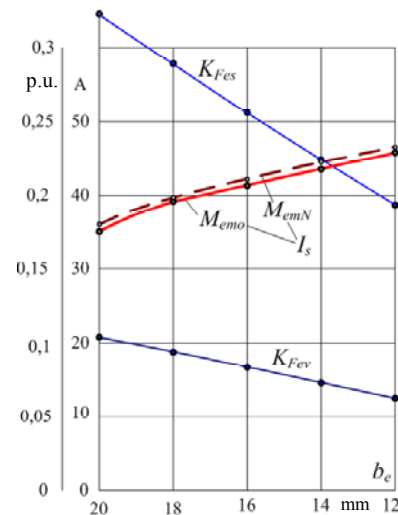modes of operation will be within the range between the
resulting two graphs.

Fig. 8. Dependencies of the filling factors of the working
chamber K_{Fes} and K_{Fev} and the stator winding current I_s on the
FE length b_e

Here, according to Table 1, the graphs of the
dependencies of the planar K_{Fes} and volumetric K_{Fev}
filling factors of the working chamber are also plotted.

Now according to the Table 1 and Fig. 8, it can be
seen that in the considered range of variation of the length
of the ferromagnetic elements, the stator winding current
will automatically change to a rather noticeable value of
about 10 A. It can be easy recorded continuously using an
ammeter or a special current sensor.

Thus, the operator controlling the inductor or the
automatic control system can determine the current value
of the filling factor of the working chamber with
ferromagnetic elements and, therefore, the moment in
time when it is necessary to replenish it with new
elements.

Also, in the Table 1 the column of the EMF of phase
stator winding E_a (6) is added. In the considered range of
variation in the length of ferromagnetic elements, this
EMF changed by 5.4 %. The EMF will also change to the
same extent of any measuring coils, which are used to
indicate the filling of the working chamber of the inductor
with ferromagnetic elements.

But the phase current at the same time changed to
29.2 % – therefore, this is namely a more visual and
sensitive indicator of the concentration of ferromagnetic
elements in the working chamber, that is, an indicator of
the volumetric filling factor of the working chamber K_{Fev}
which in Table 1 changed by 40 %.

The results obtained are qualitatively confirmed by experimental data on a simplified inductor model [6]. In the conditions of the studies carried out there, it was revealed that a decrease in the volumetric filling factor of the chamber from 0.037 to 0 led to an increase in the stator current by 13.4 %. The smaller change in comparison with the RMFI considered in the paper is explained by the significantly lower values of the filling factor k_{FeV}.

Conclusions.

1. The current method developed on the basis of numerical field calculations of magnetic fields makes it possible to relate the concentration of ferromagnetic elements in the working chamber of the rotating magnetic field inductor and the current in its winding.

2. Practical calculations on a specific sample of the inductor showed that the wear of the length of the ferromagnetic elements due to their abrasion by 40 % leads to an automatic increase in the phase current by 29.2 %. At the same time, the applied alternative control method by means of measuring coils requires a more complex inductor design and gives a decrease in EMF only by 5.4 %, that is, it has a much lower sensitivity.

3. Observation of the current of the inductor winding makes it possible to control the filling of its working chamber with ferromagnetic elements without interrupting the process of operation of the RMFI. This makes it possible to timely replenish the chamber with such elements and, thereby, maintain the technological processing of various substances passed through this chamber at a given level.

4. Despite the fact that the studies were carried out for a specific version of FE wear (length wear), the proposed method of current control of the filling of the working chamber with them can be applied for other wear options. For example, when the FEs are thinned, when the decreases in the length and thickness of the FEs are combined, or simply when the FEs are removed from the working chamber.

REFERENCES

1. Logvinenko D.D., Sheljakov O.P. *Intensifikacija tehnologicheskih processov v apparatah s vihrevym sloem* [Intensification of technological processes in apparatus with a vortex layer]. Kiev, Tehnika Publ., 1976. 144 p. (Rus).

2. Belounis A., Mehasni R., Ouil M., Feliachi M., El-Hadi Latreche M. Design with optimization of a magnetic separator for turbulent flowing liquid purifying applications. *IEEE Transactions on Magnetics*, 2015, vol. 51, no. 8, pp. 1-8. **doi: 10.1109/TMAG.2015.2424401.**

3. Gerasimov M.D., Loktionov I.O. Dual-use technological solutions. Application prospects. *Vektor GeoNauk*, 2019, vol. 2, no. 1, pp. 19-26. (Rus). **doi: 10.24411/2619-0761-2019-10003.**

4. Milykh V.I., Shilkova L.V. Numerical-field analysis of the characteristics of a three-phase magnetic field inductor for the treatment of various substances with current stabilization. *Electrical engineering & electromechanics*, 2019, no. 6, pp. 21-28. (Rus). **doi: 10.20998/2074-272X.2019.6.03.**

5. Milykh V.I., Shilkova L.V. Characteristics of a cylindrical inductor of a rotating magnetic field for technological purposes when it is powered from the mains at a given voltage. *Electrical engineering & electromechanics*, 2020, no.2, pp. 13-19. (Rus). **doi: 10.20998/2074-272X.2020.2.02**.

6. Milykh V.I., Shilkova L.V. Experimental research of the three-phase physical model of the magnetic field inductor in the working mode when processing bulk material. *Bulletin of NTU «KhPI». Series: «Electric machines and electromechanical energy conversion»*, 2020, no.3(1357), pp. 3-7. (Ukr). **doi: 10.20998/2409-9295.2020.3.01.**

7. *Finite Element Method Magnetics: OldVersions.* FEMM 4.2 11Oct2010 Self-Installing Executable. Available at: http://www.femm.info/wiki/OldVersions (accessed 15.06.2017).

8. Milykh V.I. The system of automated formation of electrical machines computational models for the FEMM software environment. *Technical Electrodynamics*, 2018, no.4, pp. 74-78. (Ukr). **doi: 10.15407/techned2018.04.074.**

9. Milykh V.I., Shilkova L.V. Revuzhenko S.A. Numerical analysis of the magnetic field of a cylindrical three-phase magnetic separator inductor. *Bulletin of NTU «KhPI». Series: «Electric machines and electromechanical energy conversion»*, 2017, no. 1(1223), pp. 76-82. (Ukr).

10. Milykh V.I., Shilkova L.V. Numerical-experimental analysis of the magnetic field of a magnetic separator inductor on the basis of an asynchronous motor. *Bulletin of NTU «KhPI». Series: «Electric machines and electromechanical energy conversion»*, 2018, no. 5(1281), pp. 104-109. (Ukr).

V.I. Milykh[1], *Doctor of Technical Science, Professor,*
L.V. Shilkova[1], *Postgraduate Student,*
[1] National Technical University «Kharkiv Polytechnic Institute», 2, Kyrpychova Str., Kharkiv, 61002, Ukraine,
e-mail: mvikemkpi@gmail.com, larisa_lv@ukr.net

S.Kh. Oshurbekov, V.M. Kazakbaev, V.A. Prakht, V.A. Dmitrievskii, A.S. Paramonov

ANALYSIS OF ELECTRICITY CONSUMPTION OF INDUCTION MOTORS OF IE1 AND IE2 EFFICIENCY CLASSES IN A 11 kW PUMP INSTALLATION

Purpose. Comparative analysis of energy consumption indicators of electric motors of different energy efficiency classes in an electric drive of a centrifugal pump with power of 11 kW of a water supply system with throttle regulation. Methodology. In this paper a comparison of energy consumption of 11 kW pump units with induction motors of energy efficiency classes IE1 and IE2 is presented. The induction motors are powered directly from the mains. Both considered pump configurations have the same fluid flow rate characteristic of open pump systems. The amount of water consumed by the pump is adjusted by throttling. Results. The results on the daily and annual energy consumption of the two considered pump system configurations are obtained. It is shown that the pump unit using the IE2 class motor provides the annual energy savings of 9.65 thousand rubles and the life cycle energy savings of 158 thousand rubles compared to the IE1 class motor. The payback period of the IE2 class motor is calculated, which is 5 months if a new installation is commissioned and 2 years if the motor is replaced in an operating installation. Practical value. Nowadays the countries of the Eurasian Economic Union mainly use electric motors of the lowest energy efficiency class IE1, according to the IEC 60034-30 Standard (GOST IEC 60034-30-1-2016). However, according to the decision of the Commission of the Eurasian Economic Union, since the 1st of September, 2021 all general-purpose motors shall not be less efficient than the IE2 efficiency level. Therefore, the analysis of the economic effect of replacing IE1 class motors with IE2 class motors becomes relevant for the countries of the Eurasian Union. Pump drives are one of the most important consumers of electricity. Most of the pump drives are powered directly from the mains. References 25, tables 5, figures 4.

На сьогоднішній день в країнах Євразійського економічного союзу в основному застосовуються електродвигуни низького класу енергоефективності IE1, відповідно до стандарту МЕК 60034-30 (ГОСТ МЕК 60034-30-1-2016). Однак, згідно з рішенням комісії Євразійського економічного союзу, з 1 вересня 2021 р значення коефіцієнта корисної дії двигунів не повинно бути менше значень, встановлених для класу енергетичної ефективності IE2. Тому для країн Євразійського союзу актуальним стає аналіз економічного ефекту від заміни двигунів класу IE1 на двигуни класу IE2. У даній роботі представлений порівняльний аналіз показників енергоспоживання асинхронних електродвигунів класів енергоефективності IE1 і IE2 в електроприводі відцентрового насоса потужністю 11 кВт системи водопостачання з дросельним регулюванням. Асинхронні двигуни живляться безпосередньо від електричної мережі. Обидві насосні системи мають один і той же графік витрати рідини, характерний для розімкнутих насосних систем. Кількість витрачається насосом води регулюється за рахунок дроселювання. Отримано результати по добовому і річному енергоспоживанню двох розглянутих конфігурацій насосної системи. Показано що система, де застосовується асинхронний двигун класу енергоефективності IE2, забезпечує економію 118,6 євро за рік і 2000 євро за життєвий цикл, в порівнянні з асинхронним двигуном класу IE1. Розрахований термін окупності двигуна класу IE2, який складає 5 місяців в разі введення в дію нової установки і 2 роки, в разі заміни двигуна в працюючій установці. Бібл. 25, табл. 5, рис. 4.

На сегодняшний день в странах Евразийского экономического союза в основном применяются электродвигатели низкого класса энергоэффективности IE1, согласно стандарту МЭК 60034-30 (ГОСТ МЭК 60034-30-1-2016). Однако, согласно решению комиссии Евразийского экономического союза, с 1 сентября 2021 г. значение коэффициента полезного действия двигателей не должно быть меньше значений, установленных для класса энергетической эффективности IE2. Поэтому для стран Евразийского союза актуальным становится анализ экономического эффекта от замены двигателей класса IE1 на двигатели класса IE2. В данной работе представлен сравнительный анализ показателей энергопотребления асинхронных электродвигателей классов энергоэффективности IE1 и IE2 в электроприводе центробежного насоса мощностью 11 кВт системы водоснабжения с дроссельным регулированием. Асинхронные двигатели питаются напрямую от электрической сети. Обе насосные системы имеют один и тот же график расхода жидкости, характерный для разомкнутых насосных систем. Количество расходуемой насосом воды регулируется за счет дросселирования. Получены результаты по суточному и годовому энергопотреблению двух рассмотренных конфигураций насосной системы. Показано что система, где применяется асинхронный двигатель класса энергоэффективности IE2, обеспечивает экономию 118,6 евро за год и 2000 евро за жизненный цикл, по сравнению с асинхронным двигателем класса IE1. Рассчитан срок окупаемости двигателя класса IE2, который

составляет 5 месяцев в случае введения в строй новой установки и 2 года, в случае замены двигателя в работающей установке. Библ. 25, табл. 5, рис. 4.

Ключевые слова: **асинхронный двигатель, дроссельное регулирование, срок окупаемости, центробежный насос, энергоэффективность, энергопотребление.**

Introduction. The high energy intensity of modern industry determines the high urgency of increasing the energy efficiency of production. Electric motors consume about 70 % of the electricity in industrial applications. Therefore, in many countries around the world, a ban is gradually being introduced on the use of motors with low energy efficiency classes. However, in Russia today, mainly electric motors of low energy efficiency class IE1, in accordance with the IEC 60034-30 Standard, are used. Motors of IE2 class of domestic production are also presented on the Russian market [1]. However, the demand for energy efficient motors in Russia is small due to the low cost of electricity compared to the countries of the European Union. For comparison, the price of electricity for industrial consumers in Germany is about 0.2 EUR/kW·h, while in Russia it is only about 0.057 EUR/kW·h [2, 3].

In the European Union, since 2017, in general industrial applications, it is permissible to use motors of classes not lower than IE3, for power of 0.75-375 kW. Moreover, since the 1st of July, 2023 in the European Union, motors with power of more than 75 kW must comply with the IE4 class [4]. In the future, there are plans to expand the mandatory class IE4 for lower power motors and move to the mandatory class IE5 for powerful motors [5]. It should be noted that even in modern conditions, the use of IE4 and IE5 class motors can be justified due to high, constantly increasing prices for energy carriers and the need to reduce the impact on the environment [6].

The massive use of motors of higher energy efficiency classes will significantly reduce energy consumption, reduce the energy intensity of the gross domestic product, and will also contribute to improving the environmental situation by reducing the emission of harmful substances during electricity generation. The use of energy-efficient motors is consistent with the achievement of the goals stated in the energy and environmental strategies of various countries: the European Union (European Green Deal [6]), the USA (State Energy Program), Switzerland (supports the Paris Agreement), China (supports the Paris Agreement), Japan (Net Zero Energy Building), South Korea (supports the Paris Agreement), as well as the Russian Federation [7], etc.

Therefore, according to the decision of the Commission of the Eurasian Economic Union on the requirements for the energy efficiency of energy-consuming devices [8], since the 1st of September, 2021

the efficiency value for motors with power of 0.75-375 kW should not be less than the values established for the IE2 energy efficiency class. And from the 1st of September, 2023 the efficiency of motors with power of 7.5-375 kW should already correspond to the IE3 class. The IE3 class requirement since the 1st September 1, 2025 will also be extended to 0.75-7.5 kW motors [8].

The obligatory transition to IE2 class motors in Russia and the countries of the Eurasian Economic Union makes it possible to hope that in the future, albeit with a certain time delay due to objective economic reasons, the requirements for the energy efficiency of motors will approach the modern requirements of the European Union.

Pump systems consume about 22 % of the world's electricity [9]. A large number of works [10-16] are devoted to the issues of comparing the energy consumption of pump systems using different motors with different IE classes. However, all of these papers deal with pump systems with motor speed control using a frequency converter. Despite the high efficiency, as well as the best static and dynamic control characteristics of the AC drive with a frequency converter, due to the high cost of the converter, most of the pump drives are still powered directly from the mains [9]. For example, the share of variable speed drives in the German market is about 30 %, and in the Swiss market – 20 % [17]. In Russia and other CIS countries, the share of variable frequency drives is traditionally lower than in the European Union.

For pumps powered directly from the mains, the comparison of energy consumption when using motors with different IE classes is considered much less often. Or example, in [9] a comparative analysis of the energy consumption of synchronous and induction motors of IE3 and IE4 classes with direct power supply from the network in the electric drive of a centrifugal pump with throttle control is considered. It is also shown in [9] that when choosing a motor, it is necessary to take into account not only the energy efficiency class, but also the load cycle in which the motor operates, and, accordingly, the efficiency of the motor at reduced loads. However, the use of motors of classes IE3 and IE4 is currently not legally supported in all countries.

Based on the above **literature review**, it can be concluded that the issues of comparing motors of different energy efficiency classes in pump units with an uncontrolled speed remain insufficient highlighted.

The goal of this work is a comparative analysis of the energy consumption of 11 kW direct-on-line induction motors with energy efficiency classes IE1 and IE2 in an electric drive of a throttle-controlled centrifugal pump.

The urgency of this work is due to the need to assess the economic effect of replacing IE1 class motors with IE2 class motors for such a common class of mechanisms as centrifugal pumps, in view of the imminent introduction of the mandatory use of IE2 class motors in the countries of the Eurasian Union. For comparison, the energy consumption indicators and the costs of motors of the IE1 and IE2 classes over the life cycle are compared, the payback period of the IE2 class motor is analyzed. In [18], such an analysis was carried out for the particular case of a 15 kW pump unit. This work expands on this analysis.
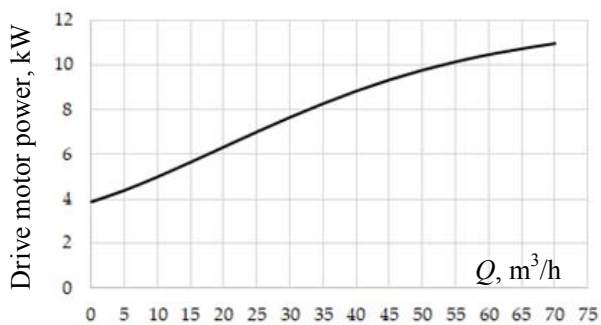
Pump characteristics. For the calculation, a Calpeda NM 50/20A/ B pump with power of 11 kW was selected [19]. The rated speed of the pump is 2900 rpm.

The maximum performance of the pump system corresponds to the point at which the water flow rate is 10 % higher than at the point with the best efficiency point (BEP) $Q_{110\%} = 1.1 \cdot Q_{bep} = 66$ m^3/ h.

Figure 1,*a* shows the catalog *Q-H* characteristic of the pump [19], and Fig. 1,*b* presents the dependence of the mechanical power of the pump drive motor depending on the water supply at the rated speed [19].
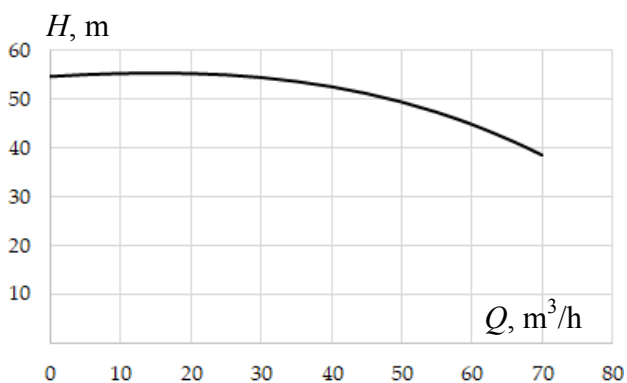
a – Q-H pump characteristic

b – required mechanical power of the motor depending on the flow rate

Fig. 1

Characteristics of induction motors. For the calculation the asynchronous motors of Russian production: 7AVEC160M2ie1 (class IE1) and 7AVEC160M2ie2 (class IE2) of the 7AVE series [1] with power of 11 kW were selected. The efficiency values of these motors in the nominal mode are equal to 88.2 % and 90 %, respectively.

Table 1 shows data on the efficiency of the selected motors in 5 different load modes. P_{mech} is the mechanical power of the motor; P_n is the rated mechanical power of the motor. These data are also shown in Fig. 2.

Table 1

Motor efficiency data

Motor	Motor efficiency, %				
	$P_{mech} = 0.25 \cdot P_n$	$P_{mech} = 0.5 \cdot P_n$	$P_{mech} = 0.75 \cdot P_n$	$P_{mech} = P_n$	$P_{mech} = 1.25 \cdot P_n$
IM IE1	79.5	86.6	88.4	88.2	85.8
IM IE2	83.8	89.2	90.4	90	88.5
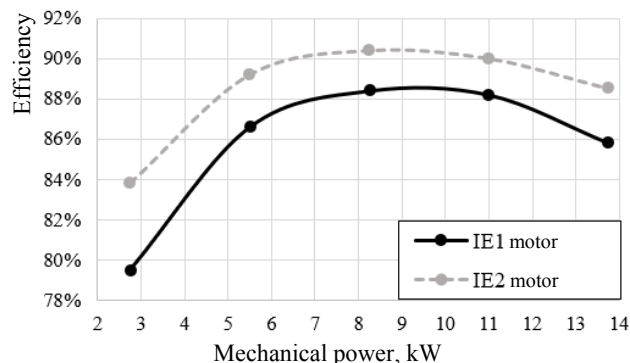
Fig. 2. Efficiency curves of motors

Pump working points. An open-loop pumping system is considered, the water flow rate of which varies in the range from 75 % to 110 % of the flow rate Q_{bep}, which corresponds to the working point of the pump with the highest efficiency (the best efficiency point, BEP). 25 % of the time the pump operates at a point with a flow rate of $0.75 \cdot Q_{bep}$, 50 % of the time – with a flow rate Q_{bep}, and another 25 % of the time – with a flow rate of $1.1 \cdot Q_{bep}$. This dependence is diagrammatically shown in Fig. 3. This load curve is recommended by the Europump manufacturer association for estimating the energy consumption of pumps with fixed drive [20].

At the maximum water flow rate ($Q = 1.1 \cdot Q_{bep}$), the valve is fully opened, and to ensure flow rates equal to Q_{bep} and $0.75 \cdot Q_{bep}$, the valve is partially closed so that the system characteristic changes, and the point of its intersection with the pump characteristic moves to the left. Figure 4 shows the *Q-H* characteristic of the pump and the characteristics of the hydraulic system at various working points.

Fig. 3. Water flow rate diagram per cycle [20]

Fig. 4. *Q-H* characteristic of the pump and curves of the system

To assess energy consumption, the mechanical power of the drive motor is first calculated, in three modes shown in Fig. 3. When regulating the water flow by throttling, the working points of the pump system move along Q-*H* pump characteristic by measuring the characteristic of the hydraulic system. The characteristic of the hydraulic system is described by the following equation [9]:

$$H = H_{st} + k \cdot Q^2, \qquad (1)$$

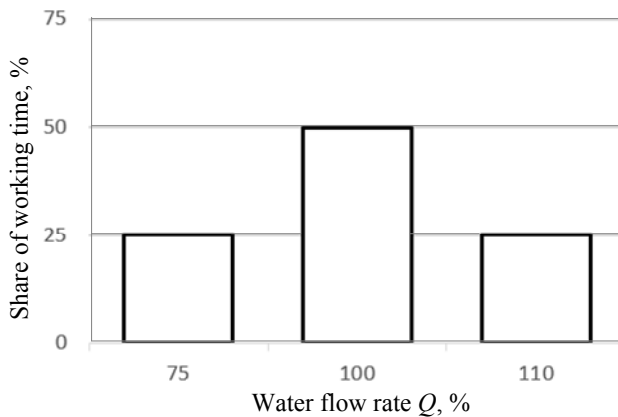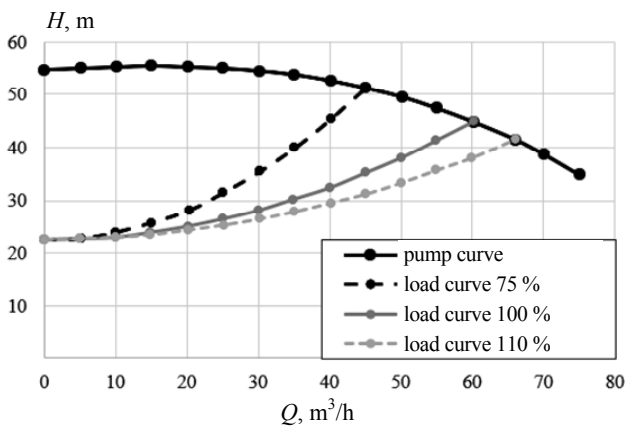where Q and H are the required values of water supply and pressure of the hydraulic system (hydraulic load); H_{st} is the static pressure of the hydraulic system ($H_{st} = H_{bep} / 2 = 22.5$ m); k is the coefficient of friction of the hydraulic system, the value of which depends on the value of the valve opening.

Table 2 shows the results of calculating the mechanical power (P_{mech}) and other characteristics of the pump at three different water flow rates corresponding to Fig. 3.

The coefficient of friction for different Q is calculated based on (1) as $k = (H - H_{st}) / Q^2$.

Table 2

Pump cycle data

Q, %	k, h²/m⁵	Q, m³/h	H, m	Pump efficiency, %	Pmech, kW
75	0.014	45	51.31	67.3	9.35
100	0.006	60	45.00	70.3	10.47
110	0.004	66	41.47	69.2	10.78

The pump efficiency is calculated as P_{hydr} / P_{mech}, where $P_{hydr} = \rho \cdot g \cdot H \cdot Q$ is the hydraulic power of the pump; $\rho = 1000$ kg/m³ is the density of the liquid; $g = 9.81$ m/s² is the acceleration of gravity; P_{mech} is determined according to the dependence shown in Fig. 1,*b*.

Power consumption of the pump unit. Efficiency values of motors at different working points (Table 3) are found according to the dependencies shown in Fig. 2.

Table 3

Efficiency of motors at the considered working points of the pump

Q, %	Pmech, kW	Motor efficiency, %	
		IE1 IM	IE2 IM
75	9.35	88.32	90.24
100	10.47	88.24	90.08
110	10.78	88.22	90.03

Using the data from Table 3, it is possible to find the values of the consumed electrical power at the considered working points, according to the formula:

$$P_1 = P_{mech} / \eta_{motor}, \qquad (2)$$

where η_{motor} is the motor efficiency.

The results of this calculation are shown in Table 4, in which $i = 1..3$ is the number of the considered load point.

Table 4

Electrical power consumed by the motors at the considered working points of the pump

i	Q, %	tᵢ/ tsum, %	P₁, kW	
			IM class IE1	IM class IE2
1	75	25	10.585	10.360
2	100	50	11.865	11.623
3	110	25	12.223	11.997

Using the results obtained (see Table 4), we calculate the daily electricity consumed (E_{day}), the annual electricity consumed (E_{year}), the sum of the annual energy costs (C_{year}) and the annual savings (S_{year}) for a pump system with an IE2 motor, compared to pump system with an IE1 class motor [9]:

$$E_{day} = \frac{t_{sum}}{1000} \cdot \sum_{i=1}^{3}\left(P_{1i} \cdot \frac{t_i}{t_{sum}} \right); \qquad (3)$$

$$E_{year} = E_{day} \cdot 365; \qquad (4)$$

$$C_{year} = E_{year} \cdot GT; \qquad (5)$$

$$S_{year} = C_{year\,1} - C_{year\,2}, \qquad (6)$$

where t_i / t_{sum} is the share of the working time of the i-th operating mode; t_{sum} is the working cycle duration (24 h); $GT = 0.057$ EUR/kW·h is the electricity tariff in Russia for 1 kW·h for industry (Moscow, 2019) [2]; C_{year1} and C_{year2} are the sum of annual energy costs of the first (when using an IE1 class motor) and second (IE2 class motor) pump systems configuration.

We also estimate the energy consumption over the entire life cycle of the pump system, which is usually 20 years [21]. Estimation of the cost of energy during the entire life cycle of the pump system is determined by the following formula [21]:

$$C_{lcc} = \sum_{m=1}^{n}\left(\frac{C_{year\,m}}{\left(1 + [y - p]^m\right)} \right), \qquad (7)$$

where $C_{year\,m}$ is the sum of electricity costs of the m-th year; y is the interest rate of the Central Bank ($y = 0.06$); p is the expected annual inflation ($p = 0.04$); n is the service life of the system ($n = 20$ years).

The calculation results by (3) – (7) are shown in Table 5.

Table 5
Comparison of energy consumption parameters

Parameters	E_{day}, kW·h	E_{year}, kW·h	C_{year}, EUR	S_{year}, EUR/h	C_{lcc}, thousand EUR
IE1 IM	279.2	101921	5 809	–	95.0
IE2 IM	273.5	99827	5 690	118.6	93.0

As it can be seen from the Table 5, annual savings S_{year} are EUR 118.6 with the IE2 motor compared to the IE1 motor. The savings over 20 years (difference in C_{lcc} of the two engines) are 2,000 EUR taking into account interest rates and inflation.

Also, based on the data obtained, we calculate the payback period when using an IE2 class motor. According to [22], the difference in the cost of active materials for an induction motor 7AVE with power of 13 kW and class IE1 and IE2 is only 6.7 % (in [22] there is no data on active materials for a motor with power 11 kW). However, the difference in the market price of induction electric motors of neighboring energy efficiency classes of the 7AVE series [1], according to [23], is 20-25 %. We calculate the payback period for two cases:

1) when a new pump unit is put into operation with the use of IE2 IM instead of IE1 IM;

2) when replacing the IE1 class IM with the IE2 class IM in a pump unit in operation.

In the first case, the payback period is defined as the ratio of the difference in the cost of IE1 and IE2 class motors to the annual energy savings [24] (8):

$$T = (C_{m2} - C_{m1}) / S_{year}, \qquad (8)$$

where T is the value of the payback period of the system, year; $C_{m1} = 194.21$ EUR is the cost of an induction motor of class IE1 [25]; $C_{m2} = 1.25 \cdot C_{m1} = 242.76$ EUR is the cost of an induction motor of class IE2 [23].

In the second case, we calculate the payback period as (9):

$$T = C_{m2} / S_{year}. \qquad (9)$$

The payback periods, calculated according to (8), (9), are 0.41 years (approximately 5 months) when a new pump unit with IM IE2 is put into operation and 2.03 years when the IM of the IE1 class is replaced by the IM of the IE2 class in the existing unit.

Conclusions.

This paper compares the energy efficiency indicators of a pump unit with power of 11 kW when using induction motors of IE1 and IE2 classes. In both cases, the same flow rate graph is considered, typical for open-loop pump systems. The flow rate is regulated by throttling the pipeline.

It is shown that a system using an IE2 class induction motor saves EUR 118.6 per year and EUR 2,000 (including the interest rate and inflation) per life cycle, compared to a system using an IE1 class induction motor.

The payback period when using a more expensive IE2 class motor instead of an IE1 class motor is 5 months when a new pump unit is put into operation and 2.03 years when replacing motors in a pump unit in operation.

The short payback period for the first case allows to conclude that the use of IE2 motors in new installations is very profitable at current prices for motors and electricity.

REFERENCES
1. Technical catalog. Series of low-voltage asynchronous motors 7AVE, dimensions 160-315mm, energy efficiency classes IE1, IE2, IE3. Available at: http://www.xn--h1aambls2f.xn--p1ai/produkcziya/elektrodvigateli/nizkovoltnye-asinhronnye-dvigateli-7ave/ (accessed 01 May 2020). (Rus).
2. Electricity tariffs for medium-sized enterprises in 2020. Available at: https://time2save.ru/articles/tarify-na-elektroenergiyu-dlya-srednih-predpriyatiy-v-2018 (accessed on 11 July 2020). (Rus).

3. Eurostat Data for the Industrial Consumers in Germany. Available at: https://appsso.eurostat.ec.europa.eu/nui/show.do?dataset=nrg_pc_205&lang=en.

4. Commission Regulation (EU) 2019/1781 of 1 October 2019 laying down ecodesign requirements for electric motors and variable speed drives pursuant to Directive 2009/125/EC of the European Parliament and of the Council, amending Regulation (EC) No 641/2009 with regard to ecodesign requirements for glandless standalone circulators and glandless circulators integrated in products and repealing Commission Regulation (EC) No 640/2009, Document 32019R1781. Available at: https://eur-lex.europa.eu/eli/reg/2019/1781/oj.

5. Doppelbauer M. Update on IEC motor and converter standards. *6th International Motor Summit for Energy Efficiency powered by Impact Energy*, Motor Summit, 2016.

6. Annex to the Communication from the Commission to the European Parliament, the European Council, the Council, the European Economic and Social Committee and the Committee of the Regions. The European Green Deal. Brussels, 11.12.2019, COM (2019) 640 final. Available at: https://ec.europa.eu/info/sites/info/files/european-green-deal-communication-annex-roadmap_en.pdf.

7. Long-term development strategy of the Russian Federation with low greenhouse gas emissions until 2050. Available at: https://economy.gov.ru/material/file/babacbb75d32d90e28d3298582d13a75/proekt_strategii.pdf (accessed 20 March 2020). (Rus).

8. Decision of the Council of the Eurasian Economic Commission of August 8, 2019 no. 114 «On the technical regulation of the Eurasian Economic Union «On requirements for the energy efficiency of energy-consuming devices». Available at: https://www.garant.ru/products/ipo/prime/doc/73240518 (accessed 11 May 2020). (Rus).

9. Goman V.V., Oshurbekov S.Kh., Kazakbaev V.M., Prakht V.A., Dmitrievskii V.A. Comparison of energy consumption of various electrical motors operating in a pumping unit. *Electrical engineering & electromechanics*, 2020, no. 1, pp. 16-24. **doi: 10.20998/2074-272X.2020.1.03.**

10. Ahonen T., Orozco S.M., Ahola J., Tolvanen J. Effect of electric motor efficiency and sizing on the energy efficiency in pumping systems. *2016 18th European Conference on Power Electronics and Applications (EPE'16 ECCE Europe)*, Sep. 2016, Karlsruhe, pp. 1-9. **doi: 10.1109/EPE.2016.7695671.**

11. Van Rhyn P., Pretorius J.H.C. Utilising high and premium efficiency three phase motors with VFDs in a public water supply system. *2015 IEEE 5th International Conference on Power Engineering, Energy and Electrical Drives (POWERENG)*, May 2015, Riga, pp. 497-502. **doi: 10.1109/PowerEng.2015.7266367.**

12. Brinner T.R., McCoy R.H., Kopecky T. Induction versus permanent-magnet motors for electric submersible pump field and laboratory comparisons. *IEEE Transactions on Industry Applications*, 2014, vol. 50, no. 1, pp. 174-181. **doi: 10.1109/TIA.2013.2288203.**

13. Safin N., Kazakbaev V., Prakht V., Dmitrievskii V., Sarapulov S. Interpolation and analysis of the efficiency of a synchronous reluctance electric drive at various load points of a fan profile. *2018 25th International Workshop on Electric Drives: Optimization in Control of Electric Drives (IWED)*, Moscow, 2018, pp. 1-5. **doi: 10.1109/IWED.2018.8321372.**

14. Kazakbaev V., Prakht V., Dmitrievskii V., Ibrahim M., Oshurbekov S., Sarapulov S. Efficiency Analysis of Low Electric Power Drives Employing Induction and Synchronous Reluctance Motors in Pump Applications. *Energies*, 2019, vol. 12, no. 6, p. 1144. **doi: 10.3390/en12061144.**

15. Kazakbaev V.M., Prakht V.A., Dmitrievskii V.A. A comparative performance analysis of induction and synchronous reluctant motors in an adjustable-speed electric drive. *Russian Electrical Engineering*, 2017, vol. 88, no. 4, pp. 233-238. **doi: 10.3103/s106837121704009.**

16. Kazakbaev V., Prakht V., Dmitrievskii V., Sarapulov S., Askerov D. Comparison of power consumption of synchronous reluctance and induction motor drives in a 0.75 kW pump unit. *2017 International Siberian Conference on Control and Communications (SIBCON)*, Jun. 2017, Astana, pp. 1-6. **doi: 10.1109/SIBCON.2017.7998485.**

17. Phillips R., Tieben R. Improvement of Electric Motor Systems in Industry (IEMSI). *Proceedings of the 10th international conference on energy efficiency in motor driven systems (EEMODS' 2017)*, Rome, Italy, September 6-8, 2017. pp. 53-67. **doi: 10.2760/345473.**

18. Oshurbekov S., Kazakbaev V., Prakht V., Dmitrievskii V. Comparative Study of Energy Consumption of 15 kW Induction Motors of IE1 and IE2 Efficiency Classes in Pump Applications. *Proceedings of 2020 XI International Conference on Electrical Power Drive Systems (ICEPDS)*, Saint-Petersburg, Russia, 2020, October 04-07, pp. 1-6. (*Accepted for publication*).

19. NM, NMS, Close Coupled Centrifugal Pumps with Flanged Connections; Catalogue; Calpeda, 2018. Available at: https://www.calpeda.com/system/products/catalogue_50hzs/53/en/NM_NMS_EN2018.pdf?1549893188 (accessed 23 March 2019).

20. Extended product approach for pumps, Copyright © 2014 by Europump. Published by Europump.

21. Pump Life Cycle Costs: A Guide to LCC Analysis for Pumping Systems. Executive Summary. Hydraulic Institute (Parsippany, NJ); Europump (Brussels, Belgium); Office of Industrial Technologies Energy Efficiency and Renewable Energy U.S. Department of Energy (Washington, DC). January 2001, pp. 1–19. Available at: https://www.energy.gov/sites/prod/files/2014/05/f16/pumplcc_1001.pdf.

22. Bespalov V.Y., Kobelev A.S., Kruglikov O.V., Makarov L.N. Constructing and mastering the production of energy-efficient asynchronous motors of mass-market series. *Russian Electrical Engineering*, 2015, vol. 86, no. 4, pp. 194-200. **doi: 10.3103/S1068371215040033.**

23. Kobelev A.S. Cast copper rotor motors: between the price and the performance. *Constructor. Mechanical engineer Journal*, 2020. Available at: https://konstruktor.net/podrobnee-elekt/dvigateli-s-litym-mednym-rotorom-shpagat-mezhdu-cenoj-i-ehffektivnostju-2464.html (Accessed 11 May 2020). (Rus).

24. Tyuteva P.V. Algorithm for evaluating the energy efficiency of asynchronous motors in pumping units. *Bulletin of the Tomsk Polytechnic University*, 2009, vol. 315, no. 4, pp. 75-79. (Rus).
25. *Price list, induction motors of the AIR series, class IE1.* Available at: http://www.a-a-a.ru/01-pr.html (Accessed 22 June 2020). (Rus).

Received 12.07.2020

S.Kh. Oshurbekov[1],
V.M. Kazakbaev[1], *Candidate of Technical Science,*
V.A. Prakht[1], *Candidate of Technical Science,*
V.A. Dmitrievskii[1], *Candidate of Technical Science,*
A.S. Paramonov[1],
[1] Ural Federal University,
19, Mira Str., Ekaterinburg, 620002, Russia,
e-mail: safarbek.oshurbekov@urfu.ru,
vadim.kazakbaev@urfu.ru,
va.prakht@urfu.ru,
vladimir.dmitrievsky@urfu.ru,
paramonov.aleksey@inbox.ru

B.I. Kuznetsov, T.B. Nikitina, I.V. Bovdui

STRUCTURAL-PARAMETRIC SYNTHESIS OF ROLLING MILLS MULTI-MOTOR ELECTRIC DRIVES

Aim. Improving of control accuracy by rolling strip thickness and tension and reducing of sensitivity to changes of plant parameters based on structural-parametric synthesis of robust control by rolling mills multi-motor electric drives with parametric uncertainty. Methodology. The method of structural-parametric synthesis of robust control by rolling mills multi-motor electric drives with parametric uncertainty which improves control accuracy by rolling strip thickness and tension and reducing of sensitivity to changes of plant parameters is developed. The method based on the multi-criteria game decision in which payoff vectors are dispersions of longitudinal thickness and tension of the rolled. The calculation of the payoff vector associated with modeling of the synthesized system with different input signals and for various values of the plant parameters for various modes of operation of the system. The multi criterion game solution is calculated based on particles multiswarm optimization algorithms. Results. The results of the structural-parametric synthesis of robust control by 740 three-stand cold rolling mills multi-motor electric drives are presented. Comparisons of the strip thickness and tension accuracy of the synthesized robust system with the existing system are completed. It is showed that the use of synthesized robust controllers allowed to improve strip thickness and tension accuracy and reduce the sensitivity of the system to changes of plant parameters in comparison with the existing system. Originality. For the first time the method of structural-parametric synthesis of robust control by rolling mills multi-motor electric drives with parametric uncertainty based on multi-criteria game decision and particles multiswarm optimization algorithms to improve the control accuracy by rolling strip thickness and tension and to reduce of sensitivity to changes of plant parameters is developed. Practical value. Practical recommendations on reasonable choice of the structure and parameters of robust control by 740 three-stand cold rolling mills multi-motor electric drives to improving of control accuracy by rolling strip thickness and tension and reducing of sensitivity to changes of plant parameters are given. References 20, figures 2.
Key words: **rolling mill, multi-motor electric drive, rolling strip thickness and tension control, computer simulation.**

Цель. Повышение точности регулирования толщины и натяжения прокатываемой полосы и снижение чувствительности к изменениям параметров объекта управления на основе структурно-параметрического синтеза робастного управления многодвигательными электроприводами прокатных станов с параметрической неопределенностью. Методология. Разработан метод структурно-параметрического синтеза робастного управления многодвигательными электроприводами прокатных станов с параметрической неопределенностью, который позволяет повысить точность регулирования толщины и натяжения прокатываемой полосы и снизить чувствительность к изменениям параметров объекта управления. Метод основан на решении многокритериальной игры, в которой вектором выигрыша являются дисперсии продольной толщины и натяжения прокатываемой полосы. Вычисление вектора выигрыша связано с моделированием синтезированной системы при различных входных сигналах, для различных значений параметров объекта управления и в различных режимах работы. Решение многокритериальной игры основано на алгоритмах оптимизации роем частиц. Результаты. Приводятся результаты структурно-параметрического синтеза робастного управления многодвигательным электроприводом трехклетьевого стана холодной прокатки 740. Проведено сравнение точности регулирования толщины и натяжения полосы в синтезированной робастной и в существующей системах. Показано, что применение синтезированного робастного регулятора позволило повысить точность регулирования толщины и натяжения полосы и снизить чувствительность системы к изменениям параметров объекта управления по сравнению с существующей системой. Оригинальность. Впервые разработан метод структурно-параметрического синтеза робастного управления многодвигательными электроприводами прокатных станов с параметрической неопределенностью на основе решения многокритериальной игры и алгоритмов оптимизации роем частиц для повышения точности регулирования толщины и натяжения прокатываемой полосы и снижения чувствительности к изменениям параметров объекта управления. Практическая ценность. Даны практические рекомендации по обоснованному выбору структуры и параметров робастного управления трехклетьевым станом холодной прокатки 740 для повышения точности регулирования толщины и натяжения прокатываемой полосы и снижение чувствительности к изменениям параметров объекта управления. Библ. 20, рис. 2.
Ключевые слова: **прокатный стан, многодвигательный электропривод, регулирование толщины и натяжения прокатываемой полосы, компьютерное моделирование.**

Introduction. A rolling mill is complex multi-motor unit in which individual stands are interconnected by a rolling metal strip [1-5]. The multi stands rolling rolls rates using the main electric drives must be strictly coordinated to maintain a given strip tension in the inter-chain spaces. In addition, in hot rolling mills, loopers electric drives are used to control by strip tension. The strip tension is controlled by a simultaneous change the looper elevation angle and a coordinated change of the rolls rates of the previous and subsequent stands [6-9]. By means of front and rear winders, the specified strip tension at the inlet and outlet of the rolling mill is controlled. Regulation of the rolling rolls position is carried out with the help of electric drives of pressure screws [10-14].

The regulation system uses gauges of thickness, tension and speed of movement of the rolled strip at the inlet and outlet of the rolling mill, as well as in the inter-clearances [15-18].

The rolling process is accompanied by fluctuations in technological parameters – thickness, rolling pressure, strip tension, etc. Moreover, if the fluctuations in the strip thickness are caused by both the unevenness of the

thickness and mechanical properties of the rolled products, as well as by the eccentricities of the rolls of the rolling stand, then the fluctuations in the strip tension and proportional fluctuations in the currents of the main drives are due to the presence of elastic elements in the transmissions of the rolling moment from the drive motor to the rolling roll.

Fluctuations of the rolling mill rolls due to the presence of elastic elements (natural vibrations) have a decisive influence on the quality of the rolled products and are referred to as «vibrations». At the same time, in rolling mills, the frequencies of natural vibrations are in the range of 10-70 Hz [16–18].

The strip tension is influenced to the output strip thickness, so there is a fundamental possibility of «thin» thickness control by influencing the peripheral of the rolls rates (the main drives rates). In addition, the strip tension contributes to the production of a higher quality of strip with respect to the thickness difference in the strip width, which obtained due to the uneven production of work rolls «barrels».

Strip tension is an important technological factor that ensures the normal operation of the entire mill. The strip tension is a complex function of the speed difference of two adjacent stands and created due to the traction force of the drive motor of each subsequent stand. With a change in tension, the pressure of the metal on the rolls changes: with an increase in tension, the pressure of the metal on the rolls decreases, with a decrease in tension, the pressure increases. This is true for both front and rear strip tension changes. A metal pressure change on the rolls, in turn, leads to a change in the elastic deformation of the cage elements, i.e. at the same position of the pressure screws, the output strip thickness may be different.

Therefore, the design of advanced automatic control systems for a rolling mill requires the consideration of a multi- motor electromechanical mill system as a single electromechanical system. The synthesis of control systems by geometric parameters of multi-strand rolling mill is a complex problem that has a high dimension and cannot be solved by traditional methods.

The purpose of the work is improving of control accuracy by rolling strip thickness and tension and reducing of sensitivity to changes of plant parameters based on structural-parametric synthesis of robust control by rolling mills multi-motor electric drives with parametric uncertainty.

Problem statement. Let us consider the main provisions of the concept for design of automated control by rolling technological processes based on the synthesis of a two-level optimal control, which allows to synthesize optimal control systems for the main drives roll rate, position of pressure screws, positions of loop holders and of individual rolling stands at the lower level, and to synthesize optimal controllers at the upper level automatic control systems by thickness, tension, and loop of rolling strip.

Mathematical models of electric drives. At the beginning let us consider the mathematical models of

electric drives which is need to synthesize of control systems by the position of pressure screws, positions of loop holders and rate of the main drives for individual rolling stands.

All the main electric drives of newly built rolling mills are AC electric drives. Upgrading of existing main drive lines due to limited production space, existing DC motors replaced by AC motors. These motors have a greater degree of load, higher dynamics due to a decrease in the moment of inertia of the rotor and almost twice as much output power with the same requirements for the size of the installation site. In addition, synchronous motors have higher efficiency, a large available field weakening zone and high accuracy of torque maintenance.

Each individual main drive has its own setting action supplied through the regulator to the input of the frequency converter [15].

In the vector control by synchronous drives in most control systems, an algorithm for direct control of the motor torque is implemented [16]. Moreover, according to the majority of manufacturers of frequency converters, the rise time of the moment does not exceed 2 ms. The decay time of the moment with such a control algorithm is generally practically taken to be zero. Therefore, we will assume that the system uses frequency control of drive motors, implements hardware-software direct torque control, and we will take mathematical models of direct torque control loops in the form of proportional links.

Let us consider the mathematical models of individual main drives in the form of two-mass and three-mass electromechanical systems [16]. The mathematical model of the main electric drive, the motor is located closer to the rolling stand, takes into account two concentrated moments of inertia of the motor rotor and the rolling roll connected by an elastic shaft.

The equations of such main electric drive can written as follows

$$J_R \frac{d\omega_R}{dt} = M_E + \beta_E(\omega_M - \omega_R) - M_P;$$
$$\frac{dM_E}{dt} = C_E(\omega_M - \omega_R); \quad (1)$$
$$J_M \frac{d\omega_M}{dt} = M_M - M_E - \beta_E(\omega_M - \omega_R),$$

where ω_R, ω_M – rotation rate of the roll and the motor; J_R, J_M – moment of inertia of the roll and motor; M_E – elasticity moment; M_P – rolling moment; C_E, β_E – stiffness and internal viscous friction coefficient of the elastic shaft on twisting.

The mathematical model of the main drive, the motor of which is located further from the rolling stand, takes into account three concentrated moments of inertia - the rotor of the motor, the coupling and the rolling roll connected by elastic shafts.

The equations of such main electric drive can written as follows

$$J_R \frac{d\omega_R}{dt} = M_{E2} + \beta_{E2}(\omega_C - \omega_R) - M_P;$$

$$\frac{dM_{E2}}{dt} = C_{E2}(\omega_C - \omega_R),$$

$$J_C \frac{d\omega_C}{dt} = M_{E1} + \beta_{E1}(\omega_M - \omega_C) - M_{E2} - \ldots$$
$$\ldots - \beta_{E2}(\omega_C - \omega_R)$$

$$\frac{dM_{E1}}{dt} = C_{E1}(\omega_M - \omega_C),$$

$$J_M \frac{d\omega_M}{dt} = M_M - M_{E1} - \beta_{E1}(\omega_M - \omega_C),$$

where ω_R, ω_C, ω_M and J_R, J_C, J_M – are the rotation rate and moments of inertia of the roll, coupling and motor; M_{E1}, M_{E2} – are elasticity moments in high-rate and low-rate shafts; C_{E1}, C_{E2} and β_{E1}, β_{E2} – are stiffness and internal viscous friction coefficient of the elastic high-rate and low-rate shafts on twisting.

For hot rolling mills, the mathematical model of the electric drives of looper positions usually are adopted two-mass electromechanical systems form.

The equations of such main electric drive can written as follows

$$J_L \frac{d\omega_L}{dt} = M_{EL} + \beta_{EL}(\omega_{ML} - \omega_L) - M_L;$$

$$\frac{dM_{EL}}{dt} = C_{EL}(\omega_{ML} - \omega_L), \qquad (2)$$

$$J_{ML} \frac{d\omega_{ML}}{dt} = M_{ML} - M_{EL} - \beta_{EL}(\omega_{ML} - \omega_L),$$

where ω_L, ω_{ML} – rotation rate of the looper and the motor; J_L, J_{ML} – moment of inertia of the looper and looper motor; M_{EL} – elasticity moment; M_L – looper moment; C_{EL}, β_{EL} – stiffness and internal viscous friction coefficient of the elastic shaft on twisting for looper.

However, the feature of work of electric drives of looper positions is the nonlinear (sinusoidal) dependence of the looper load moment on the looper table angular position, that makes such electromechanical systems a substantially non-linear plant [4, 5].

The mathematical model of the electric drives of pressure screws usually are adopted in the form of single-mass electromechanical systems.

$$J_{PS} \frac{d\omega_{PS}}{dt} = M_{MPS} - M_{PPS} - M_{FPS}\text{sign}(\omega_{PS}), \quad (3)$$

where ω_{PS} – rotation rate of the pressure screws; J_{PS} – moment of inertia of the pressure screws; M_{MPS} – moment of the pressure screws motor; M_{PPS} – load moment to the pressure screws by rolling pressure; M_{FPS} – dry friction moment on the pressure screws.

Moreover, the dry friction moment on the shaft of the compression screws makes up a significant part of the moment of motor breakdown, which makes it necessary to consider such electromechanical systems as a substantially nonlinear plant [4, 5].

Mathematical model of rolling mills multi-motor electric drives.

Consider now the mathematical model of rolling mills as plant by multi-motor electric drives. For the design of local subsystems for automatic control of the thickness, tension and loop of the strip, a mathematical model of the rolling mill as a plant is required. Let us first consider the basic equations relating the energy-power parameters of one rolling stand. The quantitative increment of the final thickness Δh_1, the total rolling force ΔP and the rolling moment ΔM, as well as the increment of the rolling metal lead value ΔS, are as follows [1]:

$$\Delta h_1 = \frac{\partial h_1}{\partial h_0}\Delta h_0 + \frac{\partial h_1}{\partial T_0}\Delta T_0 + \frac{\partial h_1}{\partial T_1}\Delta T_1 + \frac{\partial h_1}{\partial z_0}\Delta z_0 + \ldots$$
$$\ldots + \frac{\partial h_1}{\partial \sigma_T}\Delta \sigma_T + \frac{\partial h_1}{\partial f}\Delta f; \qquad (4)$$

$$\Delta P = \frac{\partial P}{\partial h_0}\Delta h_0 + \frac{\partial P}{\partial h_1}\Delta h_1 + \frac{\partial P}{\partial T_0}\Delta T_0 + \ldots$$
$$\ldots + \frac{\partial P}{\partial T_1}\Delta T_1 + \frac{\partial P}{\partial \sigma_T}\Delta \sigma_T + \frac{\partial P}{\partial f}\Delta f; \qquad (5)$$

$$\Delta M = \frac{\partial M}{\partial h_0}\Delta h_0 + \frac{\partial M}{\partial h_1}\Delta h_1 + \frac{\partial M}{\partial T_0}\Delta T_0 + \frac{\partial M}{\partial T_1}\Delta T_1 + \ldots$$
$$\ldots + \frac{\partial M}{\partial \sigma_T}\Delta \sigma_T + \frac{\partial M}{\partial f}\Delta f; \qquad (6)$$

$$\Delta S = \frac{\partial S}{\partial h_0}\Delta h_0 + \frac{\partial S}{\partial h_1}\Delta h_1 + \frac{\partial S}{\partial T_0}\Delta T_0 + \frac{\partial S}{\partial T_1}\Delta T_1 + \ldots$$
$$\ldots + \frac{\partial S}{\partial \sigma_T}\Delta \sigma_T + \frac{\partial S}{\partial f}\Delta f, \qquad (7)$$

where Δh_0, ΔT_0, ΔT_1, Δz_0, $\Delta \sigma_T$, Δf are the absolute increments, respectively, of the initial thickness, the rear and front tension of the strip, the roll gap, mechanical properties, rolled metal and the value of the external friction coefficient in the deformation zone.

Based on these equations, we consider a mathematical model of a multi-stand rolling mill consisting of k stands located at a distance L_i from each other and interacting through an elastically strained strip following [1].

We introduce the vectors of the input $\boldsymbol{H_i^*}$ and output $\boldsymbol{H_i}$ thicknesses, the input $\boldsymbol{T_i^*}$ and output $\boldsymbol{T_i}$ tension and the position $\boldsymbol{B_i}$ of the pressure devices, the components of which are the corresponding values for each stand $J = \overline{1,n}$, for the linearized model and small deviations of the values from their nominal values, we obtain the following relation

$$\boldsymbol{H} = \boldsymbol{HH} \otimes \boldsymbol{H}^* + \boldsymbol{HT}^* \otimes \boldsymbol{T}^* + \boldsymbol{HT} \otimes \boldsymbol{T} + \ldots$$
$$\ldots + \boldsymbol{HB} \otimes (\boldsymbol{B} + \boldsymbol{\eta} \sin \omega t), \qquad (8)$$

where $\boldsymbol{HH}$, $\boldsymbol{HT}^*$, $\boldsymbol{HT}$, $\boldsymbol{HB}$ are the vectors of the corresponding transmission coefficients; $\boldsymbol{\eta}$ – vector of eccentricities of rolls; $\otimes$ – Kronecker (element-wise) multiplication of vectors. The time index hereinafter, where it is not needed, is omitted.

Similar relations can be obtained for the moment vectors of the main drives and the advance of the strip speed:

$$\boldsymbol{M} = \boldsymbol{MH}^* \otimes \boldsymbol{H}^* + \boldsymbol{MH} \otimes \boldsymbol{H} + \ldots$$
$$\ldots + \boldsymbol{MT}^* \otimes \boldsymbol{T}^* - \boldsymbol{MT} \otimes \boldsymbol{T}; \qquad (9)$$

$$\boldsymbol{S} = \boldsymbol{SH}^* \otimes \boldsymbol{H}^* + \boldsymbol{SH} \otimes \boldsymbol{H} + \ldots$$
$$\ldots + \boldsymbol{ST}^* \otimes \boldsymbol{T}^* + \boldsymbol{ST} \otimes \boldsymbol{T}, \qquad (10)$$

where the vectors of transmission coefficients with respect to the moment $\boldsymbol{MH}^{*}$, $\boldsymbol{MH}$, $\boldsymbol{MT}^{*}$, $\boldsymbol{MT}$ and leading $\boldsymbol{SH}^{*}$, $\boldsymbol{SH}$, $\boldsymbol{ST}^{*}$ according to the corresponding variables are determined by the technique described in [1].

The strip output speed vector is determined by the relation

$$\boldsymbol{v} = \boldsymbol{v\omega} \otimes \boldsymbol{\omega} + \boldsymbol{vS} \otimes \boldsymbol{S}, \qquad (11)$$

where $\boldsymbol{\omega}$, $\boldsymbol{v\omega}$ – are the vectors of speed of rotation of the drive rolls and the circumference of the rolls barrel; $\boldsymbol{vS}$ – the vector of transmission coefficients of the change in the strip output speed when changing the lead $\boldsymbol{S}$.

From the second volume constancy equation during rolling

$$\boldsymbol{v}^{*} \otimes \boldsymbol{H}^{*} = \boldsymbol{v} \otimes \boldsymbol{H}, \qquad (12)$$

the input velocity vector $\boldsymbol{v}^{*}$ can be determined. Neglecting the mass of the strip and assuming the instantaneous propagation of stresses along the length of the strip, we obtain

$$\boldsymbol{T}(j) = \boldsymbol{T}^{*}(j+1) \text{ for } j = \overline{1,(n-1)}, \qquad (13)$$

where $\boldsymbol{T}^{*}(j)$ is the tension on the strip unwinder.

Strip winding tension

$$\boldsymbol{T}(j) = \boldsymbol{TL}(j)\left[\boldsymbol{v}^{*}(j+1) - \boldsymbol{v}(j)\right]\Delta t; \qquad (14)$$
$$j = \overline{1,(n-1)},$$

where $\boldsymbol{TL}$ is the vector of specific stiffness of the strip in tension in the inter-cleft gap between the j-th and $(j+1)$-th stands, having a $(n-1)$ dimension.

The thickness $\boldsymbol{H}^{*}(j+1)$ of the strip at the entrance of the $(j+1)$ stand is equal to the thickness $\boldsymbol{H}(j)$ of the strip at the exit of the j-th stand, taking into account the time of transport delay

$$\boldsymbol{H}_i^{*}(j+1) = \boldsymbol{H}_{i-k}(j) \text{ and } j = \overline{1,(n-1)},$$

where $k = \text{int}(L_{j,\,(j+1)} / L_{bj})$ – is the integer part of the number equal to the deviation of the length of the inter-cleft gap $L_{j,\,(j+1)}$ between the j-th and $(j+1)$-th stands from the base length L_{bj} of the strip in this gap.

Mathematical models of the main electric drives, winder drives, loop holder drives, push-button electric drives are described in the form of a state space in the form of corresponding state equations.

Method of synthesis. We form the structure of a multi-connected system for automatically controlling by thickness, tension and loop of the strip based on typical schemes for a broadband mill. We introduce the vector $\boldsymbol{X}$ of the desired parameters, the components of which are the gain of the regulators (P, PI, PID, etc.).

We also introduce the vector $\boldsymbol{\Delta}$ of uncertainties of the system characterizing the real deviation of the system parameters from their calculated values. Note, then the transmission coefficients in the (1-4) expressions change most strongly during the rolling process for different rolling passes and when the rolled strip assortment changing.

Changes in strip thickness and tension are random processes. The main purpose of the system for regulating the thickness, tension and loops of a broadband hot rolling mill is to maintain the set values of the strip thickness behind the rolling stands, inter-stand tension and also the rotation angles of the loop holders at given levels.

Then the problem of structural-parametric synthesis of robust control by rolling mills multi-motor electric drives with parametric uncertainty can formulated in the multi-criteria game form [12] with payoff vector

$$\boldsymbol{J}(X,\Delta) = \begin{bmatrix} \Delta\boldsymbol{H}(X,\Delta)_1^2, \Delta\boldsymbol{H}(X,\Delta)_2^2,\ldots \\ \ldots, \Delta\boldsymbol{H}(X,\Delta)_N^2, \Delta\boldsymbol{T}(X,\Delta)_1^2,\ldots \\ \ldots, \Delta\boldsymbol{T}(X,\Delta)_2^2, \Delta\boldsymbol{T}(X,\Delta)_{N-1}^2 \end{bmatrix}^T. \qquad (15)$$

The components of the payoff vector are the dispersions of thicknesses $\Delta\boldsymbol{H}_i^2$ and dispersions of fluctuations in interstand tension $\Delta\boldsymbol{T}_i^2$ relative to their given values, and the deviations of the strip thickness at the exit of the i-th stand from the given value.

In the multi-criteria game (15) the first player is the vector $\boldsymbol{X}$ of the desired regulators parameters, and its strategy is the minimization of the vector gain, and the second player is a parametric external influences vectors Δ and the strategy of this player is maximization of the same vector gain [6], [7] and [12].

To find the decision of the multi-criterion games (15) from Pareto-optimal decisions [19] taking into account the preference relations [20], we used special nonlinear algorithms of stochastic multi-agent optimization.

The synthesized system parameters are determined from the multi-criteria game solution. The synthesized system structure is formed by nonzero elements from the initial excessively specified structure.

Computer simulation results. For the structural-parametric synthesis of robust control and for research of the rolling strip thickness and tension accuracy the mathematical model of multi- stands rolling mills as plant by multi-motor electric drives and the mathematical models of external influences are required. In addition, the external influences mathematical models are needed to calculate the performance and required power of electric drives, and to formulate requirements for the measuring devices accuracy.

As an example in Fig. 1 are shown experimental oscillograms of the rolling process variables on the three-stands cold rolling mill (STAN–740) with systems for controlling the thickness and tension of the strip is off. In Fig. 1 are shown: T_{12}, T_{23} – strip tension in the inter-stand spaces between the first and second stands and between the second and third stands; H_2 is the rolling pressure in the second stand; S_3 – deviation of the strip thickness behind the third stand. From these oscillograms, the mathematical model of external disturbances is constructed.
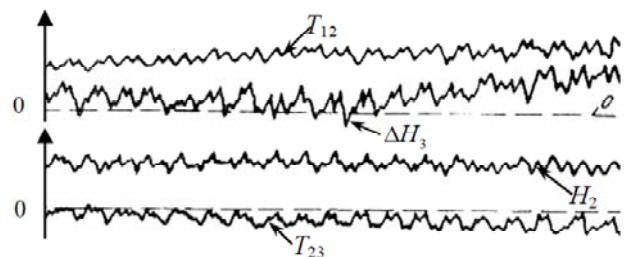

Fig. 1. Experimental oscillograms of variables of the rolling process on three-stands cold rolling mill (STAN-740)

The developed set of programs based on MATLAB was used in the synthesis of a system for automatically controlling the strip thickness and tension of a three-stand mill, on which comprehensive studies were conducted to identify the model of the mill as a control object. As an example in Fig. 2 are shown the implementation of random changes in longitudinal thickness variation and inter-stand tension in the synthesized system for three stands of the cold rolling mill (STAN–740) for the conditions of rolling steel 65G width 600 mm from thickness $H_1^* = 2$ mm to $H_3 = 1.55$ mm.
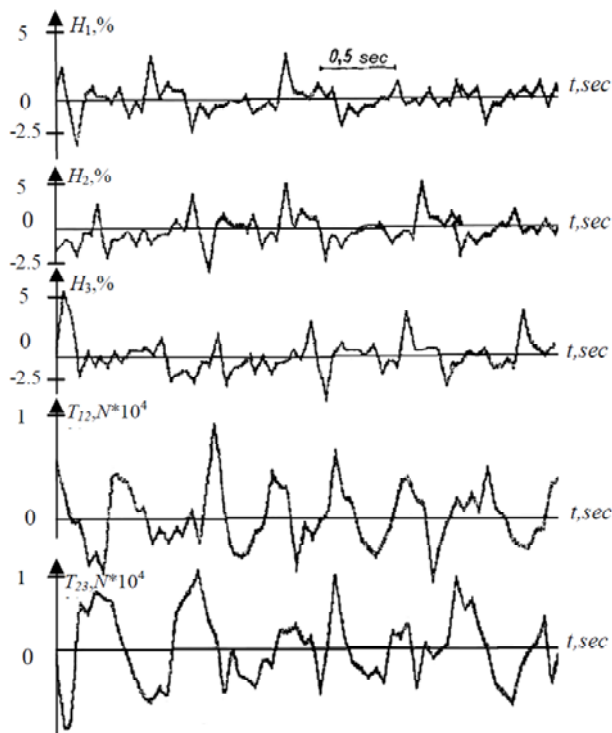

Fig. 2. Realization of random changes in longitudinal thickness variation and inter-stand tension in a synthesized system for three stands cold rolling mill (STAN-740)

The greatest decrease in the longitudinal thickness difference of the rolled strip occurred in the first stand due to the strip tension regulation between the first and second stands. However, the longitudinal thickness differences behind the second and third stands are almost the same. This, apparently, is due to an increase in the rolled strip rigidity in the second and third stands due to the strip hardening during its rolling in the first stand. As can be seen from Fig. 2, random processes of adjustable coordinates in the synthesized system satisfy the technical requirements for the system for automatically controlling the strip thickness and tension.

Numerous computer simulations of the strip thickness and tension for synthesized systems for various rolling conditions in cold and hot rolling mills were carried out.

Based on this results are shown, that the use of synthesized robust regulators made it possible to reduce the dispersions of longitudinal thickness and tension of the rolled strip in the inter-stand spaces more than 1.7-2.5 times in comparison with the existing system with typical regulator.

During the rolling process, the transmission coefficients in the (1–4) expressions change most strongly. These coefficients change most strongly for different rolling passes and when the rolled strip assortment changing. So the numerous computer simulations of the strip thickness and tension for synthesized systems for various transmission coefficients in the (1–4) expressions in cold and hot rolling mills were carried out. Based on this results are shown, that the use of synthesized robust regulators made it possible to reduce the system sensitivity to plant parameters changes on 20 % in comparison with the existing system with typical regulator.

Conclusions.

1. For the first time the method of structural-parametric synthesis of robust control by rolling mills multi-motor electric drives with parametric uncertainty based on multi-criteria game decision and particles multiswarm optimization algorithms which improves the control accuracy by rolling strip thickness and tension and reducing of sensitivity to changes of plant parameters is developed.

2. The method based on multi criterion game decision in which the vector payoff components are dispersions of longitudinal thickness and tension of the rolled strip in the inter-stand spaces. Vector payoff components calculated by modeling of the synthesized nonlinear system with different input signals, for various values of the plant parameters and for various system operation modes.

3. Based on the results of computer simulation of strip thickness and tension with the synthesized system of automatically controlling by the 740 three-stand cold rolling mill are shown, that the use of synthesized robust regulators made it possible to reduce the dispersions of longitudinal thickness and tension of the rolled strip in the inter-stand spaces more than 1.7 times, reduce on 20 % the system sensitivity to plant parameters changes in comparison with the existing system with typical regulator.

REFERENCES
1. Cuzzola F.A., Parisini T. Automation and Control Solutions for Flat Strip Metal Processing. *The Control Handbook. Second Edition*, 2010, pp. 18-36. **doi: 10.1201/b10382-22**.
2. Kozhevnikov A., Kozhevnikova I., Bolobanova N., Smirnov A. Chatter prevention in stands of continuous cold rolling mills. *Metalurgija*, 2020, vol. 59, no. 1, pp. 55-58. Available at: https://hrcak.srce.hr/224759 [accessed 06 October 2020].
3. Šinik V., Despotović Ž., Prvulović S., Desnica E. Higher harmonics of current caused by the operation of rolling mill. *IX International Conference Industrial Engineering and Environmental Protection 2019 (IIZS 2019)*, 3-4 October 2019, Zrenjanin, Serbia, pp. 50-57.
4. Krot P.V., Korennoy V.V. Nonlinear Effects in Rolling Mills Dynamics. *Proceedings of the 5th International Conference on Nonlinear Dynamics ND-KhPI2016*, September 27-30, 2016, Kharkov, Ukraine.
5. Kugi A., Schlacher K., Novak R. Nonlinear control in rolling mills: a new perspective. *IEEE Transactions on Industry Applications*, 2001, vol. 37, no. 5, pp. 1394-1402. **doi: 10.1109/28.952515.**
6. Sushchenko O.A. Robust control of angular motion of platform with payload based on H∞-synthesis. *Journal of*

Automation and Information Sciences, 2016, vol. 48, no. 12, pp. 13-26. **doi: 10.1615/jautomatinfscien.v48.i12.20**.

7. Sushchenko O.A., Tunik A.A. Robust optimization of the inertially stabilized platforms. *2012 2nd International Conference «Methods and Systems of Navigation and Motion Control» (MSNMC)*, 2012. pp. 101-105. **doi: 10.1109/msnmc.2012.6475102**.

8. Mituhiko Araki, Hidefumi Taguchi. Two-Degree-of-Freedom PID Controllers. *International Journal of Control, Automation, and Systems*, 2003, vol. 1, no. 4, pp. 401-411.

9. Zhang R., Alleyne A.G. Dynamic emulation using an indirect control input. *Journal of Dynamic Systems, Measurement, and Control*, 2004, vol. 127, no. 1, pp. 114-124. **doi: 10.1115/1.1876496**.

10. Zhiteckii L.S., Solovchuk K.Y. Robust Adaptive pseudoinverse model-based control of an uncertain SIMO memoryless system with bounded disturbances. *2019 IEEE 2nd Ukraine Conference on Electrical and Computer Engineering (UKRCON)*, Jul. 2019, pp. 621-627. **doi: 10.1109/ukrcon.2019.8879824**.

11. Zhiteckii L.S., Azarskov V.N., Solovchuk K.Y., Sushchenko O.A. Discrete-Time Robust Steady-State Control of Nonlinear Multivariable Systems: A Unified Approach. *IFAC Proceedings Volumes*, 2014, vol. 47, no. 3, pp. 8140-8145. **doi: 10.3182/20140824-6-za-1003.01985**.

12. Sushchenko O.A. Robust Control of Platforms with Instrumentation. *2019 IEEE 2nd Ukraine Conference on Electrical and Computer Engineering (UKRCON)*, Jul. 2019. pp. 518-521. **doi: 10.1109/ukrcon.2019.8879969**.

13. Shchur I., Klymko V. Comparison of different types of electromechanical systems for creating the counter-rotating VAWT. *2017 IEEE First Ukraine Conference on Electrical and Computer Engineering (UKRCON)*, May 2017. pp. 373-378. **doi: 10.1109/ukrcon.2017.8100513**.

14. Shchur I. Impact of nonsinusoidalness on Efficiency of alternative electricity generation systems. *2010 International School on Nonsinusoidal Currents and Compensation*. Lagow, 2010, pp. 218-223. **doi: 10.1109/ISNCC.2010.5524483**.

15. Ostroverkhov M., Pyzhov V., Korol S. Control of the electric drive under conditions of parametric uncertainty and coordinates' interrelation. *2017 International Conference on Modern Electrical and Energy Systems (MEES)*, Kremenchuk, 2017, pp. 64-67. **doi: 10.1109/MEES.2017.8248953**.

16. Peresada S., Kovbasa S., Korol S., Zhelinskyi N. Feedback linearizing field-oriented control of induction generator: theory and experiments. *Technical Electrodynamics*, 2017, no. 2, pp. 48-56. **doi: 10.15407/techned2017.02.048**.

17. Tytiuk V., Pozigun O., Chornyi O., Berdai A. Identification of the active resistances of the stator of an induction motor with stator windings dissymmetry. *2017 International Conference on Modern Electrical and Energy Systems (MEES)*, Nov. 2017. pp. 48-51. **doi: 10.1109/mees.2017.8248949**.

18. Zagirnyak M., Chornyi O., Nykyforov V., Sakun O., Panchenko K. Experimental research of electromechanical and biological systems compatibility. *Przegląd Elektrotechniczny*, 2016, vol.1, no.1, pp. 130-133. **doi: 10.15199/48.2016.01.31**.

19. Galchenko V.Ya., Yakimov A.N. A turmitobionic method for the solution of magnetic defectometry problems in structural-parametric optimization formulation. *Russian Journal of Nondestructive Testing*, 2014, vol. 50, no. 2, pp. 59-71. **doi: 10.1134/s106183091402003x**.

20. Gal'chenko V.Y., Yakimov A.N., Ostapushchenko D.L. Pareto-optimal parametric synthesis of axisymmetric magnetic systems with allowance for nonlinear properties of the ferromagnet. *Technical Physics*, 2012, vol. 57, no. 7, pp. 893-899. **doi: 10.1134/s1063784212070110**.

B.I. Kuznetsov[1], *Doctor of Technical Science, Professor,*
T.B. Nikitina[2], *Doctor of Technical Science, Professor,*
I.V. Bovdui[1], *Candidate of Technical Science,*
[1] State Institution «Institute of Technical Problems
of Magnetism of the NAS of Ukraine»,
19, Industrialna Str., Kharkiv, 61106, Ukraine,
phone +380 50 5766900,
e-mail: kuznetsov.boris.i@gmail.com
[2] Kharkov National Automobile and Highway University,
25, Yaroslava Mudroho Str., Kharkov, 61002, Ukraine,
e-mail: tatjana55555@gmail.com

O.F. Bondarenko, Yu.V. Kozhushko, T.O. Karbivska, Y.O. Zheliazkov, P.S. Safronov

STABILITY ANALYSIS OF HYBRID ENERGY STORAGE BASED ON SUPERCAPACITOR AND BATTERY

The aim of the work is to analyze the stability of the battery-supercapacitor hybrid storage of power supply for resistance micro-welding equipment, considering the possible variation of the system parameters and taking into account parallel series resistance of the circuit components. Methodology. The sufficient accurate mathematical model of the hybrid energy storage system to stability analysis has been obtained by the state-space average method. According to the state-space averaging method, PWM switching converters are described by separate circuit topologies for each switching period. The system of differential equations for each time interval has been derived by use of the Kirchhoff rules. The small-signal model transfer function of the SEPIC converter has been obtained by applying the Laplace transform to linear state equations averaged over one switching cycle. Finally, the Nyquist stability criterion has been considered to evaluate the stability of the proposed energy storage system. Results. Bode diagrams of an open-loop system for different values of the duty cycle, average load current, and input voltage have been obtained by using MATLAB software. The gain margin ranges from 14.6 dB to 26.4 dB and the phase margin ranges from 45.4 degrees to 54.8 degrees. From these results, it is obvious that the proposed system meets the stability criteria regardless of the aforementioned parameter fluctuations. Originality. The high-efficiency energy storage system for micro resistance welding technology has been proposed. Developing of the energy storage system according to the battery semi-active hybrid topology enables to control the Li-ion battery discharge current within the maximum allowable value. SEPIC converter utilization ensures the high-efficient operation of the power supply despite the battery charge state. Moreover, this topology allows implementing series and parallel configuration of both batteries and supercapacitors to obtain the required value of voltage and current. Practical significance. The mathematical model of the SEPIC converter has been developed by applying the state-space averaging technique. The stability analysis for parameter variation, such as duty cycle and the average load current, the input voltage has been performed by using Nyquist criteria. References 10, tables 1, figures 8.
Key words: **hybrid energy storage, SEPIC converter, stability analysis, state-space average method, micro resistance welding.**

В роботі розглянуто комбінований ємнісний накопичувач енергії на основі акумуляторної батареї (АБ) та суперконденсатора джерела живлення для установки контактного мікрозварювання. Для забезпечення рівномірного споживання струму від АБ обрано напівактивну топологію АБ та перетворювач SEPIC (Single-Ended Primary-Inductor Converter). Методом усереднення в просторі змінних стану аналітично отримано математичну модель системи. З метою проведення аналізу стійкості комбінованого накопичувача при різних значеннях коефіцієнта заповнення імпульсів, струму навантаження та напруги АБ отримано передавальну характеристику системи керування. Результати аналізу показали, що запропонована система є стійкою при зміні параметрів у встановлених межах. Бібл. 10, табл. 1, рис. 8.
Ключові слова: **комбінований ємнісний накопичувач енергії, SEPIC перетворювач, метод усереднення в просторі змінних стану, аналіз стійкості, контактне мікрозварювання.**

В работе рассмотрен комбинированный емкостный накопитель энергии на основе аккумуляторной батареи (АБ) и суперконденсатора источника питания для установки контактной микросварки. Для обеспечения равномерного потребления тока от АБ были выбраны полуактивная топология АБ и преобразователь SEPIC (Single-Ended Primary-Inductor Converter). Методом усреднения в пространстве переменных состояния аналитически получена математическая модель системы. С целью проведения анализа устойчивости комбинированного накопителя при различных значениях коэффициента заполнения импульсов, тока нагрузки и напряжения АБ получена передаточная характеристика системы управления. Результаты анализа показали, что предложенная система является устойчивой при изменении параметров в установленных пределах. Библ. 10, табл. 1, рис. 8.
Ключевые слова: **комбинированный емкостный накопитель энергии, SEPIC преобразователь, метод усреднения в пространстве переменных состояния, анализ устойчивости, контактная микросварка.**

Introduction. The vast majority of portable electronic devices have a complex nonlinear nature of power consumption. Power supplies for such devices must provide average and peak load powers, provide acceptable weight and size and high energy efficiency [1]. It is common to use different types of batteries as accumulators for portable systems. However, a significant peak load current that exceeds the average battery current can significantly reduce their service life. The use of combinations of batteries and supercapacitors can be an effective solution to such problems [1].

Depending on the configuration of storages and load, there are three main topologies of hybrid energy storage systems: passive, semi-active and active topologies [2]. Each of them is widely used in the field of

electric transport, Microgrid technology, renewable energy systems [1-3]. Also, the use of combined capacitive storages is a promising area in the field of resistance micro-welding [4].

Resistance micro-welding is an effective technology for obtaining integral joints which is widely used in the modern process of manufacturing electronic equipment. Welding technology is realized by heating the parts due to the flow of electric current of large amplitude through the place of their contact. The current amplitude usually varies from hundreds to thousands of amperes and depends on the shape and material of the welded parts [5].

The power consumption of welding machines has a specific character, namely the consumption of significant power by short pulses compared to the pauses between

them. These features of energy consumption can be the cause of the negative impact of welding machines on the industrial network. To counteract this effect, the power supplies of welding machines are developed according to the topology with intermediate energy storage (Energy Storage Topology). Usually sources built on such a topology can be divided into three main functional blocks:

• Charger provides better electromagnetic compatibility with the network and regulates the energy consumption for charging the intermediate storage.

• Intermediate capacitive storage provides the required energy during the welding cycle.

• Generator of welding pulses provides high accuracy of regulation of parameters of pulses of welding current [5].

Energy for the charge of such storages is consumed from the network uniformly, almost without causing a negative impact on it [5]. Combinations of supercapacitors, batteries and electrolytic capacitors can be used as intermediate energy storage for Energy Storage Topology [4, 5].

However, regardless of the field of use, energy efficiency, sustainability as well as weight and size are key parameters in the development of systems based on combined energy storage. The presence of a large-capacity energy storage device and nonlinear load in the DC-DC converter can adversely affect the stability of its operation. The instability of the system can manifest itself in the form of bifurcations, chaotic and quasi-periodic modes of operation [6]. Therefore, minimizing the likelihood of such phenomena is a critical task to prevent power supply system failure and reducing the rate of degradation of the characteristics of batteries and supercapacitors.

In recent years, a large number of studies have focused on methods for assessing the stability of DC-DC converters [6] and, in particular, power supplies based on combinations of capacitive storages [7]. For example,

in [6] a detailed review of various methods for assessing the stability of systems based on DC-DC converters is presented, the features of application, advantages and disadvantages of these methods, as well as examples of analysis of system stability are given. Various mathematical models are also analyzed, including discrete and time-continuous models of DC-DC converters used to investigate the stability according to different criteria. Stability analysis and hierarchical control of systems based on combined capacitive energy storage devices for Microgrid are considered in [8].

Despite a number of advantages of control systems for combined capacitive storages proposed in the mentioned works [7, 8], the task of stability research needs special attention for systems used in resistance micro-welding technology as such equipment has higher reliability requirements.

Therefore, **the goal of the paper is** the stability analysis of a hybrid energy storage of power supply for a contact micro-welding machine.

Mathematical model of the combined energy storage system. The generalized block diagram of the power supply for the resistance micro-welding machine is built on a topology with intermediate energy storage and shown in Fig. 1.

The charger consumes energy from the industrial network and provides the required value and shape of the charging current. In addition, it is necessary to provide galvanic isolation between the network and the load and the correction of the power factor. High-capacity electrolytic capacitors, various types of batteries, supercapacitors and combinations of the above-mentioned storages can be used as a storage device. The pulse generator in the figure is shown in the form of two cells, but to ensure the welding current of the required shape and amplitude in the load, N cells connected in parallel to the combined storage are used. The step-down converter (BUCK is marked in Fig. 1) acts as one such a cell [4, 5].
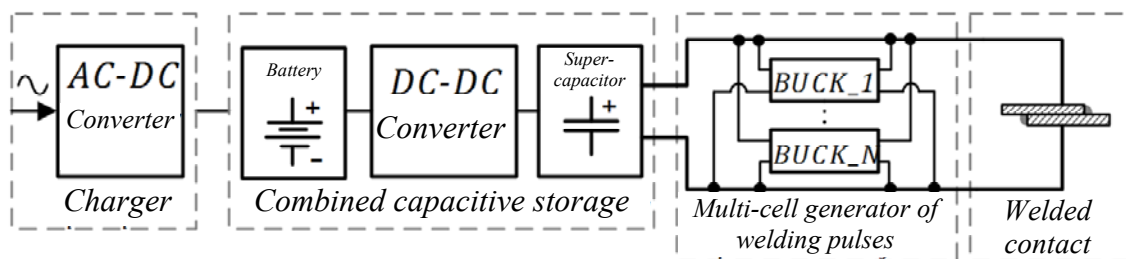

Fig. 1. Generalized block diagram of the power supply of the contact micro-welding machine

In Fig. 2 the proposed system of energy storage on the basis of semi-active topology of the battery is presented. SEPIC was chosen as a DC-DC converter to control the energy distribution between the battery and the supercapacitor. The main advantage of the semi-active battery topology is the consumption of DC from the battery with a low level of pulsations despite the fluctuations of the load current. This feature allows to significantly increase the performance of the battery in a sharp increase in load current [2]. SEPIC converter is selected as an auxiliary one because the basic requirements are met: DC current consumption from the

battery; output current regulation; wide range of output voltage regulation. Such an adjusting characteristic is necessary for Li-ion battery, because the voltage of a fully charged battery is approximately 4.2 V and gradually decreases to 2.5 V. At the same time for efficient operation of the output generator of welding pulses, powered by the supercapacitor, its input voltage must maintained at 2.7 V.
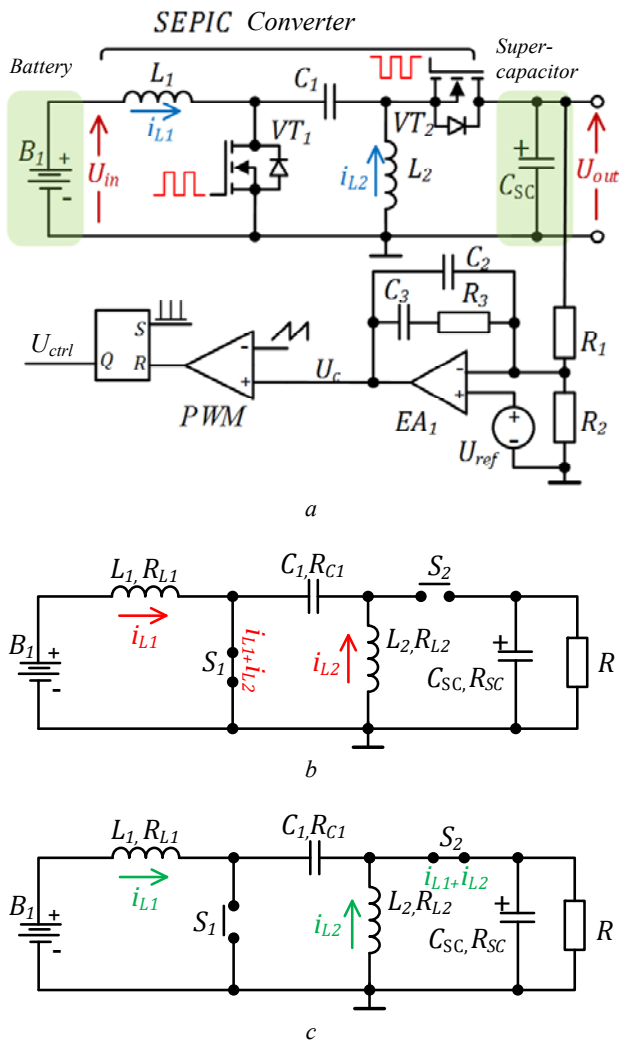
Fig. 2. Simplified circuit of combined capacitive energy storage (*a*); linearized equivalent circuit of the converter in the interval [0; *dT*] (*b*); linearized equivalent circuit of the converter on the interval [*dT*; *T*] (*c*)

The main source of static losses in low-power circuits and with a relatively large average value of the output current is the resistance of semiconductor switches in the conduction state. To increase the energy efficiency of the proposed system, the Schottky diode, which is commonly used in the SEPIC topology, is replaced by a MOSFET transistor, because the voltage drop on the open channel of such transistors (U_{Rds_on} = 0.3 mV … 0.7 V) at nominal values of switching current is simultaneously a direct voltage drop of the Schottky diode (U_F = 0.3… 1.5 V). However, it should be noted that with increasing frequency, the dynamic losses of the transistor increase due to recharging of the parasitic capacitances [5].

To obtain a sufficiently accurate for the analysis of the stability of the mathematical model the method of averaging state variables is used [9]. To simplify the analysis, the system can be represented as two separate circuits, for time intervals when the key is closed [0, *dT*] and open [*dT*; *T*]. Parameter *d* is the pulse filling factor that determines the conduction intervals of the keys of the PWM-controlled converters. For SEPIC, the minimum and maximum value of *d* depending on the input voltage

level is determined by expressions (1) and (2), respectively:

$$d_{\min} = \frac{U_{out} + U_f}{U_{in\,\max} + U_{out} + U_f}; \qquad (1)$$

$$d_{\max} = \frac{U_{out} + U_f}{U_{in\,\min} + U_{out} + U_f}, \qquad (2)$$

where U_{out} is the output voltage; U_f is the direct voltage drop on the closed key S_2; $U_{in\min}$ is the minimum value of the input voltage; $U_{in\max}$ is the maximum value of the input voltage.

The paper considers a quasi-steady state mode when the battery and the supercapacitor are charged to the nominal value. The value of the maximum frequency for analysis is selected so that the phase margin for the converter does not exceed 50°, which is within generally accepted standards. The proposed model is valid for this type of converters at frequencies up to 150 kHz, because it does not take into account the dynamic losses of semiconductor elements. MOSFET transistors *VT*1 and *VT*2 have been replaced by ideal switches S_1 and S_2, the resistance in the closed state of which is infinitely small, and in the open state it is infinitely large. Idealized diagrams of voltage and current of the converter showing the operation of the converter for the switching period are presented in Fig. 3.
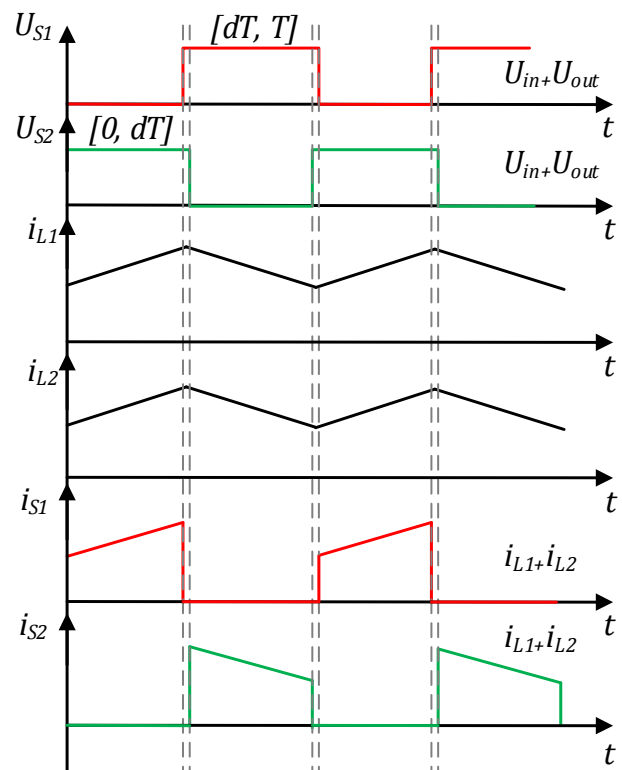

Fig. 3. SEPIC converter voltage and current idealized diagrams for the switching period

The energy for welding is consumed by short pulses with much longer pauses between them and at a certain interval can be considered as a pulse load with a period of T_w. Thus, the average current consumption for one welding cycle [0, T_w] can be defined as [2]:

$$i_{ave}(t) = \frac{1}{T_w}\int\limits_0^{T_w} i_{load}(t)dt = D_w i_{max} + (1 - D_w)i_{min} = I_{ave}, \quad (3)$$

where i_{load} is the current consumed by the generator of welding pulses; i_{max} is the amplitude of welding current; i_{min} is the the minimum value of welding current (equal to zero); D_w is the pulse filling factor, a fixed value determined by the technological features of the welding cycle.

Since the switching period of switches S_1 and S_2 is much smaller than the duration of one welding cycle T_w, the load current in the period $[0; T]$ will be constant and will be determined by the average current I_{ave} for one welding cycle.

The mathematical model is based on differential equations compiled for each linear substitution circuit. In circles with a variable structure, the systems of differential equations for linear circuits for different intervals are compiled independently of each other. Thus, the average model of the system for one switching cycle can be described by the following system of differential equations:

$$\begin{cases} X' = (dA_1 + (1-d)A_2)\cdot X + (dB_1 + (1-d)B_2)\cdot U; \\ Y = (dC_1 + (1-d)C_2)\cdot X + (dE_1 + (1-d)E_2)\cdot U, \end{cases} \quad (4)$$

where X is the vector of state variables; A_1 and A_2 are the matrices of coefficients for state variables for each linear substitution circuit; U is the vector-column of external action; B_1 and B_2 are the matrices of coefficients for the elements of external action for each linear substitution circuit; Y is the vector-column of initial values; C_1 and C_2 are the matrices of relationship of initial quantities with state variables for each linear substitution circuit; E_1 is E_2 are the matrices of the relationship between the initial quantities and the vector of external action for each linear substitution circuit.

The system of equations can be represented as the sum of the system of algebraic equations (5) for the constant component and the system of differential equations (6) for the variable component:

$$\begin{cases} X' = A^{-1}BU; \\ Y = -CA^{-1}BU + EU. \end{cases} \quad (5)$$

After applying the Laplace transform, the system of differential equations for the variable component takes the form:

$$\begin{cases} \hat{x}(s) = [C(sI - A)^{-1}B \quad C(sI - A)^{-1}B_d]\cdot \begin{bmatrix} \hat{u}(s) \\ \hat{d}(s) \end{bmatrix}; \\ \hat{y}(s) = [C(sI - A)^{-1}B + E \quad C(sI - A)^{-1}B_d + E_d]\cdot \begin{bmatrix} \hat{u}(s) \\ \hat{d}(s) \end{bmatrix}. \end{cases} \quad (6)$$

where $B_d = (A_1 - A_2)\cdot X + (B_1 - B_2)\cdot U$ and $E_d = (C_1 - C_2)\cdot X + (E_1 - E_2)\cdot U$.

The solution of the system of equations (6) gives the transfer characteristic of the converter in the small deviations mode:

$$G_{dv}(s) = C(sI - A)^{-1}B_d + E_d. \quad (7)$$

Based on the above equations, the analysis of the proposed topology is performed. The equation of state in matrix form for the operation interval $[0, dT]$ is obtained on the basis of Kirchhoff laws (8). The equation of the initial values in matrix form for the operation interval $[0, dT]$ is defined as (9). Similarly, the equation of state (10) and the equation of the initial values (11) in matrix form for the operation interval $[dT; T]$ are obtained:

$$\begin{bmatrix} i'_{L_1} \\ i'_{L_2} \\ u'_{C_1} \\ u'_{C_{SC}} \end{bmatrix} = \begin{bmatrix} -\dfrac{R_{L_1}}{L_1} & 0 & 0 & 0 \\ 0 & -\dfrac{R_{C_1}}{L_2} - \dfrac{R_{L_1}}{L_2} & \dfrac{1}{L_2} & 0 \\ 0 & -\dfrac{1}{C_1} & 0 & 0 \\ 0 & 0 & 0 & -\dfrac{1}{C_{SC}(R + R_{SC})} \end{bmatrix} \begin{bmatrix} i_{L_1} \\ i_{L_2} \\ u_{C_1} \\ u_{C_{SC}} \end{bmatrix} + \begin{bmatrix} \dfrac{1}{L_1} \\ 0 \\ 0 \\ 0 \end{bmatrix} \cdot [U_{in}], \quad (8)$$

$$U_{out} = \begin{bmatrix} 0 & 0 & 0 & \dfrac{R}{R + R_{SC}} \end{bmatrix} \cdot \begin{bmatrix} i_{L_1} & i_{L_2} & u_{C_1} & i_{SC} \end{bmatrix}^T + [0]\cdot[U_{in}], \quad (9)$$

$$\begin{bmatrix} i'_{L_1} \\ i'_{L_2} \\ u'_{C_1} \\ u'_{C_{SC}} \end{bmatrix} = \begin{bmatrix} -\dfrac{R_{C_1}}{L_1} - \dfrac{R_{L_1}}{L_1} - R_{E1} & -R_{E1} & -\dfrac{1}{L_1} & -\dfrac{R}{L_1(R + R_{SC})} \\ -R_{E2} & -\dfrac{R_{L_1}}{L_2} - R_{E2} & 0 & -\dfrac{R}{L_2(R + R_{SC})} \\ \dfrac{1}{C_1} & 0 & 0 & 0 \\ \dfrac{R}{C_{SC}(R + R_{SC})} & \dfrac{R}{C_{SC}(R + R_{SC})} & 0 & -\dfrac{1}{C_{SC}(R + R_{SC})} \end{bmatrix} \cdot \begin{bmatrix} i_{L_1} \\ i_{L_2} \\ u_{C_1} \\ u_{C_{SC}} \end{bmatrix} + \begin{bmatrix} \dfrac{1}{L_1} \\ 0 \\ 0 \\ 0 \end{bmatrix} \cdot [U_{in}], \quad (10)$$

$$R_{E1} = \frac{R \cdot R_{SC}}{L_1(R + R_{SC})} \qquad R_{E2} = \frac{R \cdot R_{SC}}{L_1(R + R_{SC})}$$

$$U_{out} = \begin{bmatrix} \dfrac{R \cdot R_{SC}}{R + R_{SC}} & \dfrac{R \cdot R_{SC}}{R + R_{SC}} & 0 & \dfrac{R}{R + R_{SC}} \end{bmatrix} \cdot \begin{bmatrix} i_{L_1} & i_{L_2} & u_{C_1} & i_{SC} \end{bmatrix}^T + [0] \cdot [U_{in}]. \qquad (11)$$

The transfer characteristic of the converter in the mode of small deviations is obtained analytically on the basis of the solution of the generalized system of differential equations for both intervals and has the form:

$$G_{dv}(s) = \frac{b_4 s^4 + b_3 s^3 + b_2 s^2 + b_1 s + b_0}{a_4 s^4 + a_3 s^3 + a_2 s^2 + a_1 s + a_0}, \qquad (12)$$

where $a_0 \ldots a_4$ are the coefficients of the denominator of the transfer characteristic; $b_0 \ldots b_4$ are coefficients of the numerator of the transfer characteristic.

Analysis of the stability of the combined energy storage system. The control system of the SEPIC converter is presented in the form of a block diagram in Fig. 4, where the main links of the control system are replaced by their transfer characteristics.
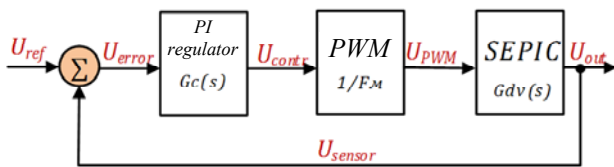

Fig. 4. Generalized structure of the SEPIC converter control system for combined capacitive energy storage

Transfer characteristic of the open system for the analysis of influence of change of parameters (filling factor, average load current and input voltage) on the stability of the system is determined as:

$$H(s) = G_C(s) \cdot F_M \cdot G_{dv}(s), \qquad (13)$$

where $G_C(s)$ is the transfer characteristic of the PI regulator, F_M is the gain of the PWM comparator, $G_{dv}(s)$ is the SEPIC transfer characteristic in small deviation mode.

The transfer characteristic $G_{dv}(s)$ of the SEPIC converter used to control the energy distribution between the elements of the combined capacitive storage device is obtained analytically on the basis of the equations presented in the previous section.

The main function of the regulator is to ensure the required control accuracy and margin for phase and amplitude in accordance with the Nyquist criterion of stability. PI (proportional-integral) regulator supplemented by a low-pass filter is selected as a regulator. This type of regulators is widely used in industry due to its simple design, low cost and simple tuning algorithm. The PI regulator eliminates forced oscillations and static error, the transfer characteristic of which is as follows [10]:

$$G_C(s) = \frac{K_C(1 + T_C s)}{T_C s(1 + T_f s)}, \qquad (14)$$

where K_C is the gain; T_C is the integration time constant; T_f is the filtration time constant.

The gain of the PWM comparator F_M is determined by the amplitude of the sawtooth signal and has the following form:

$$F_M = \frac{1}{U_M}, \qquad (15)$$

where U_M is the amplitude of sawtooth voltage.

Table 1 shows the main parameters of the SEPIC converter and PI regulator components, as well as the initial data of the combined energy storage system used for stability analysis.

Table 1

Data for stability analysis

Output parameters		Component parameters			
U_{in}, V	2.5; 3.7; 4.2	L_1, L_2, μH	10		
U_{out}, V	2.7	C_1, μF	820		
I_{out}, A	5; 10; 15	C_{SC}, F	350		
γ	0.4; 0.5; 0.6	$R_{L1}, R_{L1}, R_{C1}, R_{Csc}$, mΩ	10		
U_M, V	2.7	C_2, pF	100	R_1, R_2, kΩ	1.2
U_{ref}, V	1.35	C_3, μF	1	R_3, kΩ	15

The solution of the averaged system of differential equations and the logarithmic amplitude-phase frequency characteristics (LAPFC) of an open system under different conditions was obtained using the MATLAB software package.

Figure 5 shows the LAPFC of the open system for different values of the load current at the nominal parameters of the circuit components, the input voltage U_{in} = 3.7 V and the pulse filling factor d = 0.5. The diagrams show that the control system provides a margin for the phase from 45.4° to 54.8° and for the amplitude from 14.6 dB to 26.4 dB; when the load current changes the system remains stable.
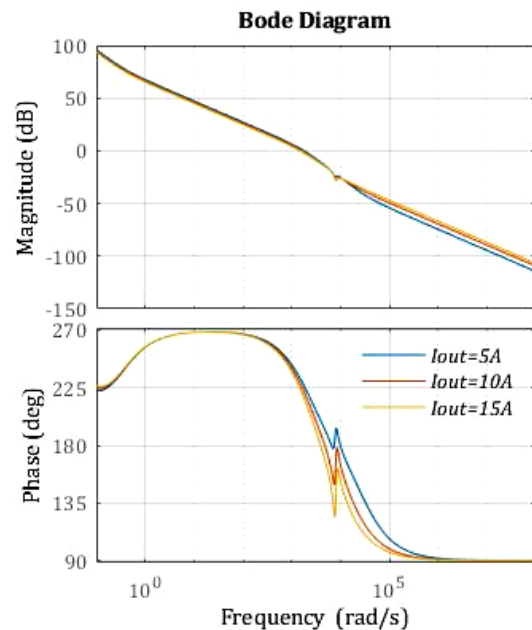

Fig. 5. LAPFC of the open system for different values of the load current

LAPFCs of the system when changing the pulse filling factor and nominal input voltage U_i = 3.7 V, current loads I_{out} = 10 A are shown in Fig. 6. The system is stable at different values of the pulse filling factor. Similarly, the stability of the system is affected by the change in input voltage at d = 0.5 and I_{out} = 10 A (Fig. 7). All other system parameters remain unchanged in all three cases.
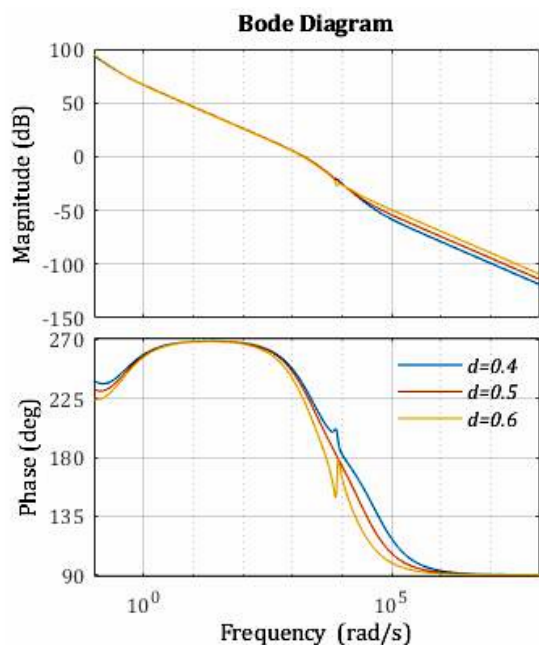
Bode Diagram

Fig. 6. LAPFC of the open system for different values of the pulse filling factor
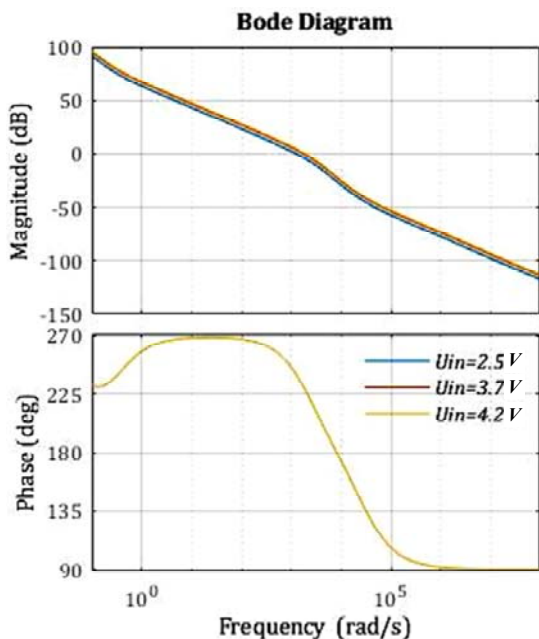
Bode Diagram

Fig. 7. LAPFC of the open system for different values of the input voltage

The reaction of the system to the influence in the form of a single step function is shown in Fig. 8. Because the system has a supercapacitor of large capacitance, the duration of the transient is in milliseconds. In order to counteract this effect, the supercapacitor can be represented as a voltage source, because the voltage on it during one switching period is almost unchanged.
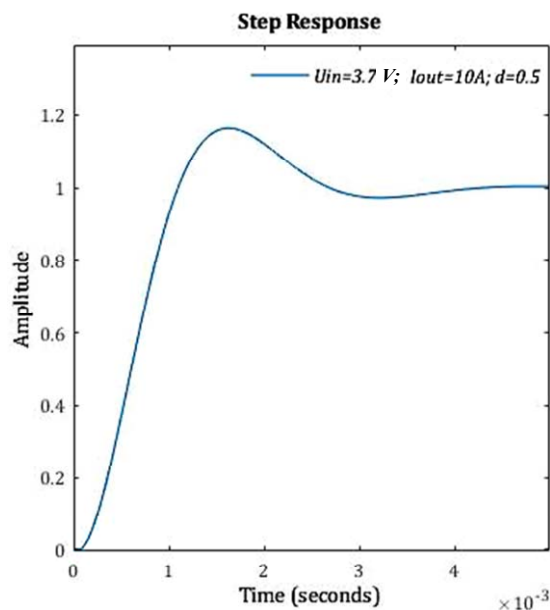
Step Response

Fig. 8. Transient function of the transfer characteristic of a closed loop

Conclusions.

An energy storage device based on a combination of a supercapacitor and a battery for a power supply developed according to the topology of intermediate energy storage used for resistance micro-welding technology is proposed. A semi-active battery topology and a SEPIC converter have been selected for energy distribution between the storages, which allows to provide the battery discharge with the rated current and rated voltage on the supercapacitor regardless of the battery charge level.

A mathematical model of the converter which takes into account the parasitic resistances of the circuit components is obtained. The Nyquist criterion is used to study the stability of the proposed control link. As a result of the analysis the area of stability of system at variation of key parameters of system is defined. The presented topology is stable when changing the pulse filling factor, load current and input voltage in a wide range.

Further work will be devoted to the practical verification of the obtained results using the physical model of the proposed combined storage.

REFERENCES
1. Khalid M. A review on the selected applications of battery-supercapacitor hybrid energy storage systems for microgrids. *Energies*, 2019, vol. 12, no. 23, p. 4559. **doi: 10.3390/en12234559.**
2. Kuperman A., Aharon I. Battery-ultracapacitor hybrids for pulsed current loads: A review. *Renewable and Sustainable Energy Reviews*, 2011, vol. 15, no. 2, pp. 981-992. **doi: 10.1016/j.rser.2010.11.010.**

3. Bocklisch T. Hybrid energy storage approach for renewable energy applications. *Journal of Energy Storage*, 2016, vol. 8, pp. 311-319. **doi: 10.1016/j.est.2016.01.004**.

4. Kozhushko Y., Pavkovic D., Zinchenko D., Karbivska T., Sydorets V., Bondarenko O. Hybrid Energy Storage System of Power Supply for Micro Resistance Welding. *2019 IEEE 39th International Conference on Electronics and Nanotechnology, ELNANO 2019 – Proceedings*, 2019, pp. 584-589, **doi: 10.1109/elnano.2019.8783890.**

5. Bondarenko O., Verbytskyi I., Prokopets V., Kaloshyn O., Spitsyn D., Ryzhakova T., Kozhushko Y. Modular Power Supply for Micro Resistance Welding. *Electrical, Control and Communication Engineering*, 2017, vol. 12, no. 1, pp. 20-26. **doi: 10.1515/ecce-2017-0003**.

6. El Aroudi A., Giaouris D., Iu H. H.-C., Hiskens I.A. A Review on Stability Analysis Methods for Switching Mode Power Converters. *IEEE Journal on Emerging and Selected Topics in Circuits and System*, 2015, vol. 5, no. 3, pp. 302-315. **doi: 10.1109/jetcas.2015.2462013**.

7. Kotra S., Mishra M.K. Design and Stability Analysis of DC Microgrid With Hybrid Energy Storage System. *IEEE Transactions on Sustainable Energy*, 2019, vol. 10, no. 3, pp. 1603-1612. **doi: 10.1109/tste.2019.2891255**.

8. Dong C., Jia H., Xu Q., Xiao J., Xu Y., Tu P., Lin P., Li X., Wang P. Time-delay stability analysis for hybrid energy storage system with hierarchical control in DC Microgrids. *IEEE Transactions on Smart Grid*, 2018, vol. 9, no. 6, pp. 6633-6645. **doi: 10.1109/tsg.2017.2717504**.

9. Rudenko Yu.V. Mode of averaging of pulse DC converter model. *Technical Electrodynamics*, 2017, no. 3, pp. 42-48. (Rus). **doi: 10.15407/techned2017.03.042.**

10. Aström K.J., Hägglund T. *PID controllers: theory, design, and tuning*, vol. 2. International Society of Automation, 1995.

O.F. Bondarenko[1]*, Candidate of Technical Science, Associate Professor,*
Yu.V. Kozhushko[1]*, Postgraduate Student,*
T.O. Karbivska[1]*, Postgraduate Student,*
Y.O. Zheliazkov[1]*, Student,*
P.S. Safronov[1]*, Candidate of Technical Science, Associate Professor,*
[1] National Technical University of Ukraine «Igor Sikorsky Kyiv Polytechnic Institute»,
37, Prospect Peremohy, Kyiv-56, 03056, Ukraine,
e-mail: bondarenkoaf@gmail.com

V.S. Grinchenko, K.V. Chunikhin

MAGNETIC FIELD NORMALIZATION IN RESIDENTIAL BUILDING LOCATED NEAR OVERHEAD LINE BY GRID SHIELD

This paper deals with the magnetic field mitigation of 110 kV trefoil single-circuit and double-circuit overhead lines by grid shields. The shields under study are made of aluminum conductors connected in parallel. These shields are mounted on the walls of the building. We study the efficiencies of plane and U-shaped grid shields as the dependence from the quantity of metal. As the result, we show that the plane grid shield does not supply the required efficiency of magnetic field mitigation in corner areas of the building. At the same time, the U-shaped grid shield having equivalent quantity of metal allows to mitigate the magnetic field to the reference level 0.5 µT in more than 97 % part of the building. References 11, figures 9, tables 4.
Key words: **magnetic field, shielding, overhead line, right-of-way, reference level.**

Досліджено можливість зменшення магнітного поля в житлових будинках, які знаходяться на границі охоронної зони одноколових повітряних ліній електропередачі із розташуванням проводів у вершинах трикутника та двололо-вих повітряних ліній електропередачі 110 кВ, поширених в міських електромережах, за допомогою запропонованих авторами гратчастих екранів. Розглянуті екрани виконано з алюмінієвих проводів, з'єднаних паралельно між собою, та встановлено на стіни будинку. Досліджено ефективності плаского та U-подібного гратчастих екранів різної ме-талоємності. Показано, що плаский гратчастий екран не забезпечує достатнього зменшення магнітного поля в ку-тових областях житлових будинків. У той же час U-подібний гратчастий екран еквівалентної металоємності до-зволяє зменшити магнітне поле до гранично допустимого рівня 0,5 мкТл в більш ніж 97 % приміщень будинку. Запро-поновано рекомендації щодо конструктивного виконання гратчастих екранів. Бібл. 11, рис. 9, табл. 4.
Ключові слова: **магнітне поле, екранування, повітряна лінія електропередачі, охоронна зона, гранично допустимий рівень.**

Исследована возможность уменьшения магнитного поля в жилых домах, которые находятся на границе охранной зоны распространенных в городских электросетях одноцепных воздушных линий электропередачи с расположением проводов в вершинах треугольника и двухцепных воздушных линий электропередачи 110 кВ, при помощи предложен-ных авторами решетчатых экранов. Рассмотренные экраны выполнены из алюминиевых проводов, соединенных па-раллельно между собой, и установлены на стены дома. Исследованы эффективности плоского и U-образного решет-чатых экранов различной металлоемкости. Показано, что плоский решетчатый экран не обеспечивает достаточно-го уменьшения магнитного поля в угловых областях жилых домов. В то же время U-образный решетчатый экран эквивалентной металлоемкости позволяет уменьшить магнитное поле до предельно допустимого уровня 0,5 мкТл в более чем 97 % помещений дома. Предложены рекомендации по конструктивному исполнению решетчатых экранов. Библ. 11, рис. 9, табл. 4.
Ключевые слова: **магнитное поле, экранирование, воздушная линия электропередачи, охранная зона, предельно допустимый уровень.**

Introduction. The 110 kV overhead lines (OHL) crossing residential areas are the main source of the power frequency magnetic field in residential buildings [1]. Long-term exposure of power frequency magnetic field (even when its level is relatively low) negatively affects on human health. This leads to a global trend of tightening of sanitary standards. In Ukraine, the reference level of power frequency magnetic field for residential areas is 0.5 µT [2]. However, this norm does not meet for most residential buildings located near OHL, in particular, on borders of their right-of-way (ROW). This is because the size of ROW, regulated in [3], does not take into account modern requirements for the reference level of power frequency magnetic field. Dismantling and transferring OHL or replacing it with an underground cable line requires significant costs. Therefore, it is advisable to mitigate the OHL magnetic field by electromagnetic shields – solid electrically conductive plates, installed on the inner or outer surface of the wall. But such solid shields cannot be used on walls with windows.

In [4, 5] the mitigation of the magnetic field, created by a single-circuit OHL with a vertical arrangement of conductors, is considered and a new type of electromagnetic shields is proposed: the so-called grid shield, consisting of a set of aluminum conductors connected in par-

allel. The main advantage of this shield is that it does not interfere the light propagation.

However, the possibility of using grid shields to mitigate the magnetic field in residential buildings, located on the ROW border of widespread 110 kV trefoil single-circuit and double-circuit OHL, creating rotating magnetic field, is not studied.

The purpose of this work is to determine the possibility of the magnetic field normalization in residential buildings, located on right-of-ways borders of typical 110 kV trefoil and double-circuit overhead lines, using grid shields and to develop recommendations for shield design.

Geometric sizes of single-circuit OHL and right-of-way. Fig. 1 shows the accepted designations for single-circuit tower sizes: a_1, a_2, a_3 are the shortest distances from the vertical axis of tower symmetry to the suspension points of conductors; h_1, h_2 are their heights. Note, that depending on climatic conditions towers with different vertical spacing between the conductors are used [2]. Also Fig. 1 shows the numbering of conductors of the single-circuit OHL, adopted in this work. We assume that OHL is symmetric and RMS values of conductors currents are equal to each other, i.e. $I_3 = I_2 = I_1$.
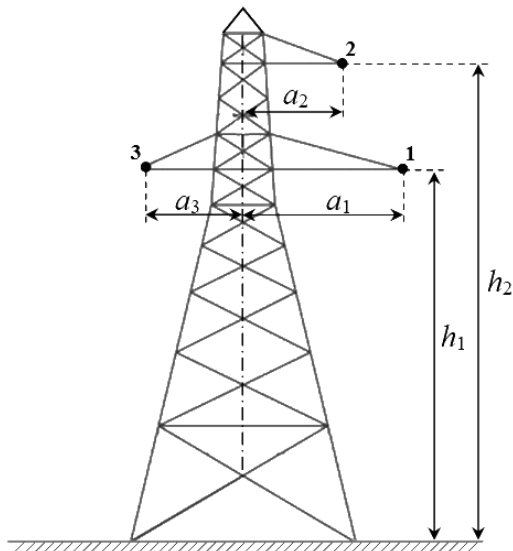
Fig. 1. Schematic representation of 110 kV
single-circuit OHL tower

Table 1 summarizes the geometric sizes of typical 110 kV single-circuit towers [6]. We see that a_1, a_2, a_3 and h_1, h_2 of P110-3V type tower are the closest to corresponding averaged values, given in Table 1. Therefore, in further magnetic field calculations for single-circuit OHL we assume, that a_1=4.2 m, h_1=19 m, a_2=2.1 m, h_2=23 m and a_3=2.1 m.

ROW is established to create normal operating conditions for electrical networks and ensure their safety, as well as to comply with security requirements. In Ukraine, the ROW size of 110 kV OHL is 20 m [3]. Therefore, in this work, the distance between the outermost conductor with number 1 and the residential building wall, located along the ROW border x=0, is taken to be 20 m (Fig. 2).

Table 1

Sizes of typical 110 kV single-circuit OHL towers

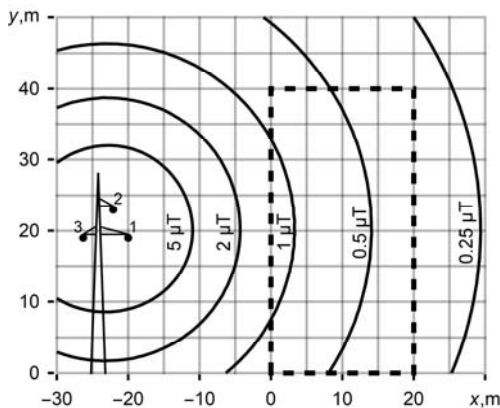| Tower type	a_1, m	a_3, m	h_1, m	a_2, m	h_2, m
P110-3V	4.2	2.1	19	2.1	23
P110-3V+4	4.2	2.1	23	2.1	27
PS110-9V	4.2	2.6	19	2.6	25
PM110-1F	4.7	2.4	19	2.4	23
PM110-3F	3.9	2.3	15	2.3	19
PB-29	2.75	2.0	13.5	2.0	17.5
Average value	4.0	2.3	18	2.3	22.4

Fig. 2. Distribution of single-circuit OHL magnetic field

Magnetic field of single-circuit OHL. In [7] it is shown that the OHL magnetic field penetrates residential buildings with almost no weakening. To calculate the OHL magnetic field we assume the following [1, 7, 8]: OHL conductors are infinitely long, parallel to each other and to the ground; the influence of towers on the OHL magnetic field distribution is neglected; the electric currents induced in the ground are neglected, assuming zero electrical conductivity of the soil.

The accepted assumptions allow obtaining an analytical expression for the magnetic field, created by OHL in free space. According to the first assumption, the magnetic field is plane-parallel. If the Cartesian coordinate system is such as shown in Fig. 2, then the RMS value of the magnetic flux density at an arbitrary point (x, y) can be found using the following expression [7]:

$$B = \left(\left| \sum_{p=1}^{3} \frac{\mu_0 I_p e^{j\varphi_p}}{2\pi} \cdot \frac{y - y_p}{(x - x_p)^2 + (y - y_p)^2} \right|^2 + \left| \sum_{p=1}^{3} \frac{\mu_0 I_p e^{j\varphi_p}}{2\pi} \cdot \frac{x - x_p}{(x - x_p)^2 + (y - y_p)^2} \right|^2 \right)^{\frac{1}{2}}, \quad (1)$$

where I_p and φ_p are the RMS value and the initial phase of the current in the p-th OHL conductor; x_p and y_p are coordinates of the p-th OHL conductor in the xOy plane; μ_0=$4\pi \cdot 10^{-7}$ H/m is a vacuum permeability; j is an imaginary unit.

The value of the OHL rated current is taken equal to I_1=500 A [1, 7, 8]. The initial phases are taken as follows: φ_1=$-2\pi/3$, φ_2=0, φ_3=$2\pi/3$. Fig. 2 shows the distribution of magnetic flux density isolines, found using (1). The dotted line marks the contour of the residential building, located near OHL. We see that the magnetic field exceeds the reference level of 0.5 μT in the left part of the residential building.

Shielding of single-circuit OHL magnetic field. We select the following parameters of the plane grid shield on the basis of [4, 5]: the number of conductors is 81, the diameter of each conductor is 8 mm, and the distance between adjacent conductors is 0.5 m. The quantity of metal of the shield is denoted by V. The shield is located in the plane x=0, i.e. on the wall of the residential building facing OHL (Fig. 3). Thus, the coordinates of axes of conductors are as follows: x_k=0, y_k=$(0.5 \cdot k)$ m, where k=0..80. The electrical conductivity of the grid shield is equal to $3.5 \cdot 10^7$ S/m.

To find the shielded magnetic field distribution, we alternately used two different approaches: the numerical simulation within the framework of the model, presented in [4, 5], and the analytical calculation within the framework of the model, proposed in [9].

The difference in the magnetic flux density of the shielded field, obtained using these models, lays within 3%. To verify the models, we considered the case of zero conductivity of the shield: the results of the magnetic field calculation at control points agree with the results of the calculation according to the technique from [10].
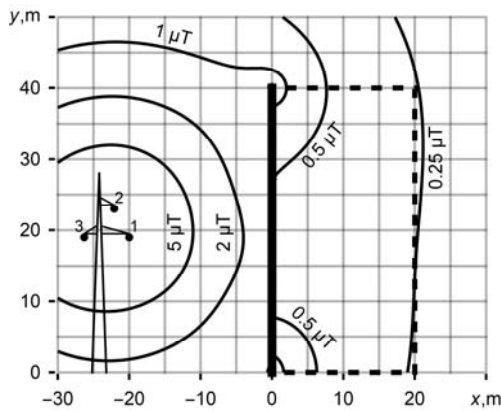
Fig. 3. Distribution of single-circuit OHL magnetic field when using plane grid shield

Fig. 4. Distribution of single-circuit OHL magnetic field when using U-shaped grid shield

Fig. 3 shows calculation results of the OHL magnetic field when the plane grid shield is used. We see that the magnetic field does not exceed the reference level of 0.5 μT in the bigger part of the residential building. However, the plane shield does not provide a sufficient magnetic field mitigation in corner areas of the building.

To increase the efficiency of shielding, we use the approach proposed in [5], where the usage of U-shaped grid shields is recommended. Consequently, we take the parameters of the U-shaped shield as follows: the number of conductors is 121, the diameter of each conductor is 6.5 mm, the distance between adjacent conductors is 0.5 m, and the length of arms is 10 m. Fig. 4 shows a U-shaped contour. The conductors are located along this contour with an equal step. The vertical section is identical to the plane grid shield. The arms of the shield (each of them consists of 20 conductors) are located on upper and lower technical floors of the residential building. Axes of conductors of arms have the following coordinates: $x_k = (0.5 \cdot k)$ m, $y_k = 0$ for the lower arm and $y_k = 40$ m for the upper arm, where $k=1..20$. The quantity of metal of the U-shaped shield under consideration is equal to V.

Fig. 4 shows calculation results of the single-circuit OHL magnetic field when the U-shaped grid shield is used. We see that the magnetic field is lower than the reference level in almost the entire residential building. The excess is observed only in the vicinity of the outer conductors of the shield.

We use the magnetic field normalization index η as a criterion for the magnetic field shielding efficiency in the residential building. This index determines the percentage of living space, where the magnetic field is normalized and does not exceed the reference level. When the magnetic field is plane-parallel, the normalization index is

$$\eta = \frac{S}{S_0} \cdot 100\% , \qquad (2)$$

where S is the total of cross-sections of residential building areas, in which the magnetic field does not exceed the reference level, and S_0 is the cross-section of the entire building. Note that according to [2] the areas closer than 0.5 m to the walls are not taken into account when finding S and S_0. Analysis of magnetic field distributions in Fig. 3 and Fig. 4 allows to determine S in each case. The area S_0 is a product of sides lengths of the shielding region.
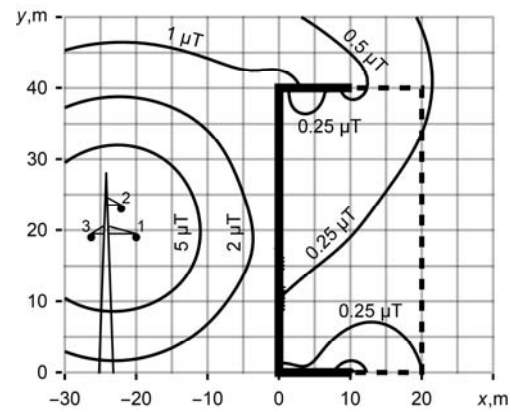
Then according to (2) the index η is 88.3% when using the plane grid shield and 99.2% when using the U-shaped grid shield.

An increase or decrease in the quantity of metal of the grid shield, achieved by changing the conductor diameter, leads to a corresponding change in the normalization index. Table 2 shows η when varying the quantity of metal of the shield from $0.2 \cdot V$ to $1.2 \cdot V$. Calculation results show that the use of the plane grid shield is ineffective for the trefoil OHL magnetic field mitigation, when the magnetic field is rotating. At the same time, the U-shaped grid shield makes it possible to achieve the normalization index η=97% at the quantity of metal of $0.5 \cdot V$. Therefore, the conductor diameter can be reduced to 4.6 mm, while maintaining number of conductors of the shield and their arrangement.

Note that relatively high values of η, given in Table 2, also follows from the fact, that in the absence of the shield the magnetic field level does not exceed the reference in the right part of the building. From the analysis of the magnetic field distribution, shown in Fig. 2, it follows that the magnetic field normalization index in the absence of the shield is 38.1%.

Geometric sizes of double-circuit OHL. There are several options for the location of double-circuit OHL conductors on the tower: «vertical arrangement», «straight firtree», «reverse firtree» and «barrel». The last one is the most widespread in Ukraine (Fig. 5).

Table 2

Magnetic field normalization index η
for residential building located near single-circuit OHL
when using grid shield

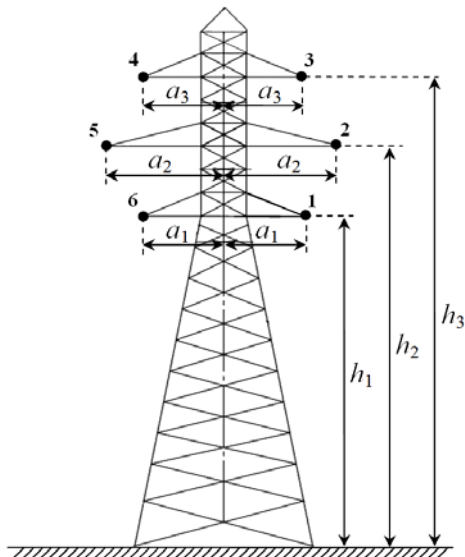| Quantity of metal of shield referred to V	η, %	
	Usage of plane shield	Usage of U-shaped shield
0.2	60.5	64.3
0.3	68.6	81.0
0.4	75.3	91.6
0.5	80.1	97.4
0.6	83.0	99.2
0.8	86.6	99.2
1.0	88.3	99.2
1.2	89.2	99.2

Fig. 5. Schematic representation of 110 kV
double-circuit OHL tower

By analogy with previous sections, we introduce the following designations for double-circuit tower sizes: a_1, a_2, a_3 are the shortest distances from the vertical axis of tower symmetry to the suspension points of conductors; h_1, h_2, h_3 are their heights. Also Fig. 5 shows the numbering of conductors of double-circuit OHL. Traditionally to simplify the operation of OHL, conductors 1-3 make up the one three-phase line, and conductors 4-6 form the another one. We assume that both of them are symmetric. Then RMS values of currents in conductors 1-3 are equal to each other, i.e. $I_3=I_2=I_1$. Similarly, for the second line, $I_4=I_5=I_6$. Note that in the general case the values of currents I_1 and I_6 can be different.

Table 3 summarizes the geometric sizes of typical 110 kV double-circuit towers [6]. We see that geometric sizes of P110-4V type tower are the closest to average values. Therefore, in further double-circuit OHL magnetic field calculations, we assume a_1=2.1 m, h_1=19 m, a_2=4.2 m, h_2=23 m, a_3=2.1 m, h_3=27 m.

Table 3

Parameters of typical double-circuit towers
of 110 kV OHL

Tower type	a_1, m	h_1, m	a_2, m	h_2, m	a_3, m	h_3, m
P110-2	2.0	19	4.1	23	2.0	27
P110-4V	2.1	19	4.2	23	2.1	27
P110-4V+4	2.1	23	4.2	27	2.1	31
PM110-2F	2.4	19	4.7	23	2.4	27
PM110-4F	2.3	15	3.9	19	2.3	23
P110-6V	2.1	19	4.2	25	2.1	31
P110-6V+4	2.1	23	4.2	29	2.1	35
PS110-10V	2.6	19	4.2	25	2.6	31
PM110-8VR	2.4	19	3.3	25	2.4	31
PM110-6F	2.4	15	3.3	21	2.4	27
Average value	2.3	19	4.0	24	2.3	29

Magnetic field of double-circuit OHL. To find the double-circuit OHL magnetic field, we accept assumptions, within the framework of which (1) was obtained. So we use (1), replacing the upper limit of change from 3 to 6 for the counter p, to find the double-circuit OHL magnetic field distribution (See Fig. 6 and 7).

It is shown in [8, 11] that the double-circuit OHL magnetic field is minimal, when conductors with the same initial phase of currents are arranged centrally symmetrically. Fig. 6 shows the distribution of magnetic flux density isolines when $I_1=I_6$=500 A, $\varphi_1=\varphi_4=-2\pi/3$, $\varphi_2=\varphi_5=0$, $\varphi_3=\varphi_6=2\pi/3$. As before, the dotted line marks the contour of the residential building, located on the ROW border. We see that the magnetic field does not exceed the reference level of 0.5 µT in almost all living space, and the magnetic field normalization index is 99.2%.

The highest values of the double-circuit OHL magnetic field are achieved, when the rated current flows $I_1=I_6$=500 A and the initial phases $\varphi_1=\varphi_6=-2\pi/3$, $\varphi_2=\varphi_5=0$, $\varphi_3=\varphi_4=2\pi/3$. In this case, the magnetic field exceeds the reference level of 0.5 µT in the entire residential building (See Fig. 7).

Shielding of double-circuit OHL magnetic field. We determine the normalization index η for the residential building, located near a double-circuit OHL (Fig. 7), using plane and U-shaped grid shields. Note that the quantity of metal of each shield is V.
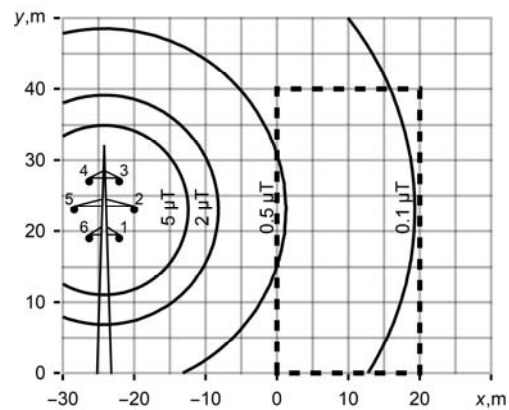

Fig. 6. Distribution of double-circuit OHL magnetic field
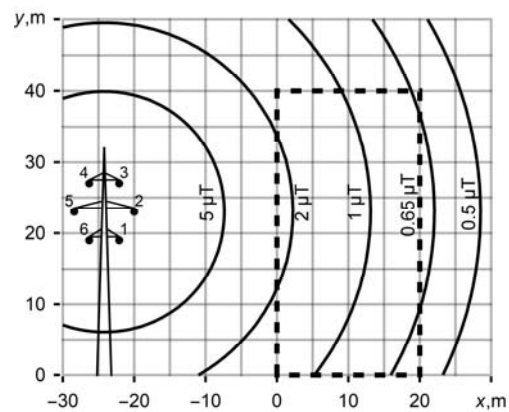when $\varphi_1=\varphi_4$, $\varphi_3=\varphi_6$

Fig. 7. Distribution of double-circuit OHL magnetic field
when $\varphi_1=\varphi_6$, $\varphi_3=\varphi_4$

Shields parameters are given in previous sections: the number of conductors is 81 and 121, respectively, and conductor diameter is 8 mm and 6.5 mm, respectively. Fig. 8 and Fig. 9 show magnetic flux density isolines when the double-circuit OHL magnetic field is mitigated with the plane and the U-shaped grid shield, respectively.

When using the plane grid shield, the magnetic field does not exceed the reference level of 0.5 μT in the bigger part of the residential building. However, as in the case of the single-circuit OHL, the plane shield does not provide the sufficient magnetic field mitigation in corner areas of the residential building. At the same time, the magnetic flux density does not exceed the reference level in almost the entire building, when the U-shaped grid shield is used to mitigate the double-circuit OHL magnetic field.

The analysis of magnetic field distributions, presented in Fig. 8 and Fig. 9, allows determining the normalization index η. According to (2), it is 83.9% when using plane shield and 98.7% when using U-shaped grid shield with quantity of metal V.

Table 4 shows η when varying the quantity of metal of the shield. We see that it is advisable to use the U-shaped grid shield with the volume of $0.75 \cdot V$ to mitigate the double-circuit OHL magnetic field. Therefore, the diameter of shield conductors can be reduced to 5.7 mm, while maintaining the number of conductors and their arrangement. In this case, the magnetic field normalization index η of the residential building is 97%, which makes it possible to use 97% of its living space.
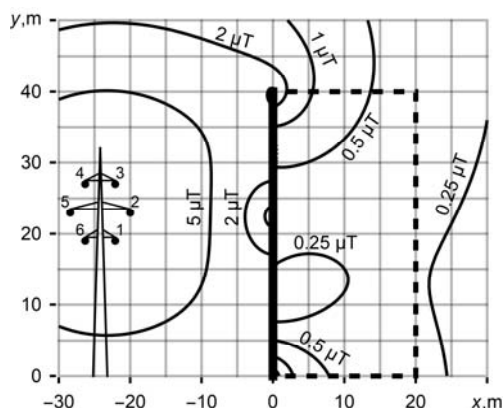

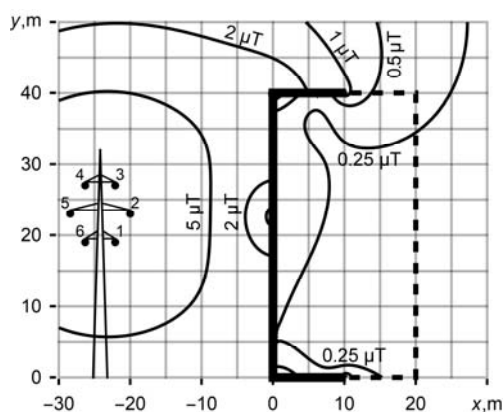Fig. 8. Distribution of double-circuit OHL magnetic field when using plane grid shield

Fig. 9. Distribution of double-circuit OHL magnetic field when using U-shaped grid shield

Table 4

Magnetic field normalization index η
for residential building located near double-circuit OHL
when using grid shield

Quantity of metal of shield referred to V	η, %	
	Usage of plane shield	Usage of U-shaped shield
0.2	15.0	27.7
0.3	41.6	52.9
0.4	60.7	70.6
0.5	69.7	82.8
0.6	75.2	90.4
0.75	80.3	97.0
0.8	81.3	97.9
1.0	83.9	98.7
1.2	85.2	99.0

The obtained results confirm the efficiency of grid shields for the magnetic field normalizing in residential buildings, located on the ROW border of typical 110 kV overhead lines, and allow formulating recommendations for the design of grid shields.

Conclusions.

1. We show that the plane grid shield made of aluminum 8 mm diameter conductors and mounted on the wall of the residential building facing 110 kV trefoil single-circuit or double-circuit overhead line mitigates the magnetic field to the reference level of 0.5 μT in the bigger part of the living space.

2. To normalize the magnetic field in the entire residential building located on the border of the right-of-way of 110 kV overhead line, it is advisable to use the U-shaped grid shield.

3. The efficient usage of the grid shield is achieved, when the distance between its adjacent conductors is less than 0.5 m, and the conductor diameter is at least 4.6 mm for 110 kV trefoil OHL magnetic field mitigation and at least 5.7 mm for 110 kV double-circuit OHL magnetic field mitigation.

REFERENCES
1. Pelevin D.Ye. The methods of reducing of the magnetic fields of overhead power lines outside security zones. *Technical Electrodynamics*, 2014, no. 5, pp. 14-16. (Rus).
2. Electrical installation regulations. Kharkiv, Fort Publ., 2017. 760 p. (Ukr).
3. Decree of the Cabinet of Ministries of Ukraine dated March 4, 1997 No. 209 *«About the statement of Rules of protection of electric networks»*, edition on April 5, 2017. (Ukr).
4. Grinchenko V.S. Mitigation of three-phase power line magnetic field by grid electromagnetic shield. *Technical Electrodynamics*, 2018, no. 4, pp. 29-32. (Ukr). **doi: 10.15407/techned2018.04.029.**
5. Grinchenko V., Pyrohova U. Mitigation of overhead line magnetic field by U-shaped grid shield. *Proc. 2019 IEEE 2nd Ukraine Conference on Electrical and Computer Engineering (UKRCON)*, Lviv, Ukraine, 2019, pp. 345-348, **doi: 10.1109/UKRCON.2019.8879834.**
6. Rokotian S., Zelichenko A., Levin L., et al. *Typical project 3.407-68/73. Unified steel normal supports of overhead lines 35, 110 and 150 kV. Volume 1.* Moscow, 1973. 66 p. (Rus).

7. Rozov V., Grinchenko V. Simulation and analysis of power frequency electromagnetic field in buildings closed to overhead lines. *Proc. 2017 IEEE First Ukraine Conference on Electrical and Computer Engineering (UKRCON)*. Kyiv, Ukraine, pp. 500-503. **doi: 10.1109/UKRCON.2017.8100538**.

8. Mazzanti G. Current phase-shift effects in the calculation of magnetic fields generated by double-circuit overhead transmission lines. *Proc. IEEE Power Engineering Society General Meeting*, 2004, pp. 413-418. **doi: 10.1109/PES.2004.1372827.**

9. Grinchenko V.S. Development of a semi-analytical model of a grid shield for the magnetic field mitigation of overhead lines. *Proc. VII All-Ukrainian Scientific Conf. of Young Scientists «Information Technologies – 2020»*, pp. 149-151. (Ukr).

10. SOU-N EE 20.179:2008. Calculation of electric and magnetic fields of power lines. Method (with changes). Kyiv, Minenergovugillja Ukrainy Publ., 2016. 37 p. (Ukr).

11. Rozov V.Yu., Reutskyi S.Yu., Pelevin D.Ye., Pyliugina O.Yu. The magnetic field of power transmission lines and the methods of its mitigation to a safe level. *Technical Electrodynamics*, 2013, no. 2, pp. 3-9. (Rus).

V.S. Grinchenko[1]*, K.V. Chunikhin*[1]
[1] State Institution "Institute of Technical Problems of Magnetism of the National Academy of Sciences of Ukraine",
19, Industrialna Str., Kharkiv, 61106, Ukraine,
e-mail: vsgrinchenko@gmail.com, kvchunikhin@gmail.com

V.M. Mikhailov

ON THE SIMILARITY OF PLANE PULSED MAGNETIC FIELDS CONTINUED FROM DIFFERENT COORDINATE AXES

Purpose. The purpose of this work is formulation of similarity conditions for plane magnetic fields at a sharp skin-effect continued in non-conducting and non-magnetic medium from different axes bounding plane surfaces of conductors. Methodology. Classic formulation of Cauchy problem for magnetic vector potential Laplace equations, mathematic physics methods and basics similarity theory are used. Two problems are considered: the problem of initial field continuation from one axis and the problem of similar field continuation form other axis on which magnetic flux density or electrical field strength in unknown. Results. Necessary and sufficient similarity conditions of plane pulsed or high-frequency magnetic fields continued from different axes of rectangular coordinates are formulated. For the given odd and even magnetic flux density distributions on axis of initial field corresponding the distributions on axis and solution of continued similar field problem are obtained. Originality. It is proved that for similarity of examined fields the proportion of corresponding vector field projections represented by dimensionless numbers in similar points of axes is necessary and sufficient. References 11, figures 4.
Key words: **plane magnetic field, sharp skin-effect, Cauchy problem for Laplace equation, similarity theory.**

Мета. Метою роботи є формулювання умов подібності плоскопаралельних магнітних полів при різкому поверхневому ефекті, що продовжуються в непровідне і немагнітне середовище з різних осей прямокутних координат, котрі обмежують плоскі поверхні провідників. Методика. Використано класичне формулювання задачі Коші для рівняння Лапласа відносно векторного потенціалу магнітного поля, методи математичної фізики та основні положення теорії подібності. Розглянуто дві відповідні задачі: задача продовження вихідного поля з однієї осі та задача продовження подібного поля з іншої осі, розподіл індукції магнітного поля на котрій є невідомим. Результати. Сформульовано необхідні та достатні умови подібності плоскопаралельних імпульсних або високочастотних магнітних полів, що продовжуються з різних осей прямокутних координат. Для заданих непарного та парного розподілів індукції на осі вихідного магнітного поля визначено відповідні розподіли на осі, а також розв'язані задачі продовження подібного поля. Наукова новизна. Доведено, що для подібності полів, які розглянуто, необхідна та достатня пропорційність представлених у критеріальній формі відповідних проекцій векторів цих полів у схожих точках осей. Бібл. 11, рис. 4.
Ключові слова: **плоскопаралельне магнітне поле, різкий поверхневий ефект, задача Коші для рівняння Лапласа, теорія подібності.**

Цель. Целью работы является формулировка условий подобия плоскопараллельных магнитных полей при резком поверхностном эффекте, которые продолжаются в непроводящую и немагнитную среду с различных осей прямоугольных координат, ограничивающих плоские поверхности проводников. Методика. Использованы классическая формулировка задачи Коши для уравнения Лапласа относительно векторного потенциала магнитного поля, методы математической физики и основные положения теории подобия. Рассмотрены две соответствующие задачи: задача продолжения исходного поля с одной оси и задача продолжения подобного поля с другой оси, распределение индукции магнитного поля на которой неизвестно. Результаты. Сформулированы необходимые и достаточные условия подобия плоскопараллельных импульсных или высокочастотных магнитных полей, продолжаемых с различных осей прямоугольных координат. Для заданных нечетного и четного распределений индукции на оси исходного магнитного поля определены соответствующие распределения на оси, а также решены задачи продолжения подобного поля. Научная новизна. Доказано, что для подобия рассмотренных полей необходима и достаточна пропорциональность представленных в критериальной форме соответствующих проекций векторов этих полей в сходственных точках осей. Библ. 11, рис. 4.
Ключевые слова: **плоскопараллельное магнитное поле, резкий поверхностный эффект, задача Коши для уравнения Лапласа, теория подобия.**

Introduction. The shape of massive solenoids (inductors) and electrodes used in electrophysical technologies to obtain electromagnetic fields of a given distribution is found by solving the field continuation problem [1-3]. We restrict ourselves to considering plane pulsed or high-frequency magnetic fields, continued from one of the axes of rectangular coordinates (for example, the *x*-axis) [4]. The problem definition includes the distribution of a certain projection of the vector of the extended field specified on this axis. In practice, it may be necessary to solve the problem of continuation of a field with a similar distribution on the *y*-axis. In this case, it is obvious to use the results obtained for the *x*-axis. The main difficulty of this approach lies, first of all, in

insufficient theoretical substantiation, as a result of which the given field distribution on the *y*-axis turns out to be unknown.

The goal of the work is a formulation of conditions for the similarity of plane magnetic fields at a sharp skin-effect, which continue into a non-conductive and non-magnetic medium from different axes of rectangular coordinates that limit the flat surfaces of the conductors.

Conditions for the similarity of magnetic fields extended from flat surfaces of conductors. In a massive conductor with a flat boundary surface eddy currents are induced under the action of a pulsed or high-frequency magnetic field of an external inductor, the profile of

which must be determined. The skin-effect is sharply manifested in the conductor. Let us accept the assumption of an ideal surface effect [3] and replace the conductor with an ideally superconducting half-space. We use three systems of Cartesian coordinates on the plane: the main (general) xOy and two auxiliary ones – x_1Oy_1 and x_2Oy_2. Consider two corresponding problems of continuation of a plane magnetic field into non-magnetic non-conducting half-spaces $y_1 > 0$ and $x_2 > 0$ without sources (Fig. 1): from the x_1 axis (the first problem whose solution is known) and from the y_2 axis (the second problem). Half-spaces $y_1 < 0$ and $x_2 < 0$ are ideal superconductors.

Equation for the magnetic vector potential $A(x, y)$ of such fields has the form [5]

$$\frac{\partial^2 A}{\partial x^2} + \frac{\partial^2 A}{\partial y^2} = 0 . \tag{1}$$

In (1) $x = x_1 \vee x_2$, $y = y_1 \vee y_2$, $A(x, y) = A_1(x_1, y_1) \vee A_2(x_2, y_2)$. Boundary conditions on the x_1-axis –

$$A_1(x_1, 0) = 0 , \quad \left.\frac{\partial A_1}{\partial y_1}\right|_{y_1=0} = B_{1x}(x_1, 0), \tag{2, 3}$$

on the y_2-axis –

$$A_2(0, y_2) = 0 , \quad \left.\frac{\partial A_2}{\partial x_2}\right|_{x_2=0} = -B_{2y}(0, y_2), \tag{4, 5}$$

where $B_{1x}(x_1, 0)$ and $B_{2y}(0, y_2)$ are the projections of the magnetic flux density $\vec{B}_1(x_1, y_1)$, $y_1 \geq 0$ and $\vec{B}_2(x_2, y_2)$, $x_2 \geq 0$ on the x_1, y_2 axes.
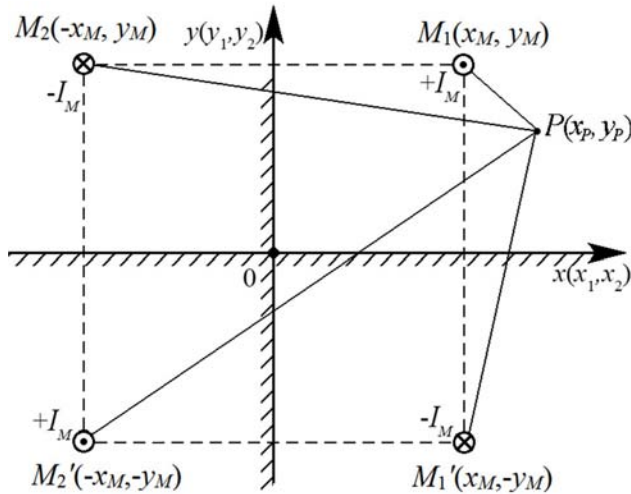

Fig. 1. Systems of coordinates and parallel axes with currents creating specified distributions of magnetic flux density (8)

Note that $B_{1x}(x_1, 0)$ is a given function, and the projection $B_{2y}(0, y_2)$ is to be determined. Comparing the formulations of the two considered problems (1)-(3) and (1), (4), (5), we note that they have geometrically similar solution domains (half-spaces $y_1 > 0$ and $x_2 > 0$, Fig. 1) with the same physical properties, contain an equation of the same type and similar boundary conditions (2), (4) on the x_1 and y_2 axes from which the fields continue. The described conditions are necessary, but they are not enough for the similarity: the boundary conditions (3), (5) remain.

Let us assume that the considered magnetic fields are similar. Then it follows from (1) – (5) that the similar coordinates [6-8] in the field continuation domains are x_1 and y_2, y_1 and x_2, and the corresponding functions are $A_1(x_1, y_1)$ and $A_2(x_2, y_2)$. Therefore, analogous quantities characterizing supposedly similar fields should be

$$\frac{\partial A_1}{\partial x_1} \text{ and } \frac{\partial A_2}{\partial y_2} , \quad \frac{\partial A_1}{\partial y_1} \text{ and } \frac{\partial A_2}{\partial x_2} , \text{ or}$$

$-B_{1y}(x_1, y_1)$ and $B_{2x}(x_2, y_2)$, $B_{1x}(x_1, y_1)$ and $-B_{2y}(x_2, y_2)$. (6, 7)

Let P be the observation point of the field with coordinates $x_P = x_{1P} \vee x_{2P}$, $y_P = y_{1P} \vee y_{2P}$ (Fig. 1). Then the similar coordinates of the point P will be x_{1P} and y_{2P}, y_{1P} and x_{2P}.

Taking into account the main provisions of the similarity theory [6-8], in addition to the noted necessary conditions, we can assert the following: for the similarity of two compared magnetic fields, it is necessary and sufficient that the values of the presented in criterial form magnetic flux density projections $B_{1x}(x_1, 0)$ and $B_{2y}(0, y_2)$ at similar points of the axes, from which these fields continue, should be proportional.

This condition allows to find $B_{2y}(0, y_2)$ and thus obtain a complete formulation of the second problem.

Magnetic flux density distribution on the y_2 axis for a similar magnetic field. Let in the first problem the given distributions of the magnetic flux density on the x_1-axis can be represented by the formula

$$B_{1x}(x_1, 0) = \frac{\mu_0 I_{1M}}{\pi} \left\{ y_{1M} \left[\frac{1}{(x_1 - x_{1M})^2 + y_{1M}^2} \mp \right. \right.$$
$$\left. \left. \mp \frac{1}{(x_1 + x_{1M})^2 + y_{1M}^2} \right] \right\}, \tag{8}$$

where μ_0 is the magnetic constant, I_{1M}, x_{1M}, y_{1M} are the distribution parameters.

The function in curly brackets of formula (8) is odd or even, depending on the minus or plus sign between the terms in square brackets. In both cases, it has the well-known sine or cosine Fourier transform. The multiplier before of the considered function is constant therefore $B_{1x}(x_1, 0)$ also has such transform. The physical meaning of (8) is the magnetic flux density created on the x_1-axis by a system of four parallel, symmetrically located axes with currents $\pm I_M = \pm I_{1M}$, two of which (M_1' and M_2') replace the influence of the lower ideally superconducting half-space [9, 10] (Fig. 1). The parameters $x_M = x_{1M}$, $y_M = y_{1M}$ determine the position of the axes at the points M_1, M_1', M_2, M_2' of the x_1Oy_1 plane. Currents $+I_M$ have positive directions, and $-I_M$ have negative ones, indicated by a dot or a cross, respectively. For the currents in Fig. 1 we obtain an odd magnetic flux density distribution. If the currents in the upper half-space have the same (for example, positive) direction (while the currents in the lower half-space are also directed in the same way, but opposite to the first ones), we have an even distribution of magnetic flux density.

Let us find such distributions $B_{2y}(0, y_2)$ on the y_2-axis that satisfy the necessary and sufficient similarity condition formulated above. To do this, we first establish

similar parameters [6-8] of the distributions $B_{1x}(x_1, 0)$ and $B_{2y}(0, y_2)$: I_{1M} and I_{2M}, x_{1M} and y_{2M}, y_{1M} and x_{2M}, where I_{2M}, x_{2M} and y_{2M} are the parameters of the distributions $B_{2y}(0, y_2)$ unknown so far. Then, using the correspondence of similar values (7), we replace in formula (8) the coordinates and parameters with similar coordinates and parameters of the second problem. We obtain:

$$B_{2y}(0, y_2) = -\frac{\mu_0 I_{2M}}{\pi}\left\{x_{2M}\left[\frac{1}{(y_2 - y_{2M})^2 + x_{2M}^2} \mp \right.\right.$$
$$\left.\left. \mp \frac{1}{(y_2 + y_{2M})^2 + x_{2M}^2}\right]\right\}. \quad (9)$$

We represent (8), (9) in dimensionless form (in criterial form) using two systems of basic quantities: l_{1b} and l_{2b} – length, I_{1b} and I_{2b} – current, B_{1b} and B_{2b} – magnetic flux density (basic values for formula (8) have number 1 in the subscript, for (9) – number 2). Dimensionless quantities are obtained by dividing the corresponding dimensional ones by the basic ones and marked with asterisks. After transformations formulas (8), (9) take the following form:

$$B_{1x}^*\left(x_1^*, 0\right) = \frac{1}{\pi} I_{1M}^* y_{1M}^*\left[\frac{1}{\left(x_1^* - x_{1M}^*\right)^2 + y_{1M}^{*2}} \mp \right.$$
$$\left. \mp \frac{1}{\left(x_1^* + x_{1M}^*\right)^2 + y_{1M}^{*2}}\right], \quad -\infty < x_1^* < \infty; \quad (10)$$

$$B_{2y}^*\left(0, y_2^*\right) = -\frac{1}{\pi} I_{2M}^* x_{2M}^*\left[\frac{1}{\left(y_2^* - y_{2M}^*\right)^2 + x_{2M}^{*2}} \mp \right.$$
$$\left. \mp \frac{1}{\left(y_2^* + y_{2M}^*\right)^2 + x_{2M}^{*2}}\right], \quad -\infty < y_2^* < \infty. \quad (11)$$

Comparing (10) and (11), we see that for
$$x_{1M}^* = y_{2M}^*, \quad y_{1M}^* = x_{2M}^* \quad (12)$$
at similar points on the x_1 and y_2 axes with coordinates $x_1^* = y_2^*$, the values $B_{1x}^*\left(x_1^*, 0\right)$ are proportional to the values $B_{2y}^*\left(0, y_2^*\right)$. Consequently, the necessary and sufficient similarity condition is satisfied, and the sought distributions $B_{2y}(0, y_2)$ for such a magnetic field have the form (9). If in addition to (12) to accept
$$I_{1M}^* = I_{2M}^*, \quad (13)$$
then the absolute values of the compared magnetic flux density values will be equal, although this is not necessary for similarity.

All quantities included in conditions (12), (13) are similarity criteria. We choose the basic values l_{1b}, l_{2b} in such a way that conditions (12) are satisfied. In the general case, I_{1b} and I_{2b} can be any, but, if necessary, we find them taking into account condition (13). When determined $B_{1x}^*\left(x_1^*, 0\right)$ and $B_{2y}^*\left(0, y_2^*\right)$, we accepted $B_{1b} = \mu_0 I_{1b}/l_{1b}$, $B_{2b} = \mu_0 I_{2b}/l_{2b}$.

The physical meaning of distributions (9) is similar to that described for (8): the magnetic flux density created on the y_2 axis by four parallel axes with currents $\pm I_M = \pm I_{2M}$ (the axes are located at points whose coordinates $\pm x_M$ and $\pm y_M$ are determined by the parameters $\pm x_{2M}$ and $\pm y_{2M}$, Fig. 1).

Figure 2 shows the symmetric parts of the odd (*a*) and even (*b*) distributions of the magnetic flux density on the axes at $x_1 \geq 0$ and $y_2 \geq 0$, calculated by (10), (11). Accepted: $l_{1b} = l_{2b}$, $I_{1b} = I_{2b}$, $I_{1M} = I_{2M}$; для curves $1 - x_{1M}^* = 0,1$, $y_{1M}^* = 0,1$; $2 - 0,25, 0,1$; $3 - 0,15, 0,2$; $4 - 0,25, 0,2$. The values x_{2M}^* and y_{2M}^* are determined using relations (12). The coincidence of the distributions $B_{1x}^*\left(x_1^*, 0\right)$ and $-B_{2y}^*\left(0, y_2^*\right)$ illustrates the necessary and sufficient condition for the similarity of magnetic fields.
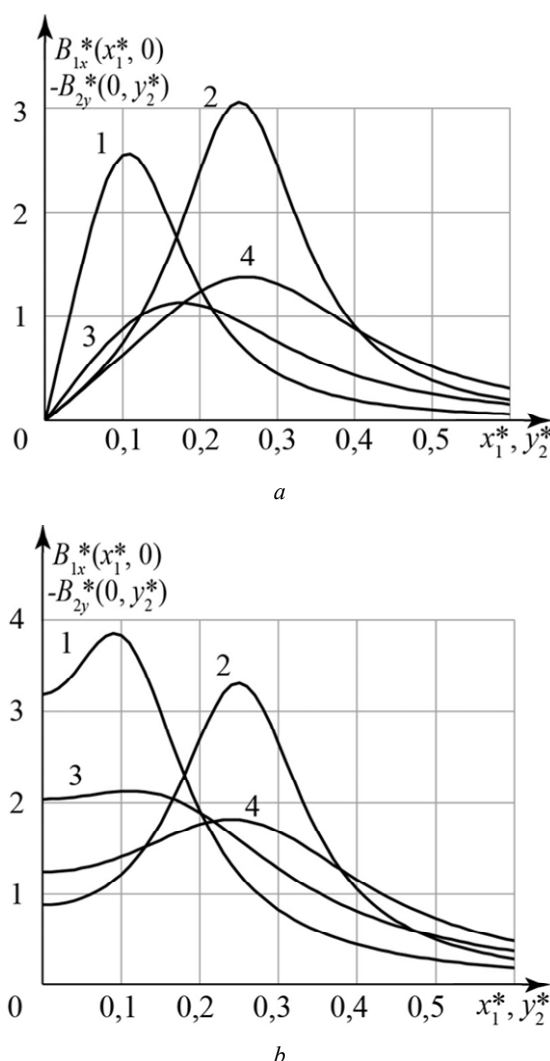

Fig. 2. Odd (*a*) and even (*b*) distributions of the magnetic flux density on the axes x_1, y_2

Continuation of similar magnetic fields by solving the first problem. The solutions of the first problem (1)-(3), taking into account (8), obtained by the method of particular solutions that continuously depend on the parameter, have the following form:

$$A_1(x,y) = \frac{2\mu_0 I_M}{\pi} \int_0^\infty e^{-y_M \lambda} \begin{Bmatrix} \sin(x_M \lambda)\sin(x\lambda) \\ \cos(x_M \lambda)\cos(x\lambda) \end{Bmatrix} \times \quad (14)$$

$$\times \lambda^{-1} \operatorname{sh}(y\lambda)d\lambda, \quad -\infty < x < \infty, \; 0 < y < y_M.$$

The first line of the multiplier of the integrand in curly braces (14) refers to the odd distribution $B_{1x}(x_1, 0)$, the second – to the even one.

The solutions of the second problem (1), (4), (5) taking into account (9) are found by replacing coordinates and parameters in (14) by similar values of a similar field. We obtain:

$$A_2(x,y) = \frac{2\mu_0 I_M}{\pi} \int_0^\infty e^{-x_M \lambda} \begin{Bmatrix} \sin(y_M \lambda)\sin(y\lambda) \\ \cos(y_M \lambda)\cos(y\lambda) \end{Bmatrix} \times \quad (15)$$

$$\times \lambda^{-1} \operatorname{sh}(x\lambda)d\lambda, \quad -\infty < y < \infty, \; 0 < x < x_M.$$

In (14), (15)) $I_M = I_{1M} \vee I_{2M}$, $x_M = x_{1M} \vee x_{2M}$, $y_M = y_{1M} \vee y_{2M}$. The constraints $y < y_M$ and $x < x_M$ are due to the convergence of improper integrals [4]. The correctness of the described method for determining such a magnetic field and, in particular, (15) is confirmed by the coincidence of the latter with the solution of the second problem by the same method as the first one.

Another method for solving the first problem is to use the Green function for an axis with a unit current located in a non-magnetic and non-conductive medium parallel to the surface of an ideally superconducting half-space. For the odd distribution $B_{1x}(x_1, 0)$ (8) we have [10]:

$$A(P) = \frac{\mu_0 I_M}{\pi} \ln\left[\frac{r_{M_1' P} r_{M_2 P}}{r_{M_1 P} r_{M_2' P}}\right], \quad (16)$$

where $r_{M_1 P}$, $r_{M_1' P}$, $r_{M_2 P}$, $r_{M_2' P}$ is the distance between points P and, accordingly, M_1, M_1', M_2, M_2' (Fig. 1).

Using the known relationship between the magnetic flux density and the vector potential of the magnetic field [5] and (16) to calculate the projections, we obtain the following formulas:

$$B_{1x}(P) = -\frac{\mu_0 I_M}{2\pi}\left[(y_P - y_M)\left(\frac{1}{r_{M_1 P}^2} - \frac{1}{r_{M_2 P}^2}\right) + \right.$$
$$\left. + (y_P + y_M)\left(\frac{1}{r_{M_2' P}^2} - \frac{1}{r_{M_1' P}^2}\right)\right]; \quad (17)$$

$$B_{1y}(P) = \frac{\mu_0 I_M}{2\pi}\left[(x_P - x_M)\left(\frac{1}{r_{M_1 P}^2} - \frac{1}{r_{M_1' P}^2}\right) + \right.$$
$$\left. + (x_P + x_M)\left(\frac{1}{r_{M_2' P}^2} - \frac{1}{r_{M_2 P}^2}\right)\right]. \quad (18)$$

Note that in (16) – (18) it is assumed that the observation point P is located in the upper half-space $y > 0$ (in a particular case, on the x-axis). Let us find $B_{2x}(P)$ and $B_{2y}(P)$ for a similar magnetic field in the

region $x > 0$ (in a particular case on the y-axis), replacing coordinates and parameters in (17), (18) with similar values. We obtain surprising, at first glance, results: the formulas for determining $B_{2x}(P)$ and $B_{2y}(P)$ formally coincide with (17), (18). The reason is that a system of four axes with currents, which creates a magnetic field in the region $y > 0$ of the first problem (for more details, in the physical sense of (8)), simultaneously creates a similar magnetic field in the region $x > 0$. Here, the axes located in points M_2 and M_2' (Fig. 1), replace the influence of an ideally superconducting half-space $x < 0$. Therefore, formula (16) is also a solution of the second problem for a similar magnetic field in the region $x > 0$ in the case of an odd distribution $B_{2y}(0, y_2)$.

When using the Green function in the case of even distributions $B_{1x}(x_1, 0)$ and $B_{2y}(0, y_2)$, it is necessary to change the directions of currents in two axes to the opposite with respect to those adopted in Fig. 1: for the original field – in the M_2 and M_2' axes, for a similar field – in the M_1' and M_2' axes. In contrast to odd distributions of the magnetic flux density on the axes, the vector potential $A(P)$ is described by two different formulas. We obtain them from formula (16), having changed places $r_{M_2 P}$ and $r_{M_2' P}$ for the original field, $r_{M_1' P}$ and $r_{M_2' P}$ for a similar field:

$$A_1(P) = \frac{\mu_0 I_{1M}}{\pi} \ln\left[\frac{r_{M_1' P} r_{M_2' P}}{r_{M_1 P} r_{M_2 P}}\right], \quad (19)$$

$$A_2(P) = \frac{\mu_0 I_{2M}}{\pi} \ln\left[\frac{r_{M_2 P} r_{M_2' P}}{r_{M_1 P} r_{M_1' P}}\right]. \quad (20)$$

Formulas for calculating magnetic flux density projections $B_{1x}(P)$ and $B_{1y}(P)$, $B_{2x}(P)$ and $B_{2y}(P)$ differ from (17), (18) in opposite signs before the fractions $1/r_{M_2 P}^2$ and $1/r_{M_2' P}^2$, $1/r_{M_1' P}^2$ and $1/r_{M_2' P}^2$. The correctness of the transforms is confirmed by the correspondence of the obtained formulas to the relations (6), (7).

Figures 3, 4 show the magnetic field lines of the initial and similar magnetic fields $A(x, y) = $ const, calculated by (16), (19), (20) for the distributions of the magnetic flux density 2 in Fig. 2,a,b. It is accepted that $A^* = A/A_b$, $A_b = \mu_0 I_M$, $A_b = A_{1b} \vee A_{2b}$, $A_{1b} = A_{2b}$, $l_{1b} = l_{2b}$. For magnetic field lines $1, 5 - A_1^* = A_2^* = 0.05$, $2, 6 - 0.1$, $3, 7 - 0.15$, $4, 8 - 0.2$.

We see that the corresponding field lines of the considered magnetic fields are geometrically similar, which confirms the correctness of the obtained results. The field lines shown in Fig. 4,a,b, limit the profiles of current-conducting inductors to create pulsed or high-frequency magnetic fields of given distributions on the axis y_2.
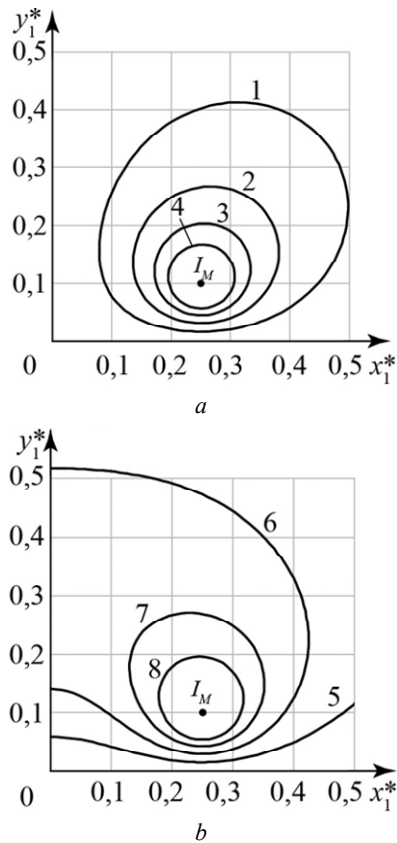
Fig. 3. Magnetic field lines at odd (*a*) and even (*b*) distributions
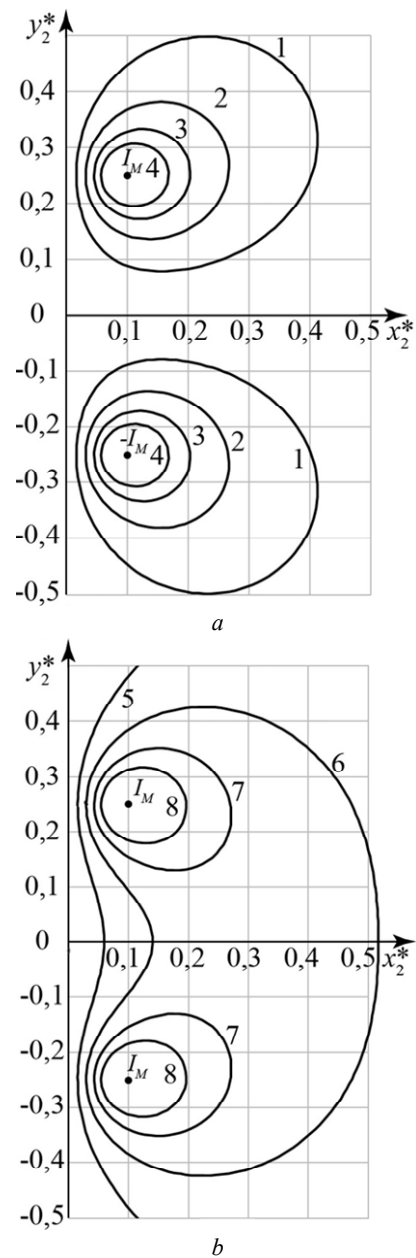of the magnetic flux density on the axis x_1

Fig. 4. Magnetic field lines at odd (*a*) and even (*b*) distributions
of the magnetic flux density on the axis y_2

The results obtained for the magnetic field can be used to determine the profiles of one or more long parallel uniformly charged electrodes, with the help of which an electrostatic field of a given distribution is to be created on the flat surface of the conductor. For this we use the electrostatic analogy of plane electrostatic and magnetic fields of conductors with a sharp skin-effect (J.D. Cockroft, 1929, [4]), according to which the distributions of the taken with a minus sign projection of the electric field strength $E_{1y}(x_1, 0)$ and $B_{1x}(x_1, 0)$ correspond to one another.

Appendix. The use of two methods for solving field continuation problems allows not only checking the results, but also obtaining formulas for calculating complex improper integrals that are absent in the reference literature [11]. For example, comparing formulas (14) and (19) for the initial field, we have two improper integrals:

$$\int_0^\infty e^{-y_M\lambda}\lambda^{-1}\begin{Bmatrix}\sin(x_M\lambda)\sin(x\lambda)\\\cos(x_M\lambda)\cos(x\lambda)\end{Bmatrix}\text{sh}(y\lambda)d\lambda =$$

$$= \frac{1}{8}\ln\left\{\frac{(x-x_M)^2+(y+y_M)^2}{(x-x_M)^2+(y-y_M)^2}\times\right. \tag{21}$$

$$\left.\times\left[\frac{\dfrac{(x+x_M)^2+(y-y_M)^2}{(x+x_M)^2+(y+y_M)^2}}{\dfrac{(x+x_M)^2+(y+y_M)^2}{(x+x_M)^2+(y-y_M)^2}}\right]\right\}.$$

The limits of *x* and y change are the same as in (14). In the described way, one can obtain several more formulas for calculating improper integrals using (17), (18), as well as the corresponding formulas for a similar field. Comparison of (15) with (20) leads to a number of improper integrals. For instance:

$$\int_0^\infty e^{-x_M\lambda}\lambda^{-1}\begin{Bmatrix}\sin(y_M\lambda)\sin(y\lambda)\\\cos(y_M\lambda)\cos(y\lambda)\end{Bmatrix}\text{sh}(x\lambda)d\lambda =$$

$$= \frac{1}{8}\ln\left\{\frac{(x+x_M)^2+(y-y_M)^2}{(x-x_M)^2+(y-y_M)^2}\times\right. \tag{22}$$

$$\left.\times\left[\frac{\dfrac{(x-x_M)^2+(y+y_M)^2}{(x+x_M)^2+(y+y_M)^2}}{\dfrac{(x+x_M)^2+(y+y_M)^2}{(x-x_M)^2+(y+y_M)^2}}\right]\right\}.$$

We see that formula (22) differ from (21) only by similar values of a similar magnetic field. In addition, it is necessary to take into account also other limits of variation of x and y (see formula (15)).

Conclusions.

1. For the similarity of plane pulsed or high-frequency magnetic fields continued into a non-magnetic and non-conductive medium from different axes of Cartesian coordinates that bound the flat surfaces of the conductors, it is necessary and sufficient that the values of the corresponding projections of the magnetic flux density presented in the criterial form at similar points of the axes are proportional. This condition makes it possible to find the distribution of the magnetic flux density on the axis from which the similar field continues.

2. Solutions to the problems of the continuation of similar magnetic fields can be obtained from the known solutions of the problems of the continuation of the initial fields by replacing the coordinates and parameters in them with the corresponding similar quantities.

REFERENCES
1. Belyj I.V., Fertik S.M., Himenko L.T. Directory of magnetic-pulse treatment of metals. Kharkov, Vysshaia shkola Publ., 1977. 168 p. (Rus).
2. Shneerson G.A. Fields and transients in equipment ultra strong currents. Moscow, Energoatomizdat Publ., 1992. 416 p. (Rus).
3. Gurbanov G.G., Kas'iankov P.P., Taganov I.N. Propagation of the field potential along a given distribution on the axis. *Radio engineering and electronics*, 1967, no. 4, pp. 659-661. (Rus).
4. Mikhailov V.M. Shapes determination of the electrodes and coils to generate predetermined field distributions. *Technical electrodynamics. Thematic issue «Problems of modern electrical engineering»*, 2000, part 6, pp. 13-16. (Rus).
5. Tozoni O.V. Calculation of electromagnetic fields on computers. Kiev, Tekhnika Publ., 1967. 252 p. (Rus).
6. Kirpichev M.V., Konakov P.K. Mathematical foundations of similarity theory. Moscow-Leningrad, Acad. of Sci. USSR Publ., 1949. 104 p. (Rus).
7. Eigenson L.S. Modeling. Moscow, Sovetskaia nauka Publ., 1952. 372 p. (Rus).
8. Venikov V.A., Venikov G.V. The theory of similarity and modeling (in relation to the problems of the electric power industry). Moscow, Vysshaia shkola Publ., 1984. 439 p. (Rus).
9. Vasetskii Iu.M., Vlasov D.I., Konovalov O.Ia., Mikhailov V.M. Some solutions to the problem of continuation of a plane field in elementary functions. *Proceedings of the conference SIMULATION-2012*, Kiev, 2012, pp. 232-236 (Rus).
10. Valery Mikhailov, Mykyta Petrenko. Inductor shape determination for electromagnetic forming of sheet workpieces. *Przeglad Elektrotechniczny*, 2020, no. 1, pp. 74-77. **doi: 10.15199/48.2020.01.18.**
11. Gradshtein I.S., Ryzhik I.M. Tables of integrals, sums, series and products. Moscow, Nauka Publ., 1971. 1108 p. (Rus).

V.M. Mikhailov, Doctor of Technical Science, Professor,
National Technical University «Kharkiv Polytechnic Institute»,
2, Kyrpychova Str., Kharkiv, 61002, Ukraine,
e-mail: valery.m.mikhailov@gmail.com

M.I. Baranov, S.G. Buriakovskyi, V.V. Kniaziev

POWERFUL HIGH-CURRENT GENERATOR OF MICROSECOND VOLTAGE PULSES WITH VOLTAGE AMPLITUDE UP TO ±2 MV AND CURRENT AMPLITUDE UP TO ±150 KA WITH ELECTRIC ENERGY STORED IN CAPACITORS UP TO 1 MJ

Purpose. Development and evaluation, on the basis of existing ultra-high-voltage generator of pulsed voltages and currents of GINT-4 type, of the new scheme of design of its charging-discharging circuit (CDC), and creation of modernized powerful ultra-high-voltage high-current generator of GINT-2 type to form microsecond voltage pulses with amplitudes up to ±2 MV and current with amplitude up to ±150 kA in the electrical load, with electrical energy stored in its capacitive energy storage (CES) up to 1 MJ. Methodology. Fundamentals of theoretical and applied electrical engineering, electrical power engineering, electrophysical principles of high-voltage and high pulsed current engineering, fundamentals of electromagnetic compatibility (EMC), instrument engineering, high-voltage instrumentation and standardization. Results. The new scheme of design of CDC of the modernized powerful ultra-high-voltage, heavy-current generator of GINT-2 type of outdoor placement, that allows obtaining, with preservation of the main electrotechnical elemental base of existing powerful prototype generator GINT-4 (rated output voltage ±4 MV with rated electrical energy stored in CES of 1 MJ and maximal amplitude of output current pulse in electrical load up to ±75 kA) pulses of current of microsecond duration with doubled amplitude (up to ±150 kA) in the long (from 1 to 4 m length) air gap of standard two-electrode discharging «needle-plane» system, in comparison with parameters of current pulses with amplitudes up to ±75 kA that are formed in the discharging circuit of generator of GINT-4 type with the use of the analogous air discharging system, has been developed. Experimental evaluations of the developed new discharging circuit in CDC of the modernized generator of GINT-4 type has been performed in field conditions, and its advantages over the old discharging circuit in composition of CDC of generator of GINT-4 type have been shown. Calculated evaluations of rise rates of high pulsed current (HPC) in plasma channel of air spark discharge of CES with energy up to 1 MJ of generator of GINT-2 type, and strength of electric and magnetic field that are formed around this high-current channel of spark discharge and are powerful electromagnetic interference (PEMI) for objects of armaments and military equipment (OAME) were performed. It was shown that rise rates of HPC obtained for generator GINT-2 in the channel of long air spark discharge (of artificial lightning) and PEMI around this channel practically satisfy strict requirements of the NATO Standards AESTP-250: 2014 and USA MIL-STD-464C: 2010. Originality. The new scheme of design of CDC in composition of the modernized powerful ultra-high-voltage high-current generator of GINT-2 type (developer – Research and Design Institute «Molniya» of NTU «KhPI»), satisfying requirements of the mentioned standards for full-scale tests of OAME for EMC and immunity to action on them of PEMI from long atmospheric spark electric discharges (lightning) was developed for the first time. Practical value. Application of the created ultra-high-voltage high-current generator of GINT-2 type in tests of OAME for EMC and immunity to action on them of PEMI from artificial lightning will assist increase in reliability of OAME functioning in conditions of damaging (destabilizing) action on them HPC and PEMI of natural and artificial origin. References 19, figures 6.
Key words: **ultra-high-voltage high-current generator of voltage and current pulses, technical objects of military use, standards of tests for electromagnetic compatibility and lightning resistance.**

Запропонована і апробована нова схема побудови потужного надвисоковольтного сильнострумного генератора імпульсних напруг та струмів ГІНС-2 зовнішньої установки, що формує на активно-індуктивному навантаженні мікросекундні імпульси напруги амплітудою до ±2 МВ і струму амплітудою до ±150 кА при електричній енергії, що запасається, до 1 МДж. Даний генератор побудований на основі розміщеного в польових умовах модернізованого стаціонарного генератора ГІНС-4 на номінальну напругу ±4 МВ і номінальний струм амплітудою ±75 кА з електричною енергією, що запасається в його високовольтних конденсаторах, номінальним значенням 1 МДж. Приведені описи схемних і конструктивних вирішень генератора ГІНС-2, що дозволяють забезпечити при збереженні основної електротехнічної елементної бази генератора ГІНС-4 отримання на довгому розрядному повітряному проміжку двоелектродної системи «голка-плоскість» імпульсів струму мікросекундної тривалості з подвоєною амплітудою в порівнянні з параметрами імпульсів струму, що формуються в розрядному колі генератора ГІНС-4 з використанням аналогічної двоелектродної системи. Переведення генератора ГІНС-4 в режим роботи генератора ГІНС-2 із зменшеним удвічі рівнем вихідної імпульсної напруги і збільшеним удвічі рівнем вихідного імпульсного струму обумовлено вимогами стандартів НАТО АЕСТР-250: 2014 і США MIL-STD-464C: 2010 при випробуваннях технічних об'єктів на електромагнітну сумісність і несприйнятність до дії на них потужніх електромагнітних завад від атмосферних грозових сильнострумних електричних розрядів (блискавок). Бібл. 19, рис. 6.
Ключові слова: **надвисоковольтний сильнострумний генератор імпульсів напруги і струму, технічні об'єкти військового призначення, стандарти випробувань на електромагнітну сумісність і блискавкостійкість.**

Предложена и апробирована новая схема построения мощного сверхвысоковольтного сильноточного генератора импульсных напряжений и токов ГИНТ-2 наружной установки, формирующего на активно-индуктивной нагрузке микросекундные импульсы напряжения амплитудой до ±2 МВ и тока амплитудой до ±150 кА при запасаемой электрической энергии до 1 МДж. Данный генератор построен на основе размещенного в полевых условиях

модернизированного стационарного генератора ГИНТ-4 на номинальное напряжение ±4 МВ и номинальный ток амплитудой ±75 кА с запасаемой в его высоковольтных конденсаторах электрической энергией номинальным значением 1 МДж. Приведены описания схемных и конструктивных решений генератора ГИНТ-2, позволяющих обеспечить при сохранении основной электротехнической элементной базы генератора ГИНТ-4 получение на длинном разрядном воздушном промежутке двухэлектродной системы «игла-плоскость» импульсов тока микросекундной длительности с удвоенной амплитудой по сравнению с параметрами импульсов тока, формируемых в разрядной цепи генератора ГИНТ-4 с использованием аналогичной двухэлектродной системы. Перевод генератора ГИНТ-4 в режим работы генератора ГИНТ-2 с уменьшенным вдвое уровнем выходного импульсного напряжения и увеличенным вдвое уровнем выходного импульсного тока обусловлен требованиями стандартов НАТО AECTP-250: 2014 и США MIL-STD-464C: 2010 при испытаниях технических объектов на электромагнитную совместимость и невосприимчивость к воздействию на них мощных электромагнитных помех от атмосферных грозовых сильноточных электрических разрядов (молний). Библ. 19, рис. 6.

Ключевые слова: **сверхвысоковольтный сильноточный генератор импульсов напряжения и тока, технические объекты военного назначения, стандарты испытаний на электромагнитную совместимость и молниестойкость.**

Problem definition. In accordance with the requirements of the current Standards of the NATO AECTP-250: 2014 [1] and the USA MIL-STD-464C: 2010 [2] when testing various objects of armaments and military equipment (OAME) for electromagnetic compatibility (EMC) and resistance to direct (indirect) the action on them of powerful electromagnetic interference (PEMI) caused by atmospheric thunderstorm high-current spark electric discharges (lightning) [3-5], it is required in the area of placement on the test site of the mentioned OAME to form such high electric and magnetic fields in the surrounding airspace due to the flow of a spark channel of artificial lightning with high pulses current (HPC) which should be characterized by the rate of lightning HPC rise of the order of 10^{11} A/s with its amplitude up to (100-200) kA. The rate of increase in the strengths of the electric and magnetic fields in the near circular zone with radius r_c up to (3-10) m from the spark channel of artificial lightning should be, respectively, about 10^{11} V/(m·s) and 10^9 A/(m·s) [1, 2]. To ensure the fulfillment of such stringent requirements for the amplitude-temporal parameters (ATP) of the HPC of artificial lightning and the PEMI, appropriate powerful ultra-high-voltage high-current test electrical installations are required that can simulate in the open air near or far from the tested OAME long (1 m and more length) spark electric discharges (lightning) with HPC of the specified ATPs. The development and creation of such an ultra-high-voltage (for output pulse voltage with amplitude of 1 MV or more) high-current (for output pulse current with amplitude of 100 kA or more) test electrical equipment is associated with large financial and material and labor costs. It is known that the cost of constructing such a special test electrical equipment operating in the microsecond time range of generated on an electrical load pulses of voltage and current, is about USD 1000 per 1 kJ of electrical energy stored in its capacitive energy storage (CES) [6]. Therefore, with the energy intensity required by [1, 2] of ultra-high-voltage high-current test electrical equipment of the order of 1 MJ for its construction in Ukraine, funds are required of at least USD 1 million. In this regard, an appropriate technical solution for its developers is the appropriate modernization of the existing generators of pulse voltages and currents (GINT),

which ensures compliance with the requirements of regulatory documents [1, 2].

In the 1970s, for testing the electrical strength of the external (internal) insulation of electric power and OAME facilities for EMC and lightning resistance at the experimental testing ground of the Research and Design Institute «Molniya» of NTU «KhPI» (urban-type settlement Andreevka, Kharkiv region) a powerful generator of the GINT-4 type of stacked type was created, characterized by rated output voltage U_{ex}=±4 MV with rated electrical energy stored in its high-voltage capacitors equal to 1 MJ [7]. The insulating support structure (INS) of this generator was made on the basis of 576 porcelain support insulators of the KO-400S type, beams and braces made of wood laminated plastic of the DSPB-E-40 type, and its insulating protective (enclosing) structure is based on fiberglass pipes of the TSPO type and fiberglass roll electrical material of the REM-0,8 type [6, 7]. The scheme for constructing its charge-discharge circuit (CDC) adopted in the design of GINT-4, shown and described in [8, Fig. 12], provided a damped sinusoidal current pulse with amplitude of its first half-wave with duration of up to 11 μs no more I_{m1}≈±75 kA in a two-electrode system «needle-plane» [7, 9]. It should be noted that the CDC of the GINT-4 generator was made according to the classic bipolar Arkadiev-Marx circuit, containing 16 electrical cascades and, accordingly, 32 oppositely charged stages of it up to constant rated voltage U_C=±125 kV, separated by 16 two-electrode uncontrolled air switches made in the form of standard ball arresters (BA) with diameter of 125 mm [7]. Each stage of electrical cascades consisted of 4 high-voltage capacitors in a metal case of the type KBMG-125/1 (rated charging voltage U_C=±125 kV; electric capacitance C=1 μF) developed by the Research and Design Institute «Molniya» of NTU «KhPI». As a result, the CDC of the GINT-4 generator had 128 capacitors of the KBMG-125/1 type. In this regard, the capacity «in the discharge» C_d of this generator was about 0.125 μF, and the rated value of the electric energy stored in its capacitors W_g=0,5$C_d U_{ex}^2$ was equal to 1 MJ. In bipolar charging circuits (two for each electric polarity of the capacitors C of its CDC) of the indicated capacitors of the GINT-4 generator, single-section high-voltage charging

resistors R_C with nominal value of 500 Ω were installed in an amount of 32 (8 for each of the four charging legs of the stages of its cascades), made on the basis of nichrome wire wound on a long fiberglass pipe and filled with epoxy compound [7, 9] were installed.

The CDC of the GINT-4 generator contained 16 discharging single-section resistors R_d (8 for each of the two oppositely charged branches of the stages of its cascades) with nominal value of 110 kΩ, each of which was made on the basis of a series fixed on a rectangular getinax plate of zigzag-shaped 50 constant ceramic volume resistors of the TVO-10-2,2 kΩ type and is designed for voltage of ±500 kV [7, 9]. All stages of the GINT-4 generator in the area of their BAs were equipped with damping resistors R_{Ca} with nominal value of 0.5 Ω, made by winding nichrome wire on short fiberglass pipes and filling it with epoxy compound [7, 9]. In the discharge mode of the CDC capacitors of the GINT-4 generator to the electrical load due to nine damping resistors R_{Ca}, a total active resistance equal to $R_{C\Sigma}\approx 4.5$ Ω is connected to its discharge circuit. ATPs of voltage (current) pulses formed on an electrical load were determined by the choice in the CDC of this generator of the level and polarity of the charging voltage U_C of the steps of its electrical cascades, as well as the circuits used at its output for generating the required electrical signals. The CDC design circuit adopted in the construction of the GINT-4 generator led to the obtaining of a sufficiently high level of the specific self-inductance of this type of generator at the output of its ultra-high-voltage discharge circuit, amounting to 20 μH/MV [7, 9]. In this regard, the own inductance L_g of the discharge circuit of the generator of the GINT-4 type at $U_{ex}=\pm 4$ MV was about 80 μH [7-10]. The relatively small value of the capacitance «in the discharge» $C_d = 0.125$ μF and the relatively large value of its own inductance $L_g \approx 80$ μH of the generator of the GINT-4 type, in principle, do not allow it to fulfill the considered requirements of the NATO AECTP-250: 2014 [1] and the USA MIL-STD-464C: 2010 Standards [2] when testing OAME for EMC, the effect of PEMI on them as wells lightning resistance. From the given technical characteristics of the GINT-4 type generator, it can be seen that in relation to the requirements presented in [1, 2], its main disadvantage is the relatively low level of artificial lightning HPC (no more than $I_{m1} \approx \pm 75$ kA) formed by it on an electrical load (for example, on a long air discharge gap). In this regard, an urgent applied problem is one that is aimed at modernizing the CDC of the ultra-high-voltage generator of the GINT-4 type with the goal of real approximation with its help to the fulfillment of the basic requirements of regulatory documents [1, 2] at the Research and Design Institute «Molniya» of NTU «KhPI» when testing OAME on EMC, the impact on them of the corresponding HPC, PEMI as well as lightning resistance.

The goal of the paper is the development and testing on the basis of the existing super-high-voltage generator of the GINT-4 type of a new scheme for constructing its CDC and the creation of a modernized powerful ultra-high-voltage high-current generator of the GINT-2 type for the formation on an electrical load of microsecond voltage pulses with amplitude of up to ±2 MV and current with amplitude of up to ±150 kA with stored electrical energy in its CES up to 1 MJ.

1. Results of the development of a new CDC scheme of the modernized powerful ultra-high-voltage high-current generator GINT-2. When modernizing the CDC of the powerful ultra-high-voltage high-current generator of the GINT-4 type, our main attention was directed to increasing the capacity «in the discharge» C_d and decreasing own inductance L_g of this generator. Due to such measures, it becomes real for us to achieve the goal defined for the tested OAME by regulatory documents [1, 2]. In this case, an indispensable condition was the preservation in its CDC of the main electrical element base of the generator of the GINT-4 type.

Figure 1 shows a circuit diagram of a modernized powerful ultra-high-voltage high-current generator of the GINT-2 type, containing in its CDC, with its capacity «in the discharge» $C_d=0.5$ μF, eight electrical stages, eight uncontrolled air BAs with diameter 125 mm, one controlled BA of the trigatron type and 128 high-voltage capacitors of the KBMG-125/1 type.

In the CDC of the generator of the GINT-2 type, single-section discharge resistors R_d with nominal value of 110 kΩ (4 for each polarity of its two branches of the charge of high-voltage capacitors C of the sections of all cascades) remained the same from the CDC of the generator type GINT-4.

Figure 2 shows a general view of the GINT-2 generator.

In Fig. 1, the test object (TO) is a two-electrode discharge system «needle-plane», the length l_a of the air gap in which can vary from 1 to 4 m. It can be seen that, in contrast to the scheme for constructing the generator of the GINT-4 type, the new CDC o the generator of the GINT-2 type in each stage of its electrical cascades contains eight capacitors of the KBMG-125/1 type. With parallel charging up to voltage U_C of the corresponding polarity of these capacitors through charging resistors R_C with nominal value of 30 kΩ, the stages of all stages are galvanically interconnected by means of charging-separating resistors R_{CO} with nominal value of 180 Ω borrowed from the CDC of the GINT-4, which do not participate in the high-current discharge circuit of the generator of the GINT-2 type (see Fig. 1) [11]. In the discharge mode through air BAs F_1-F_8 with damping resistors R_{Ca} with nominal value of 0.5 Ω, the steps of all stages are connected in series with each other, which determines the capacity «in the discharge» of each stage, equal to $C_C = 4$ μF. Taking into account the fact that when the generator of the GINT-2 type is discharged on the TO, all of its eight electrical cascades are connected in a series circuit ascending to the steel shield-roof (see Fig. 1), then
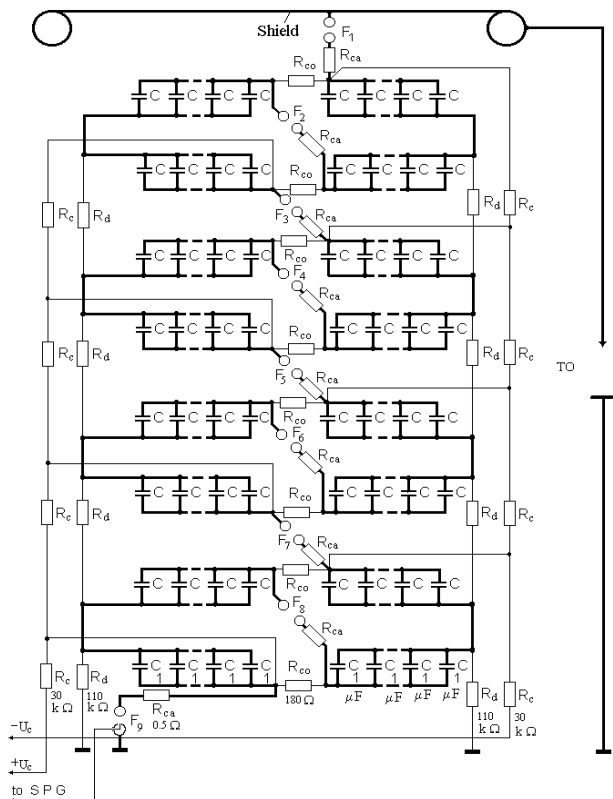
Fig. 1. Circuit diagram of the modernized powerful generator of pulse voltages and currents GINT-2 for rated voltage of ±2 MV, rated current of ±150 kA and rated electrical energy stored in its capacitors of 1 MJ, assembled on the basis of the generator of pulse voltages and currents GINT-4 for rated voltage of ±4 MV, rated current of ±75 kA and rated electrical energy stored in its CES of 1 MJ (the bold line shows a new discharge circuit of the ultra-high-voltage high-current generator)

Fig. 2. External view of the modernized powerful ultra-high-voltage high-current generator of the GINT-2 type, containing a flat steel shield-roof with slope of rectangular shape with area of 60 m^2 with round edges (in the foreground, to measure the ATPs of voltage pulses formed at the test object, an ohmic voltage divider is installed on ±2.5 MV of the ODN-2 type)

the value of the capacitance «in the discharge» C_d of such a generator becomes equal to 0.5 µF. It can be seen that the value of this capacitance of the GINT-2 generator has become four times greater than the capacitance «in the discharge» C_d of the generator of the GINT-4 type. It is important to point out that in the CDC of the generator of the GINT-4 type, the discharge circuit of its 16 electrical cascades occurred along a spiral of relatively large diameter (up to 6 m) ascending from the bottom up to the shield-roof [7, 9].

There were four electrical stages of this generator per one turn of this spiral. In the modernized CDC of the GINT-2 generator (Fig. 3), the discharge circuit of its eight electrical cascades is carried out along a linear-bifilar loop path of relatively small width (up to 3 m) ascending from the bottom up to the shield-roof. As a result of this proposed design of the new CDC, the specific own inductance of the ultra-high-voltage generator of the GINT-2 type began to be up to 10 µH/MV. At rated output voltage U_{ex}=±2 MV, the own inductance L_g of this generator decreased four times compared to the own inductance L_g≈80 µH of the generator of the GINT-4 type and began to not exceed 20 µH (with the INS height of the considered powerful generators up to 12 m [7, 9]).

Fig. 3. External view of the main elements of the modernized CDC of the generator of the GINT-2 type, which were previously electrical element base of the GINT-4 generator

For technological and technical reasons (for the possibility of using the CDC of the GINT-4 and GINT-2 generators in the future when creating an ultra-high-voltage generator of aperiodic switching voltage pulses of the standard 250 µs/2500 µs [12]), R_C charging resistors in the CDC of the GINT-2 generator were replaced with «new» two-section resistors with nominal value of 30 kΩ and length of about 1500 mm (Fig. 4).

Each section of the «new» charging resistors R_C in the CDC of the GINT-2 generator was made of 50 connected in series and zigzag connected ceramic bulk resistors TVO-5-300 Ω, placed on a flat rectangular getinax plate and filled with epoxy compound [12].

Fig. 4. General view of round cylindrical «old» (bottom) and flat rectangular «new» (top) charging resistors R_C, respectively, with nominal value of 500 Ω and 30 kΩ, which are part of the CDC, respectively, of powerful ultra-high-voltage generators of the GINT-4 type and GINT-2 type

We point out that when the CDC capacitors C of the GINT-2 type generator (see Fig. 1) reaches the specified level of charging voltage $\pm U_C$ from the starting pulse generator (SPG), a triggering microsecond voltage pulse with amplitude of ± 10 kV (the polarity of this pulse is determined by the polarity of the charge of the first electrical section of the generator stage from the ground) is fed to the trigatron-type controlled air arrester F_9 [13]. After the actuation of the controlled BA F_9 with diameter of 125 mm due to the sequential occurrence of overvoltages in the discharge circuit of the CDC of the GINT-2 generator, the air BAs F_1–F_8 of all stages are triggered along its height, which leads to the formation of the required voltage and current pulses on the TO. The polarity of the output voltage pulse U_{ex} of the GINT-2 generator will be of the opposite polarity of the charge of its first section of the electric cascade from the ground, connected directly to the BA F_9.

2. Results of calculation and experimental testing of the new CDC circuit of the powerful ultra-high-voltage high-current generator GINT-2.

According to the laws of theoretical electrical engineering, it is known that in the *RLC*-circuit as applied to the CDC of the modernized generator of the GINT-2 type, which is characterized by a halved level of the rated output voltage U_{ex} (up to ± 2 MV) and a fourfold reduced own inductance L_g (up to 20 μH) compared with the CDC of the generator of the GINT-4 type [7], provided $R_{C\Sigma} < 2(L_g/C_d)^{1/2}$, the amplitude I_{m1} of the sinusoidal discharge current at its output will be directly proportional to the value $(C_d)^{1/2}$ [14]. Since the capacity «in the discharge» C_d of the generator of the GINT-2 type has become four times higher than the corresponding capacitance C_d of the generator of the GINT-4 type, the considered amplitude I_{m1} of the rated discharge current at the output of the CDC of the modernized generator of the GINT-2 type should double with the corresponding amplitude $I_{m1} \approx \pm 75$ kA of the current [7, 9] in the discharge circuit of the generator of the GINT-4 type and amount to approximately ± 150 kA. A characteristic feature of the CDC of the modernized generator of the GINT-2 type is that the period T_g of oscillations of the discharge current in it in accordance with Thomson formula $T_g \approx 2\pi (L_g C_d)^{1/2} \approx 21$ μs [14] remains practically unchanged in comparison with the value of T_g in the CDC of the generator of the GINT-4 type.

The calculation estimate of the maximum value of the rate of rise of the discharge current i_C in the CDC of the modernized generator of the GINT-2 type with TO in the form of an air «needle-plane» system can be performed according to the following approximate relation:

$$di_C / dt \approx 2\pi T_g^{-1} I_{m1}. \qquad (1)$$

At $T_g \approx 21$ μs and $I_{m1} \approx 150$ kA, according to (1), the sought-for calculation value of the maximum rate of rise of the sinusoidal discharge current i_C in the CDC of the GINT-2 generator will be about $0.45 \cdot 10^{11}$ A/s. It can be seen that the obtained numerical value of di_C/dt approaches the requirements of regulatory documents [1, 2]. The calculation value of the maximum rate of rise in the air of the magnetic field strength H_C around the zone of flow of the high-current discharge channel from the GINT-2 generator with TO in the form of a «needle-plane» discharge system, taking into account the law of total current, can be determined by the following approximate formula:

$$dH_C / dt \approx (2\pi r_c)^{-1} di_C / dt \approx r_c^{-1} T_g^{-1} I_{m1}. \qquad (2)$$

From (2) at $r_c \approx 4.46$ m, $T_g \approx 21$ μs and $I_{m1} \approx 150$ kA it follows that the numerical value of dH_C/dt turns out to be approximately equal to $1{,}6 \cdot 10^9$ A/(m·s). The obtained dH_C/dt value fully meets the requirements from [1, 2].

As for the calculation estimate of the maximum rate of rise in the air of the electric field strength E_C around the cylindrical zone of the long spark discharge channel from the GINT-2 ultra-high-voltage generator with TO in the form of a standard «needle-plane» air discharge system, on the one hand, it can be estimated by the following approximate expression:

$$dE_C / dt \approx U_{CU} /(T_C l_a), \qquad (3)$$

where U_{CU} is the cutoff voltage for the output pulse U_{ex} in the discharge circuit of the GINT-2 generator with the specified TO in the form of a «needle-plane» system; T_C is the pre-discharge time in the «needle-plane» system; l_a is the length of the air gap in the «needle-plane» system.

We point out that the parameters U_{CU} and T_C included in (3) must be determined in accordance with the requirements of the current interstate standard GOST 1516.2-97 [15]. With the experimental data obtained for the high-current circuit of the ultra-high-voltage generator of the GINT-2 type with the considered discharge system «needle-plane» having numerical values $U_{CU} \approx 1180$ kV, $T_C \approx 1.7$ μs and $l_a = 2$ m, from (3) we obtain that in this case, the sought value of dE_C/dt takes on a numerical value equal to about $3.47 \cdot 10^{11}$ V/(m·s). It is seen that the obtained calculated value of dE_C/dt approaches the value required by [1, 2].

Figure 5 shows a typical oscillogram of a microsecond voltage pulse $U_{ex}(t)$ obtained in the high-current discharge circuit of this generator ($U_C = \pm 100$ kV) during an electric breakdown at the TO of a long air gap

(l_a=2 m) in the «needle-plane» discharge system for the case of experimental testing of the new CDC of the modernized powerful generator of the GINT-2 type. It is seen that the spark breakdown of this air gap occurs on the growing part of the ultra-high voltage pulse formed and applied to it. In this case, the pulsed cutoff voltage U_{CU} is ~1180 kV, and the pre-discharge time T_C is about 1.7 μs.

On the other hand, taking into account the classical electrodynamic ratio in air between the strengths of the electric E_C and magnetic H_C fields in the electromagnetic wave formed for testing the OAME ($E_C/H_C \approx 377$ Ω in the far circular zone from the source of electromagnetic radiation [6]) for the dE_C/dt value at the front of the first half-wave of the E_C-field strength in the near air circular zone with radius of $r_c \leq 10$ m from the spark discharge channel of artificial lightning in the considered high-current discharge circuit of the generator of the GINT-2 type, the following approximate expression can be written:

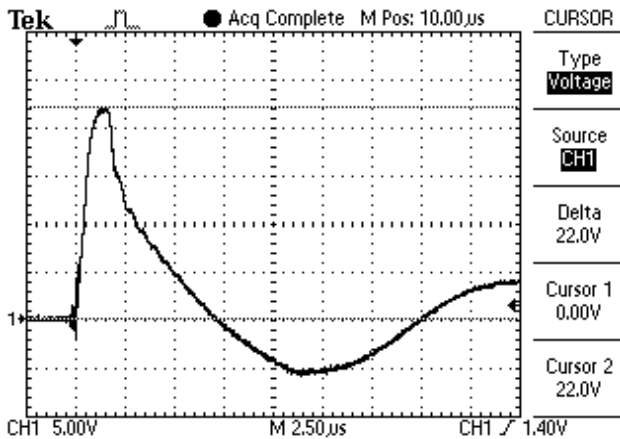$$dE_C / dt \approx 377 dH_C / dt . \qquad (4)$$

Fig. 5. Oscillogram of the voltage pulse cut off on the rising part applied to a long air gap (l_a=2 m) connected to the high-current circuit of the ultra-high-voltage generator GINT-2 of the two-electrode discharge system «needle-plane»
(U_C=±100 kV; $U_{CU} \approx$1180 kV; $T_C \approx$1.7 μs; vertical scale – 268.2 kV/cell; horizontal scale – 2.5 μs/cell)

The possibility of using formula (4) in the carried out approximate calculation estimate of the value of dE_C/dt is indicated by the fact that the distance from the center of the spark discharge channel of the simulated lightning, to which the first half-wave of the E_C-field strength propagates through the air with an electric breakdown of an air gap of length $l_a \leq$(1-4) m in a two-electrode system «needle-plane» for $T_C \leq$2 μs (see Fig. 5), numerically does not exceed 600 m. Such an approach in the calculation estimation of dE_C/dt does not contradict the requirements of the above documents [1, 2]. In addition, a similar approach is used to assess the ATPs of formed in the near air zones of artificially generated high-power electromagnetic pulses (EMPs) simulators (for example, micro- and nanosecond EMPs of nuclear explosions) [16].

Then from (4) at $dH_C/dt \approx 1.6 \cdot 10^9$ A/(m·s), obtained above from (2) at $r_c \approx 4.46$ m for the case under consideration ($T_g \approx 21$ μs; $I_{m1} \approx 150$ kA) , it follows that dE_C/dt can take a numerical value equal to approximately $6.03 \cdot 10^{11}$ V/(m·s). This slew rate for dE_C/dt practically meets the requirements set out in the normative documents [1, 2].

Figure 6 shows a typical oscillogram of the damped sinusoidal discharge current $i_C(t)$ ($T_g \approx 21$ μs) in the CDC of the generator of the GINT-2 type with an electrical breakdown of an air gap of length l_a=1 m in the «needle-plane» discharge system. From the data in Fig. 6 it follows that when the charging voltage U_C of capacitors in the CDC of the GINT-2 generator increases to the rated level and equal to ±125 kV, it becomes possible to obtain current pulses in the air discharge system «needle-plane» with the amplitude of the first half-wave equal to $I_{m1} \approx \pm$ 150 kA.
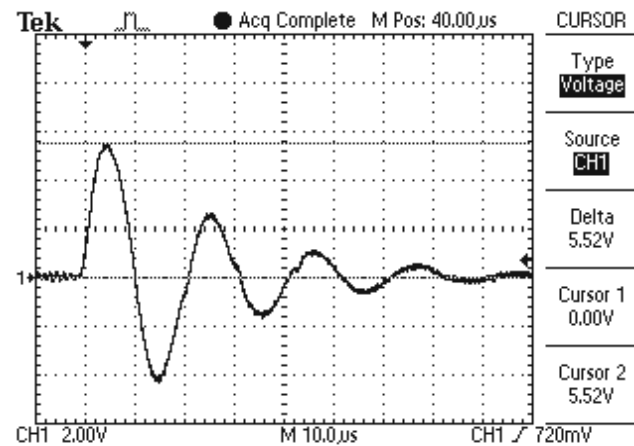
Fig. 6. Oscillogram of the pulsed current in the discharge high-current circuit of the ultra-high-voltage generator of the GINT-2 type with an electrical breakdown of an air gap of length l_a=1 m in the «needle-plane» discharge system
(U_C=±50 kV; $I_{m1} \approx$62.1 kA; $T_g \approx$21 μs; vertical scale – 22.52 kA/cell; horizontal scale – 10 μs/cell)

When measuring the ATPs of voltage pulses formed in the discharge circuit of the GINT-2 generator (see Fig. 5), an ultra-high-voltage ohmic divider of pulsed voltage for ±2.5 MV type ODN-2 (see Fig. 2) with a division coefficient $K_d \approx 53.65 \cdot 10^3$ [17] matched in the measuring circuit was used. From ODN-2 a shielded cable communication line with length of up to 60 m was coordinatedly connected to a Tektronix TDS 1012 digital storage oscilloscope, placed to reduce electromagnetic interference in its working channel and to increase the measurement accuracy of these ATPs far from the generator of the GINT-2 and the TO type in a buried shielded measuring bunker.

When registering the ATPs of the discharge current pulses i_C in the CDC of the GINT-2 generator, a coaxial shunt of the ShK-300 type [18] verified by the State Metrological Service with a shielded cable communication line up to 70 m in length, having a conversion coefficient

numerically equal to $K_S \approx 11.26 \cdot 10^3$ A/V and coordinatedly connected to the measuring path with a Tektronix TDS 1012 digital storage oscilloscope, placed to reduce the parasitic influence of external PEMI on it far from the test site in a buried shielded measuring bunker [19].

Taking into account the absence in the open literature of data on ultra-high-voltage test installations of NATO countries that implement the requirements of the above Standards [1, 2], we can conclude that, in terms of their technical characteristics (ATPs of voltage, current and PEMI pulses generated at the TO, the level of electric energy storage in its CES and a relatively low cost of development and construction), an ultra-high-voltage generator of the GINT-2 type meets the high world requirements in the field of high-voltage pulse technology.

Conclusions.

A powerful ultra-high-voltage high-current generator of pulsed voltages and currents of the GINT-2 type, developed and created at the Research and Design Institute «Molniya» of NTU «KhPI» which forms microsecond voltage pulses with amplitude of up to ±2 MV and current with amplitude of up to ±150 kA with electric energy stored in its high-voltage capacitors up to 1 MJ on an active-inductive electrical load made in the form of a standard two-electrode air discharge system «needle-plane» allows, in accordance with the requirements of the current Standards of the NATO AECTP-250: 2014 and the USA MIL-STD-464C: 2010 to carry out full-scale tests of weapons and military equipment for electromagnetic compatibility and resistance to direct (indirect) impact on them of HPC and powerful electromagnetic interference caused by atmospheric lightning spark discharges (lightning).

Note.

REFERENCES

1. AECTP-250: 2014. NATO Standard Electrical and Electromagnetic Environmental Conditions. Edition C Version 1, December 2014, NSO Publ. − 253 p.
2. MIL-STD-464C: 2010. Department of defense. Interface standard. Electromagnetic Environmental Effects Requirements for Systems. USA, 2010. − 165 p.

3. Uman M.A. Natural and artificially-initiated lightning and lightning test standards. *Proceedings of the IEEE*, 1988, vol. 76, no. 12, pp. 1548-1565. **doi: 10.1109/5.16349.**
4. Dyakov A.F., Kuzhekin I.P., Maksimov B.K., Electromagnetic compatibility and lightning protection in the power. Moscow, MEI Publishing House, 2009. 455 p. (Rus).
5. Kravchenko V.I. Lightning. Electromagnetic factors and their impact on the striking technical objects. Kharkov, NTMT Publ., 2010. 292 p. (Rus).
6. Knopfel' G. Ultra strong pulsed magnetic fields. Moscow, Mir Publ., 1972. 391 p. (Rus).
7. Pekar' I.R., Fertik S.M. The powerful high-voltage electric-discharge setting on 4 MV and 1 MJ. *Lecture collection of interinstitute conference «Electrophysics apparatus and electric isolation»*. Moscow, Energiya Publ., 1970, pp. 22-26. (Rus).
8. Baranov M.I., Buriakovskyi S.G., Kniaziev V.V., Rudenko S.S. Analysis of characteristics and possibilities of high-voltage electrical engineering complex Scientific-&-Research Planning-&-Design Institute «Molniya» of NTU «KhPI» for the tests of objects of energy, armament, aviation and space-rocket technique on electric safety and electromagnetic compatibility. *Electrical engineering & electromechanics*, 2020, no. 4, pp. 37-53. **doi: 10.20998/2074-272X.2020.4.06**.
9. Baranov M.I. Selected topics of Electrophysics. Monograph in 4 Vols. Vol. 3. Theory and practice of electrophysics tasks. Kharkiv, Tochka Publ., 2014. 400 p. (Rus).
10. Baranov M.I., Bocharov V.A., Ignatenko N.N., Kolobovskyi A.K. The powerful generators of impulsive voltage and currents of maximum parameters for testing of power electroenergy equipment. *Electrical engineering & electromechanics*, 2003, no. 2, pp. 75-80. (Rus).
11. Baranov M.I. The comparative analysis of work of two charts of construction of generators of high-voltage incendiary impulses of voltage of powerful electrophysics options. *Bulletin of NTU «KhPI». Series: Technique and electrophysics of high voltage*, 2006, no. 37, pp. 100-107. (Rus).
12. Baranov M.I., Koliushko G.M., Kravchenko V.I. A switching aperiodic superhigh-voltage pulse generator for testing the electric strength of insulation of technical objects. *Instruments and Experimental Technique*, 2013, vol. 56, no. 6, pp. 653-658. **doi: 10.1134/s0020441213050126.**
13. Dashuk P.N., Zayents S.L., Komel'kov V.S., Kuchinskyi G.S., Nikolayevskaya N.N., Shkuropat P.I., Shneerson G.A. The technique of large pulsed currents and magnetic fields. Moscow, Atomizdat Publ., 1970. 472 p. (Rus).
14. Neyman L.R., Demirchyan K.S. Theoretical bases of the Electrical Engineering. In 2 vols. Vol.2. Leningrad, Energoizdat Publ., 1981. 416 p. (Rus).
15. GOST 1516.2-97. Electrical equipment and installations for AC voltages 3 kV and higher. General methods of dielectric tests. Minsk, Publishing house of standards, 1998. 31 p. (Rus).
16. Ricketts L.U., Bridges J.E., Mayletta J. Electromagnetic pulse and methods of protection. Moscow, Atomizdat Publ., 1979. 328 p. (Rus).
17. Baranov M.I., Koliushko G.M., Kravchenko V.I. Generation of standard switching aperiodic impulses of high and superhigh voltage for full-scale tests of electrical power objects. *Electrical engineering & electromechanics,* 2013, no. 2, pp. 52-56. (Rus).

18. Baranov M.I., Koliushko G.M., Kravchenko V.I., Nedzel'skii O.S., Dnyshchenko V.N. A Current Generator of the Artificial Lightning for Full-Scale Tests of Engineering Objects. *Instruments and Experimental Technique*, 2008, no.3, pp. 401-405. **doi: 10.1134/s0020441208030123.**

19. Baranov M.I., Buriakovskyi S.G., Rudakov S.V. The tooling in Ukraine of model tests of objects of energy, aviation and space-rocket engineering on resistibility to action of pulsed current of artificial lightning. *Electrical engineering & electromechanics*, 2018, no. 4, pp. 45-53. **doi: 10.20998/2074-272X.2018.4.08**.

M.I. Baranov[1], *Doctor of Technical Science, Professor,*
S.G. Buriakovskyi[1], *Doctor of Technical Science, Professor,*
V.V. Kniaziev[1]*, Candidate of Technical Science, Leader Research Scientist,*
[1] Research and Design Institute «Molniya»
of National Technical University
«Kharkiv Polytechnic Institute»,
47, Shevchenko Str., Kharkiv, 61013, Ukraine,
e-mail: baranovmi@kpi.kharkov.ua, sergbyr@i.ua, knyaz2@i.ua

V.A. Yarovenko, P.S. Chernikov, E.I. Zaritskaya, A.N. Schumylo

CONTROL OF ELECTRIC SHIPS' PROPULSION MOTORS WHEN MOVING ON CURVILINEAR TRAJECTORY

Purpose. The aim of the work is to search for the optimal control of the electric ships' propeller motors (PM) while moving on curvilinear trajectory. The indices characterizing the vessel were selected as the criteria of optimality. Methodology. Optimal control laws of PM providing electric ships' best maneuverability can be found by joint consideration of the electric propelling plant (EPP), propellers and hull. Results. A method of calculating the transient regimes of the electric ships' propulsion complexes during maneuver has been developed. A new method of forming the PM control laws is proposed. The nature of the target functions is revealed and a method of optimizing the parameters of control signals is developed. Optimization calculations have been carried out and the optimal control of the electric ships' propeller motors when moving along curvilinear trajectory has been found. Optimization has been carried out by the criterion of minimum energy consumption and by the criterion of minimum ship's distance. The optimization efficiency is illustrated. Scientific novelty. The method of searching for the optimal control laws is constructed according to the system principle, which allows optimizing the control of the propulsion motors by the final result. Practical value. The proposed recommendations can be used in the design of electric propelling plants and in their operation.
References 10, tables 3, figures 6.
Key words: **electric ships' propulsion motors, control on maneuvers, optimal control during curvilinear motion, optimization method.**

Метою роботи є пошук оптимального управління гребними електродвигунами (ГЕД) електроходів при русі по криволінійній траєкторії. В якості критеріїв оптимальності обрані показники, що характеризують судно. Методика. Оптимальні закони управління ГЕД, щоб забезпечити найкращі маневрені характеристики електроходів, можуть бути знайдені при спільному розгляді гребної електроенергетичної установки, гребних гвинтів і корпусу судна. Результати. Розроблено метод розрахунку перехідних режимів пропульсивних комплексів електроходів при маневруванні на криволінійній траєкторії. Запропоновано новий спосіб формування законів управління ГЕД. Виявлено характер цільових функцій і розроблений метод оптимізації параметрів сигналів управління. Проведено оптимізаційні розрахунки і знайдено оптимальне управління гребними електродвигунами електроходів при русі по криволінійній траєкторії. Оптимізація проведена за критерієм мінімуму витрат енергії і за критерієм мінімуму вибігу судна. Проілюстрована ефективність оптимізації. Наукова новизна. Метод пошуку оптимальних законів управління побудований за системним принципом, що дозволяє оптимізувати управління гребними електродвигунами за кінцевим результатом. Практична значимість. Запропоновані рекомендації можуть використовуватися і при проектуванні гребних електроенергетичних установок і при їх експлуатації. Бібл. 10, табл. 3, рис. 6.
Ключові слова: **гребні електродвигуни електроходів, управління на маневрах, оптимальне управління при криволінійному русі, метод оптимізації.**

Целью работы является поиск оптимального управления гребными электродвигателями (ГЭД) электроходов при движении по криволинейной траектории. В качестве критериев оптимальности выбраны показатели, характеризующие судно. Методика. Оптимальные законы управления ГЭД, обеспечивающие наилучшие маневренные характеристики электроходов, могут быть найдены при совместном рассмотрении гребной электроэнергетической установки, гребных винтов и корпуса судна. Результаты. Разработан метод расчета переходных режимов пропульсивных комплексов электроходов при маневрировании на криволинейной траектории. Предложен новый способ формирования законов управления ГЭД. Выявлен характер целевых функций и разработан метод оптимизации параметров сигналов управления. Проведены оптимизационные расчеты и найдено оптимальное управление гребными электродвигателями электроходов при движении по криволинейной траектории. Оптимизация проведена по критерию минимума расхода энергии и по критерию минимума выбега судна. Проиллюстрирована эффективность оптимизации. Научная новизна. Метод поиска оптимальных законов управления построен по системному принципу, что позволяет оптимизировать управление гребными электродвигателями по конечному результату. Практическая значимость. Предложенные рекомендации могут использоваться и при проектировании гребных электроэнергетических установок и при их эксплуатации. Библ. 10, табл. 3, рис. 6.
Ключевые слова: **гребные электродвигатели электроходов, управление на маневрах, оптимальное управление при криволинейном движении, метод оптимизации.**

Introduction. The presence in electric ships, in addition to the steering gear, of several powerful, dynamic and overload-resistant propulsion electric motors (PM) allows to achieve high maneuverability of these ships. With the joint maneuvering of the rudder and propellers, the ship's turnability improves, the degree of safety of maneuvering operations increases [1]. At the same time, this significantly changes the load on the propulsion motors and on the entire propulsion power plant as a whole.

The curvilinear trajectory of the ship's movement, its yaw, the change in the conditions of interaction of propellers, rudder and ship's hull significantly affects the forces and moments of forces acting on the ship's hull during its curvilinear unsteady motion [2, 3]. The forces and moments developed by the propellers are subject to an even greater change – the useful stop and the moment of resistance of the water to the rotation of the propeller and, accordingly, the moment of resistance to the

propeller motor. Their values change as a result of the changing bevel angle of the water flow and changes in the speed of the vessel. Thrust, drag moment and lateral force values for inner and outer propellers (in relation to the center of circulation) differ significantly from each other [4].

In Fig. 1, plans for the speeds of two propellers are built for the curvilinear movement of the vessel, where: v is the linear speed of movement of the center of gravity of the vessel; β is the drift angle; α_{BevL} and α_{BevR} are the bevel angles of the water flow incident on the left and right propellers, respectively; u_L and u_R are the transverse components of the speed of movement of the left and right propellers; v_L and v_R are the speeds of the left and right propellers.
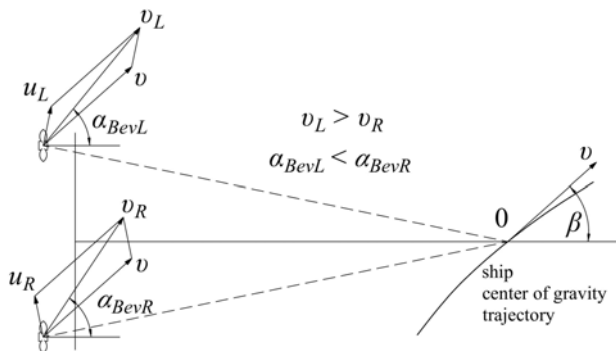

Fig. 1. Propeller speed plan for curvilinear movement

Figure 1 shows that the inner propeller operates in a flow with a larger bevel angle, and the outer one – with a smaller one. This affects the dynamic characteristics of the propellers and the moment of resistance to the external and internal PM. The loads on them turn out to be different, which can lead to the activation of the protection systems of the more loaded propeller motor and, ultimately, to the failure to perform the maneuver.

All this must be taken into account when generating control signals for propulsion motors. They must be such as to ensure, on the one hand, the best controllability of the electric ship, and on the other hand, the operation of all components of the propulsion electric propelling plant (EPP) in permissible modes.

The state of the issue under study. The control of the frequency-controlled propulsion motors of the EPP of the electric ship is carried out by generating two signals [5-7]:

- relative frequency of the supply voltage

$$\alpha = \frac{f}{f_N} ; \qquad (1)$$

- relative supply voltage

$$\gamma = \frac{U}{U_N} . \qquad (2)$$

The relationship between the relative voltage γ and the relative frequency α is called the frequency control law. In [8, 9], it is shown that for frequency-controlled propeller motors, the classical (proportional) control law is not effective, since it was obtained in relation to the

performance indicators of electric motors. In propelling electric power plants for control of propulsion electric motors during maneuvers, it is necessary to have such laws that will ensure the best maneuvering properties of electric ships. The performance indicators of the EPP, in this case, should not go beyond the permissible limits.

In [8], an approach to solving the problems of finding optimal control laws for propeller electric motors is described. A method for generating control signals based on a systemic principle is proposed. The procedure for optimization calculations has been developed. The optimal parameters of the control laws are found for maneuvering on a straight course. The efficiency of the transition to the recommended control laws is illustrated by a comparative analysis of the results of performing maneuverable operations with control according to classical laws and according to the found optimal relations between γ and α.

A change in the nature of maneuver, simultaneous control of both the propulsion electric motors and the rudder, the need to take into account both the maneuverability indicators of the electric ship and the performance indicators of the propulsion electric power plant will undoubtedly affect the laws of frequency control.

The goal of this research is the search for the optimal laws of control of the propelling electric motors of electric ships moving along a curvilinear trajectory, with joint maneuvering of the PM and the rudder.

Method for solving the problem. To achieve the goal, it is necessary to develop a mathematical model of the transient modes of operation of the propulsive complex of an electric ship when moving along a curvilinear trajectory, to form an objective function and to find the optimal laws of control of the PM during maneuvers.

An enlarged block diagram of one power circuit of the propulsive complex of an electric ship without taking into account the mutual connections is shown in Fig. 2.

Each of its «power» circuits includes: heat engine – D, synchronous generator – G, frequency converter of electricity – SE, induction propeller motor – M, heat engine speed regulator – DR, synchronous generator voltage regulator – GE, propeller - P. The propulsion system also includes rudder – R and ship's hull. The main parameters of the complex, control signals and feedback signals: ω_D and P_D – angular speed of rotation and power of heat engines; U_G and I_G – voltage and current at the generator output; U_M and I_M – voltage and current of propelling motors; M_M and ω_M – torque and angular velocity of rotation of PM (and propellers).

On the basis of the block diagram, a mathematical model and codes for calculating transient modes of operation of the propulsion complex during maneuvers were developed [10]. Generalized dimensionless parameters of the complex are found. Changes in the values of these parameters determine the behaviour of electric ships and affect the numerical values of the quality indicators of maneuvering.
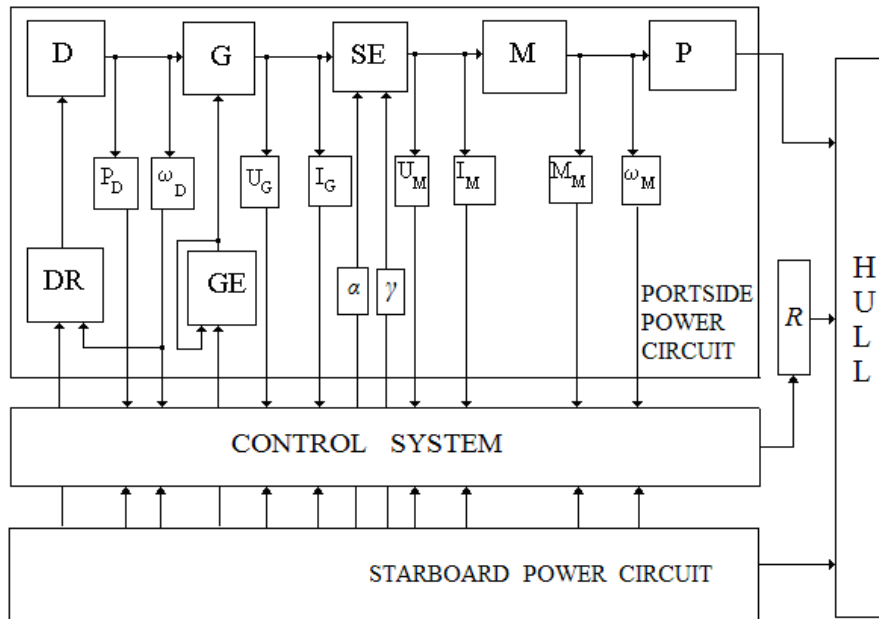
Fig. 2. Block diagram of one power circuit of the propulsive complex of the electric ship

As an example, in Fig. 3, the results of calculations of the current values of the main operating parameters of the components of the propulsion complex are shown when the electric ship is performing the maneuver «acceleration of the propulsion power plant – the ship's exit to a curvilinear trajectory (circulation)».

Results are given in relative time

$$T = v_0 t / L, \qquad (3)$$

where: v_0 is the ship's speed in the steady-state (basic) mode; L is the length of the vessel; t is the current time.
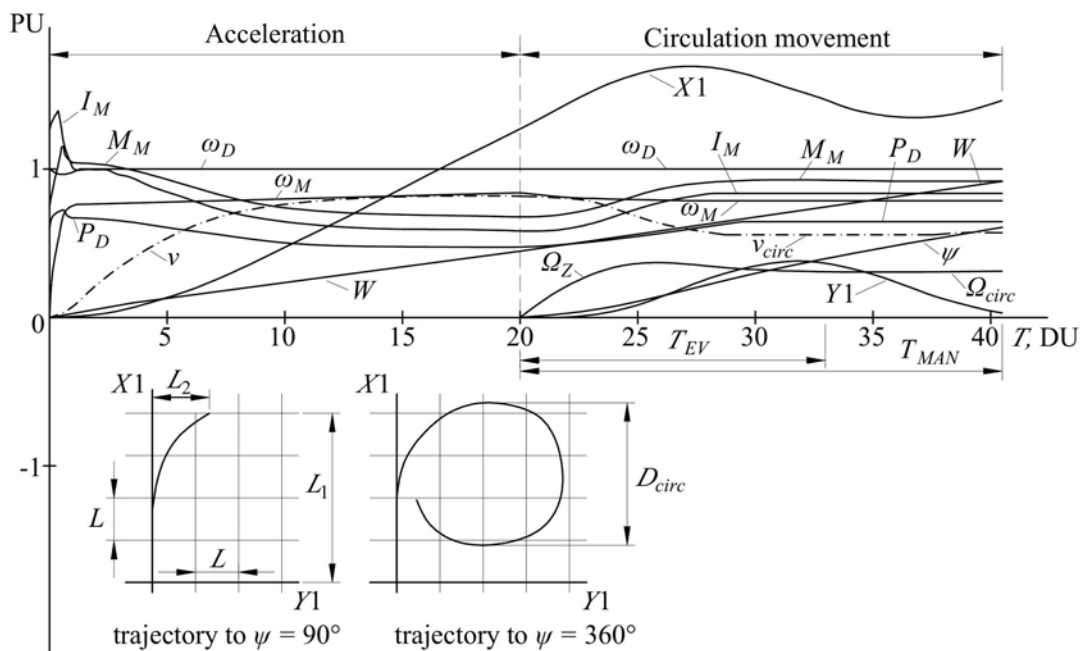
Fig. 3. The current values of the main performance indicators when performing the maneuver «acceleration of the EPP – exit to circulation»

Figure 3 shows the relative values of the operating parameters of the internal, most loaded, power circuit: heat engine (ω_D, P_D); propelling motor (I_M, M_M, ω_M). The current values are also given for: energy consumption (W); speed of movement of the vessel (v) and its course (ψ); the path traveled by the electric ship ($X1$ and $Y1$) in a coordinate system independent of the vessel, and the

angular velocity (Ω_Z) of its rotation around the vertical axis passing through the center of gravity of the vessel.

In the initial state, the vessel is stationary, the generating sets are idling. Acceleration begins with an increase in the relative values of α and γ of the voltage supplying the electric motors. PMs begin to accelerate. The torque M_M increases, and the rotational speeds of the

motors and propellers ω_M increase accordingly. The thrust of the propellers increases, and the electric ship begins to accelerate (its speed v increases). With an increase in the engine speed ω_M and the vessel's speed v, the propeller drag moment M_P increases. As the supply voltage rises, the current I_M and the torque M_M of the electric motor increase. The load on the heat engine increases. Its power P_D increases, and the rotational speed ω_D, accordingly, slightly decreases. The energy consumption W is increasing. The distance traveled by the ship increases. Gradually, after 12-13 relative units of time (in the described maneuver), the transient process ends, and the propulsive complex enters the operating mode close to the steady state. The distance traveled by the electric ship during the maneuver is described by the $X1$ curve.

From the moment $T = 20$ relative time units, the process of the ship entering a curvilinear trajectory begins. The loads on the propulsion motors and on the heat engines of the generating sets increase (I_M, M_M, P_D increase, ω_M decreases). The electric ship goes into circulation. The angular velocity Ω_Z and the lateral displacement $Y1$ appear. The vessel's speed v decreases. At approximately $T = 33$ relative time units, the evolutionary period of the circulation movement ends and its quasi-steady period begins. The electric ship reaches the steady-state values of the speed of movement v_{circ} and the angular speed of rotation (circulation) Ω_{circ}. The maneuver ends when the ship reaches the course $\psi = 360°$ (full circulation). The total duration of the considered maneuver is $T = 40.5$ relative time units. The trajectory of the electric ship's center of gravity is shown in Fig. 3.

The change in the current values of the performance indicators clearly demonstrates the nature of the course of transient processes. However, to assess the maneuvering characteristics of the complex, separate indicators of the quality of maneuvering operations are needed, which make it possible to assess the behaviour of both the components of the propelling electric power plant and the electric ship as a whole. These are: speed fluctuations and power fluctuations of heat engines; maximum values of currents and torques of synchronous generators and propelling motors in transient modes; indicators characterizing the stability of the parameters of the electricity of the ship's electrical network; inertial characteristics of the vessel; energy consumption (fuel consumption) for performing maneuvers. The mathematical model and the calculation method [10] allow to do this.

At electric ships, control of each power circuit of the propulsion electric power plant (control of each PM) is carried out independently of the others. Control signals are supplied to each propelling motor (by shifting the control post handles) – by the frequency of rotation of the PM (determined by the relative frequency of the current α) and by voltage (determined by the value of γ). The control of the electric ship, when entering a curvilinear trajectory, is carried out by shifting the rudder blade to the starboard side, while simultaneously braking the right propelling motor. With such maneuvering, the angles of the bevel of the flow of water running on the outer and inner (relative to the center of circulation) propellers change significantly (Fig. 1). Their hydrodynamic

characteristics change. The moments of resistance on the shaft of the propelling motors of the outer and inner circuits are different.

With such a maneuver, the relative frequency of the current α_L for the left PM is constant throughout the entire maneuver. For the right PM, the frequency α_R decreases with the beginning of maneuvering (in accordance with the new position of the control post handle) and remains unchanged until the end of the maneuver. The difference between α_L and α_R will be called the degree of braking of the propelling motor (propeller).

As noted above, the classical law of frequency control does not allow achieving high maneuverability of electric ships. With a systematic approach to the optimal control of the PM, it becomes necessary to search for such control signals that will provide the best values for the quality indicators of the maneuvering of electric ships. Here, it is imperative to monitor the performance of all components of the propulsion electric power plant, and first of all, the propulsion electric motors and drive motors of generator sets.

In [8], it was proposed to form control signals in the form:

$$\alpha = \alpha_{prim} + k_1(1 - \exp(-k_5 T)), \qquad (4)$$
$$\gamma = k_2\alpha + k_3\alpha^2 + k_4\alpha^3 + (1 - k_2 - k_3 - k_4)\alpha^4, \qquad (5)$$

where: α_{prim} is the initial value of the relative frequency of the supply voltage of the PM; k_2, k_3, k_4 are the parameters of control signals that are being optimized.

For the considered maneuver, it makes no sense to optimize the dependence $\alpha = \alpha(T)$, since α is fixed and is determined by a given (by the control post handle) speed of the PM. Optimization will concern only the search for optimal parameters of the control law γ / α.

According to this goal, either the minimum energy consumption for the execution of the maneuver – $W_{C\min}$, or the minimum run-out of the electric ship – $L_{1\min}$ are taken as optimality criteria. The first criterion characterizes the economic indicators of maneuvering, the second one – the safety of maneuvering operations.

In accordance with the task, it is necessary to minimize the objective function

$$W(\boldsymbol{k}) \to \min, k \in \boldsymbol{k}^n, \qquad (6)$$

or

$$L_1(\boldsymbol{k}) \to \min, k \in \boldsymbol{k}^n, \qquad (7)$$

where $\boldsymbol{k} = [k_2, k_3, k_4]$ are the parameters to be optimized; $\boldsymbol{k}^n$ is the admissible region of the n-dimensional space. Linear constraints p in the form of inequalities $g_j(\boldsymbol{k}) \geq 0$, $j = 1, 2,..., p$ are determined by the tolerances for the ranges of changes in the EPP performance indicators and other conditions for performing maneuvers.

In [8], a method for finding optimal solutions to such problems is described. It was developed based on the peculiarities of the object under consideration and the complex topography of the target functions revealed during the research. In the process of optimization, the calculations of the current values of all operating parameters of the complex are carried out during the execution of the corresponding maneuvers by the electric ship and, based on their results, the energy consumption for the execution of the maneuver and the run of the electric ship are determined.

Results of work. Below are the results of optimization of the parameters of the frequency control law. The search for optimal parameters was carried out for one of the typical (described above) maneuvers of electric ships – acceleration and entry into circulation. Optimization was carried out according to the $W_{C\min}$ and $L_{1\min}$ criteria.

When generating control signals to propulsion motors, it is necessary, as noted above, to ensure the operation of the propulsion electric power plant in permissible modes. From Fig. 1 it can be seen that the internal propeller operates in a flow with a larger bevel angle. The load on its propeller motor turns out to be significantly greater than the load on the external PM. The possible actuation of the protection systems of the «internal» power circuit can lead to a failure to perform a maneuver or even to an emergency. Based on this, when searching for the optimal parameters of control signals, first of all, it is necessary to control the performance indicators of the internal power contour.

The nature of the maneuvering operations performed by the electric ships, and, accordingly, the fuel consumption and run-out of the electric ship, are influenced by the design parameters of the ship, and the parameters of the electric power plant and external conditions. The degree of influence of each parameter is different. When looking for optimal propulsion motor control, it is very important to cover as many electric ships as possible. In other words, the recommendations should be valid for a wide class of ships.

In the process of developing a mathematical model of transient modes (in relative units), criteria for dynamic similarity (generalized dimensionless parameters of propulsion complexes) were identified; the ranges of change of their values are found, covering all electric ships with frequency-controlled PM (with a traditional propeller drive).

As shown by preliminary studies (screening experiments), the following parameters have the most significant influence on the selected criteria, when maneuvering by the rudder and propeller motors together: the degree of braking; v_{prim} – the initial speed of the vessel; β_R – the rudder blade shift angle; generalized dimensionless parameter of the complex N_X – power-to-weight ratio of the electric ship

$$N_X = \frac{L \sum K_{Pj} P_{ej0}}{(m + \lambda_{11}) v_0^2}, \qquad (8)$$

where P_{ej0} and K_{Pj} are the effective stop of the propeller in the steady state and its share in the total stop, respectively; m and λ_{11} are the mass of the vessel and the masses of water attached to it (along the longitudinal axis X).

For various ratios between these parameters (in fact, for various electric ships), optimization calculations were carried out and optimal solutions were obtained. As an example, in Table 1 (according to the criterion of minimum energy consumption $W_{C\min}$) and in Table 2 (according to the criterion of minimum ship run-out $L_{1\min}$) some of their results are given. These are the optimal parameters of the frequency control law γ / α, presented in the form of equation (5), when the vessel enters circulation with simultaneous rotation of the rudder blade β_R and braking of the right propelling motor. The calculations were carried out for maneuvers at the relative initial speed of the vessel $v_{prim} = 1.0$ and $v_{prim} = 0.8$. Table 1 shows a small number of options for combinations of α_L, α_R, N_X, β_R and optimal solutions for performing the maneuver by the criterion of minimum $W_{C\min}$.

Table 1

Combinations of significant parameters and optimal solutions for the criterion of minimum energy consumption $W_{C\min}$

Option	Numerical values of parameters, p.u.					$W_{Cclassic}$, p.u.	Optimal solutions				Efficiency, %
							equation $\gamma = \gamma(\alpha)$			$W_{C\min}$, p.u.	
	v_{prim}	α_L	α_R	N_X	β_R		k_2	k_3	k_4		
1	1,0	1,0	0,8	0,12	0,262	16,67	2,08	−1,15	2,38	15,37	7,8
2	0,8	0,8	0,65	0,12	0,262	15,09	2,97	−2,39	1,71	10,86	28,03
3	0,8	0,8	0,55	0,12	0,262	13,16	3,24	−2,62	1,16	9,352	28,94
…	…	…	…	…	…	…	…	…	…	…	…
14	0,8	0,8	0,65	0,165	0,4	11,0	3,47	−3,089	1,342	7,93	27,91
15	0,8	0,8	0,55	0,165	0,4	9,7	3,27	−2,67	1,21	6,88	29,07
…	…	…	…	…	…	…	…	…	…	…	…
25	1,0	1,0	0,8	0,21	0,576	9,95	2,73	−0,07	−2,66	9,13	8,2
26	0,8	0,8	0,65	0,21	0,576	9,09	2,56	0,08	−2,27	6,93	27,51
27	0,8	0,8	0,55	0,21	0,576	8,02	3,2	−2,57	1,26	5,71	28,8

In Fig. 4, as an illustration, graphical interpretations of the control signal (5) are given with the optimal values of the coefficients k_2, k_3, k_4 for the first three options (from Table 1) combinations of parameters α_L, α_R, N_X, β_R are presented.

To assess the effectiveness of optimization, the corresponding maneuvers were calculated when controlling the propulsion electric motors and according to the classical proportional law. The results of calculating the energy consumption for performing

maneuvers according to this law are given in the $W_{Cclassic}$ column of the Table 1. The last column of the table illustrates the efficiency of optimization – the degree to which energy costs are reduced when switching to optimal control. Depending on the conditions of maneuvering, it ranges from 8 % to 29 %.
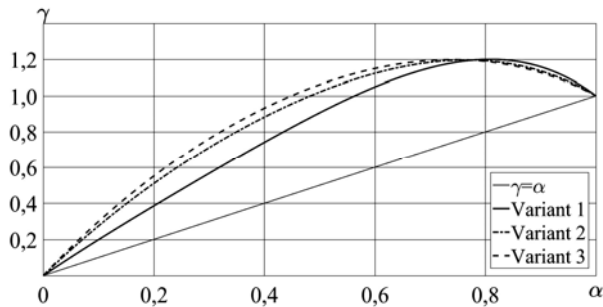

Fig. 4. Dependencies $\gamma = \gamma (\alpha)$ according to the criterion of minimum energy consumption W_{Cmin}

A lower degree of efficiency corresponds to the movement of the vessel at a higher speed, and a higher efficiency – when moving at a lower speed and maximum braking by the propelling motor (it should be borne in mind that the degree of braking is limited by the hydrodynamic characteristics of the propeller). Thus, the transition to optimal control of the PM (and the joint maneuvering by the motors and the rudder is most often carried out precisely at the partial motion of the vessel) significantly reduces the energy consumption W_C for the maneuver, which confirms its expediency.

Change in the optimality criterion leads, as expected, to other optimal solutions. Table 2 shows the results of optimization calculations according to the criterion of minimum run-out of the electric ship L_{1min} when it enters circulation. As can be seen from the table, the numerical values of the coefficients k_2, k_3 and k_4 differ significantly from those obtained by the criterion of the minimum energy consumption.

Figure 5 shows graphical interpretations of control signals with optimal values of the coefficients k_2, k_3, k_4 for the same first three (as in Table 1) options for parameters α_L, α_R, N_X, β_R combinations.

Table 2

Combinations of significant parameters and optimal solutions for the criterion of minimum run-out of the electric ship L_{1min}

| Option	Numerical values of parameters, p.u.					$L_{1classic}$, p.u.	Optimal solutions				Efficiency, %
							equation $\gamma = \gamma (\alpha)$			L_{1min}, p.u.	
	v_{prim}	α_L	α_R	N_X	β_R		k_2	k_3	k_4		
1	1,0	1,0	0,8	0,12	0,262	7,03	3,32	−7,58	2,33	6,62	5,8
2	0,8	0,8	0,65	0,12	0,262	6,28	3,54	−7,96	3,55	5,62	10,5
3	0,8	0,8	0,55	0,12	0,262	5,8	3,8	−8,6	2,1	5,36	7,6
…	…	…	…	…	…	…	…	…	…	…	…
17	0,8	0,8	0,65	0,21	0,4	4,9	3,51	−7,9	2,2	4,56	6,9
…	…	…	…	…	…	…	…	…	…	…	…
25	1,0	1,0	0,8	0,21	0,576	4,15	3,57	−8,23	2,27	3,94	4,6
26	0,8	0,8	0,65	0,21	0,576	4,137	3,72	−8,57	2,05	3,85	9,7
27	0,8	0,8	0,55	0,21	0,576	4,06	3,87	−8,79	2,01	3,72	8,3
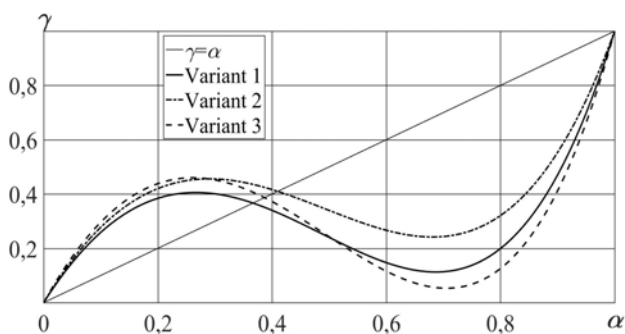
Fig. 5. Dependencies $\gamma = \gamma (\alpha)$ according to the criterion of minimum run-out of the electric ship L_{1min}

Analysis of these dependencies shows the following. Since, simultaneously with the rudder blade shifting, the braking of the right propeller motor is performed, the loads on this PM increase. In addition, the internal PM propeller begins to operate in a water flow with a larger bevel angle (Fig. 1), which leads to an increase in its drag moment.

This does not affect the operating performance of the generating sets, since they are covered by cross-links, and this is reflected in the performance of propulsion electric motors, since their power circuits are independent of each other. Internal PMs are loaded more and their performance indicators can approach the setpoints for the operation of protection systems.

To prevent the emergency shutdown of the PM (such maneuvers are carried out, as a rule, in order to prevent collision of ships), it is necessary to reduce the voltage value, which should be done by the automatic control system in accordance with the calculated optimal laws. This can be seen in Fig. 5.

To evaluate the efficiency of optimization (as for the $W_{Cclassic}$ option in Table 1), Table 2 shows the results of calculating the run-out of an electric ship when controlling propeller motors also according to the classical proportional law. The results of calculations according to this law are given in the $L_{1classic}$ column. The efficiency of optimization – the degree of decrease in the run-out of the electric ship varies depending on the

conditions of maneuvering from 5 % to 11 %. As in the previous case, a greater degree of efficiency is obtained when the vessel is moving at intermediate speeds.

To illustrate the behaviour of the propulsive complex after optimization of control laws, Fig. 6 shows the current values of the main performance indicators when performing the same maneuver as in Fig. 3. This is option No. 27 of a combination of significant parameters and conditions for performing the maneuver (Table 2) The selected option is an example of average efficiency.

Comparative analysis of the calculation results shows that with the transition to optimal control, the run of the electric ship (the criterion of optimality) decreased from 4.06 to 3.72 of the length of the vessel, which is 8.3 %. The numerical values of the main performance indicators when controlling according to proportional and optimal laws are also given in Table 3.

Thus, the transition to optimal control of the PM can significantly reduce the run-out of the electric ship, which contributes to the increase in the safety of maneuvering operations.

Discussion. The studies carried out clearly show that the traditional control of propelling electric motors does not allow to fully realize the high maneuverability inherent in electric ships.
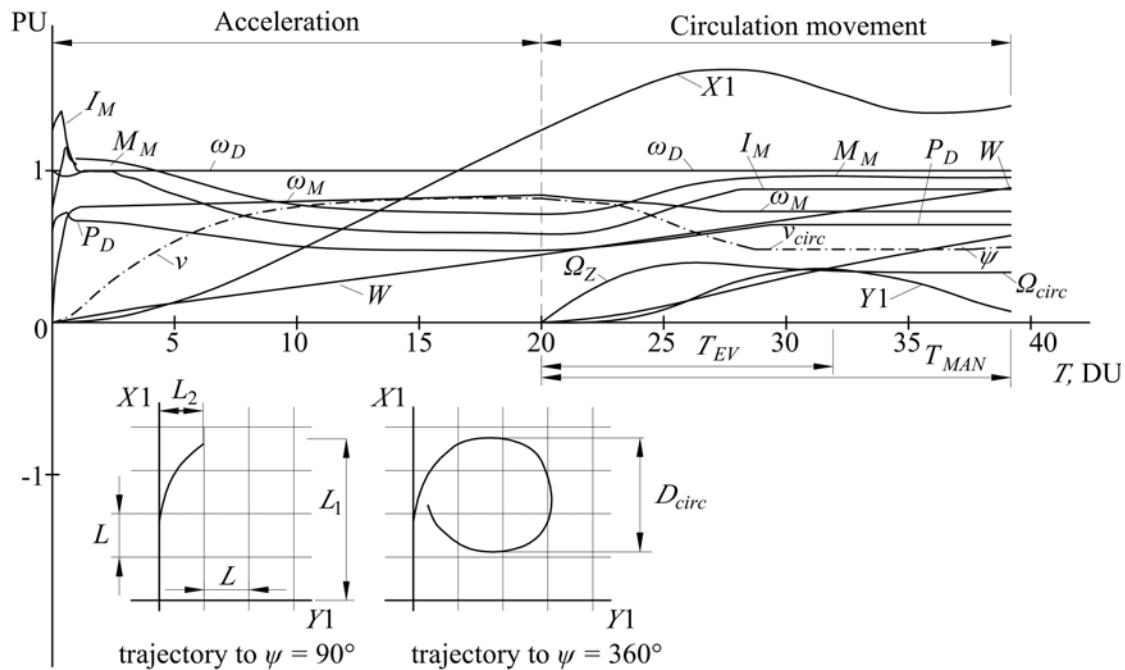

Fig. 6. Current values of the main operating parameters of the maneuver «acceleration of the EPP – exit to circulation» under optimal control low

Table 3

Indicators of the quality of maneuvering under different control laws

Quality indicator	Proportional low	Optimal low	Indicator deviation, %
T_{MAN}	20,5	19,2	+6,3
T_{EV}	13	11,9	+8,4
W	23,5	22	+6,8
L_1	4,06L	3,72L	+8,3
L_2 (ψ=90°)	1,32L	0,98L	+25,8
D_{circ}	3,22L	2,63L	+18,3
I_M	0,83	0,88	–6
M_M	0,92	0,96	–4,3
ω_M	0,79	0,73	–7,6
v_{circ}	0,56	0,48	–14,3

The reason is that the classical proportional control law, obtained in relation to the «electrical» indicators of the quality of electric motors, does not take into account the performance of the vessel. But propelling electric motors are designed precisely to ensure the best quality indicators of the ship's operation, in particular, its best maneuverability and high economic performance. We need a systematic approach to control the PM during maneuvers. In this case, «electrical» indicators should recede into the background. It is necessary to find such a control that will provide the best performance of the electric ship, with the controlled performance of its propeller electric power plant.

The solution of such problems is possible only with an integrated approach. The propeller electric power plant should be considered together with all the components of a single ship propulsion complex, which includes, in addition to the EPP, also propellers, a rudder and a hull of the ship. The presence of a mathematical model describing the behavior of the propulsive complex during maneuvers, a method for calculating the current values of the main performance indicators, and a correct (suitable for solving such problems) optimization method allows achieving this goal.

As shown in this work, with the correct organization of the propulsion electric motors control, it is possible to achieve the best values of the quality indicators of maneuvers and ensure, at the same time, the operation of

all the components of the propulsion electric power plant in permissible modes.

Conclusions.

1. The expediency of using a systematic approach in the search for optimal control of propelling electric motors of electric ships when maneuvering on a curvilinear trajectory has been substantiated. As the main criteria of optimality indicators ones characterizing the maneuverability of the vessel should be taken. The performance indicators of the EPP should be considered as constraints.

2. The disadvantages of the «classical» version of the EPP control have been grounded. A method is proposed for generating control signals for the EPP, with a simultaneous shift of the rudder blade, when the vessel enters circulation. A procedure for optimizing the parameters of control signals has been developed.

3. Optimization calculations were carried out and the optimal parameters of control signals for propelling motors were found. Optimization was carried out according to the criterion of the minimum energy consumption for performing the maneuver and according to the criterion of the minimum run-out of the electric ship. Optimization efficiency ranges from 5 % to 29 %.

REFERENCES

1. Molland A. *The maritime engineering reference book. A guide to ship design, construction and operation.* Butterworth-Heinemann, Oxford, UK, 2008. 920 p. **doi: doi:10.1016/b978-0-7506-8987-8.x0001-7.**

2. Bertram V. *Practical Ship Hydrodynamics.* Butterworth-Heinemann, Oxford, UK, 2012. 390 p. **doi: 10.1016/C2010-0-68326-X.**

3. Carlton J.S. *Marine propellers and propulsion. 4th edition.* Butterworth-Heinemann, Oxford, UK, 2018. 609 p. **doi: 10.1016/C2014-0-01177-X.**

4. Nebesnov V.I. Engine dynamics in the ship hull-propeller-engine system. Leningrad, Sudpromgiz Publ., 1961. 374 p. (Rus).

5. Leonhard W. *Control of electrical drives.* Springer-Verlag Berlin Heidelberg, 2001. 241 p. **doi: 10.1007/978-3-642-56649-3.**

6. Bose B.K. *Power electronics and AC drives.* Prentice Hall, Englewood Cliffs, New York, 2001. 738 p.

7. Mohan N., Undeland T.M., Robbins W.P. *Power electronics, converters, applications and design.* J. Wiley, New York, 2003. 811 p.

8. Yarovenko V.A., Chernikov P.S., Varbanets R.A., Zaritskaya E.I. Optimal control of the electric ships' propulsion motors during reversal. *Electrical engineering & electromechanics*, 2018, no. 6, pp. 38-46. **doi: 10.20998/2074-272X.2018.6.05.**

9. Chernikov P.S., Yarovenko V.A., Zaritskaya E.I. The influence of control laws of frequency-regulated electric motors on electric ships' maneuvering characteristics. *Bulletin of NTU «KhPI». Series: «Electric machines and electromechanical energy conversion»*, 2020, no. 3 (1357), pp. 45-51. (Ukr). **doi: 10.20998/2409-9295.2020.3.08.**

10. Yarovenko V.A., Chernikov P.S. A calculation method of transient modes of electric ships' propelling electric plants. *Electrical engineering & electromechanics*, 2017, no. 6, pp. 32-41. **doi: 10.20998/2074-272X.2017.6.05.**

V.A. Yarovenko[1]*, Doctor of Technical Science, Professor,*
P.S. Chernikov[1]*, Candidate of Technical Science,*
E.I. Zaritskaya[1]*, Candidate of Technical Science, Associate Professor,*
A.N. Schumylo[1]*, Candidate of Technical Science, Associate Professor,*
[1] Odessa National Maritime University,
34, Mechnikova Str., Odessa, 65007, Ukraine,
e-mail: yarovenko@3g.ua, chernikov@onmu.odessa.ua,
zarickayalena@ukr.net, shumilo.alexander@gmail.com

D.G. Koliushko, S.S. Rudenko, S.V. Kiprych

ANALYSIS OF THE STATE OF THE EXTERNAL LIGHTNING PROTECTION SYSTEM FOR OPERATING ENERGY OBJECTS

Introduction. Within the framework of European integration of Ukraine, the international Standard IEC 62305 has been harmonized, which provides for a full inspection of lightning protection devices with a frequency of 0.5 – 4 years, which significantly increases the volume of work. Problem. The adopted Standard is stricter than those for which external lightning protection systems (LPS) of power plants and substations, which are objects of critical infrastructure, have been designed. There is no clear algorithm of actions to bring the existing LPS of existing energy facilities of Ukraine in accordance with the requirements of IEC 62305. Due to the need to modernize the existing LPS facilities, there is a need to develop a single algorithm for these works. Goal. Development of an algorithm for evaluation of the current state LPS for existing power plants and substations. Methodology. Based on the analysis of IEC 62305, three stages of evaluation are proposed: experimental (based on geodetic and electromagnetic method of determining the configuration of the object and components of LPS), calculation (based on the topographic survey method and the electromagnetic method for determining the configuration of the object and components of the LPS) and stage of analysis and development of recommendations. Results. Three stages, which are a basis of analysis of a condition of LPS based on the created algorithm, are considered in detail. An example of the analysis LPS condition of the existing substation with a voltage of 35 kV, created according to the specified method, is given. The program report in 3D form illustrates the unprotected parts of the object. Originality. For the first time, an algorithm for analysis the state of LPS of operating energy facilities according to the IEC 62305 standard has been developed. Practical value. Typical remarks to the existing LPS are formed. The results of the work can be used to inspection and modernize the LPS energy facilities, as well as buildings and structures of public importance. References 18, tables 1, figures 3.
Key words: **lightning protection, protection zone, lightning rod, energy facility, rolling sphere method.**

В роботі запропоновано алгоритм аналізу стану системи блискавкозахисту (СБЗ) діючих енергооб'єктів, який складається з трьох етапів: експериментального (на основі топографічного та електромагнітного методу визначення конфігурації об'єкту й компонентів СБЗ), розрахункового (визначення зони захисту стандартним електрогеометричним методом) й етапу аналізу та розробки рекомендацій. До існуючих СБЗ сформовано типові зауваження та заходи щодо їх усунення відповідно до вимог ДСТУ EN 62305. Результати роботи можуть бути використані для перевірки та модернізації СБЗ складних промислових та енергетичних об'єктів, а також будівель і споруд загальносуспільного значення. Бібл. 18, табл. 1, рис. 3.
Ключові слова: **блискавкозахист, зона захисту, блискавкоприймач, енергооб'єкт, метод сфери, що котиться.**

В работе предложен алгоритм анализа состояния системы молниезащиты (СМЗ) действующих энергообъектов, состоящий из трех этапов: экспериментального (на основании топографического и электромагнитного метода определения конфигурации объекта и компонентов СМЗ), расчетного (определение зоны защиты стандартным электрогеометрическим методом) и этапа анализа и разработки рекомендаций. К существующим СМЗ сформулированы типовые замечания и меры их устранения в соответствии с требованиями ДСТУ EN 62305. Результаты работы могут быть использованы для проверки и модернизации СМЗ сложных промышленных и энергетических объектов, а также зданий и сооружений общественного назначения. Библ. 18, табл. 1, рис. 3.
Ключевые слова: **молниезащита, зона защиты, молниеприемник, энергообъект, метод катящейся сферы.**

Analysis of publications. Within the framework of European integration measures, in Ukraine the international Standard on lightning protection was harmonized [1], the requirements of which differ significantly from the Standards of the USSR [2] and Ukraine [3], according to which the design and control of the lightning protection system (LPS) of the vast majority of existing strategic energy facilities in Ukraine have been carried out.

According to [1] the LPS should be inspected:
- during installation of the LPS;
- after installation of the LPS;
- systematically, according to Table 1.

The time intervals listed in Table 1, should be applied in the absence of additional instructions of regulatory documents.

The frequency of inspection of the LPS is determined taking into account the following factors:
- classification of the protected object (power plant, substation, etc.), especially taking into account possible damages;
- LPS class;
- environment depending on the degree of its aggressiveness;
- material of individual components of the LPS;
- soil characteristics and degree of corrosion;
- weather conditions (changes in temperature and precipitation);
- changes in the parameters of the grounding device (GD) depending on humidity and temperature (e.g. resistance).

Table 1
Maximum interval between LPS inspections, year

Protection level	Visual audit	Full audit	Critical situations (full inspection)
I and II	1	2	1
III and IV	2	4	1

Note. In buildings where there is a possibility of an explosion, inspections should be carried out every six months. Critical situations may include buildings (structures) that contain sensitive internal systems, office buildings, commercial buildings, or places where a significant number of people may be present.

The LPS should also be inspected on an ongoing basis if significant changes have been made or the protected object has been reconstructed, as well as after lightning discharges.

The harmonized International lightning protection Standard [1] has more stringent requirements for lightning rods (LRs) protection zones than [2], [3] and other design requirements.

In this regard, the **urgent problem** is to inspect the LPS of existing energy facilities for compliance with the norms. The normative document itself specifies the parameters that need to be checked, but there is no explanation of the sequence and methods of verification.

In addition, the analysis of the state of LPS of complex objects, which are power plants and substations, is practically not considered. On their territory there is a large number of LRs of different types (rods, cables, nets), which create a connection between them. In addition, lightning protection of energy facilities is a strategic task, because the failure of equipment can lead to both costly repairs and significant losses from power outages of important consumers.

The analysis of the existing literature, in particular [4-8], shows that the assessment of the current state of the LPS of energy facilities in the form of a clear sequence of interrelated methods of inspection of the LPS is absent. Usually, publications are devoted to the calculation of LR protection zones or the design of LPS in accordance with [1].

The goal of the work is to develop an algorithm for assessing the current state of the LPS of existing power plants and substations.

Research materials. Due to the fact that the implementation of the inspection of the LPS [1] includes field and in-house work, and the main result is the development of recommendations for the arrangement of the LPS in accordance with regulatory requirements, the analysis of the current state of the SBZ is presented in three stages:

• obtaining initial data on the arrangement of the existing LPS (experimental stage performed in the field);

• determination of the level of the LPS and calculation of protection zones (PZs) of lightning rods (calculation stage);

• analysis of the existing LPS and development of necessary measures for protection of the object with minimization of material and labor costs (stage of analysis and development of recommendations).

Consider each of the stages of the analysis of the LPS more in detail.

1. Experimental stage. The lightning protection system consists of lightning rods, current collectors and GD.

During this stage, the following is determined:
1) geometric configuration of the LPS and the protected object;
2) general condition of LPS components (configuration, material, cross-section, quality of electrical connections, corrosion level);
3) value of the equivalent resistivity of the soil;
4) resistance of the GD of the LR with a separate ground rod.

For the listed items it is necessary to carry out field works on restoration (creation) of executive documentation. This is due to the long-term operation of the facility, during which it undergoes significant changes (installation of the communication masts, damage to the structure of the LR, expansion of the facility, corrosion infuence, etc.) and the loss of executive documentation.

When determining item 1 of the experimental stage, measurements of the geometric configuration of the protected object and the LPS by topographic surveying methods (for example, by theodolite one) are carried out [9]. The overall dimensions and height are marked on the map at a scale convenient for further work. The biggest difficulties of this item are:

• need to determine and further take into account the difference in ground level and height of parts of the object and the LPS relative to it;

• presence of high-rise buildings outside the facility, which may create additional PZ.

The work according to item 2 of the experimental stage is performed using:

• direct measurements with a caliper (cross-section of LPS conductors);

• induction method (GD configuration);

• ammeter-voltmeter method (quality of electrical connections).

Figure 1 shows a plan of the object with its LPS on the example of one of the substations with voltage class of 35 kV, which is the result of items 1, 2.

The work according to item 3 of the experimental stage is performed by the method of vertical electric sounding (using the Wenner or Schlumberger arrangement), and according to item 4 – by the ammeter-voltmeter method (by potential drop, four-point or «62% method») [10].

In general, the work for items 2 – 4 is performed according to the method described in [11] and according to the procedures described in [12].

All the difficulties of these substages correspond to the problems described in [13]. The most important of them:

• determining the condition of LPS conductors, such as current collectors, at a height near current carrying parts at power plants and substations (often in this case the only way to check is the use of photographic equipment, preferably with a long-focus lens);

• laborious work on finding grounding conductors in the soil and ways of lightning current spreading;

• practical complexity of identification of vertical electrodes and impossibility to determine their length and cross-section.

In addition, in [14] there is no concept of pulses resistance [15], in contrast to [1], so for it 4 the international method of determining the impedance using the appropriate devices considered, for example, in [16] should be used.

The results of measuring the geometric configuration of objects and their LPS are plotted on the diagram in electronic form. Data on deviations from the requirements of the Standard, changes and deformations of the LPS and any changes in the object must be recorded both in text form and with the help of photo and video equipment. The results of the experimental stage are recorded in the reporting documentation.
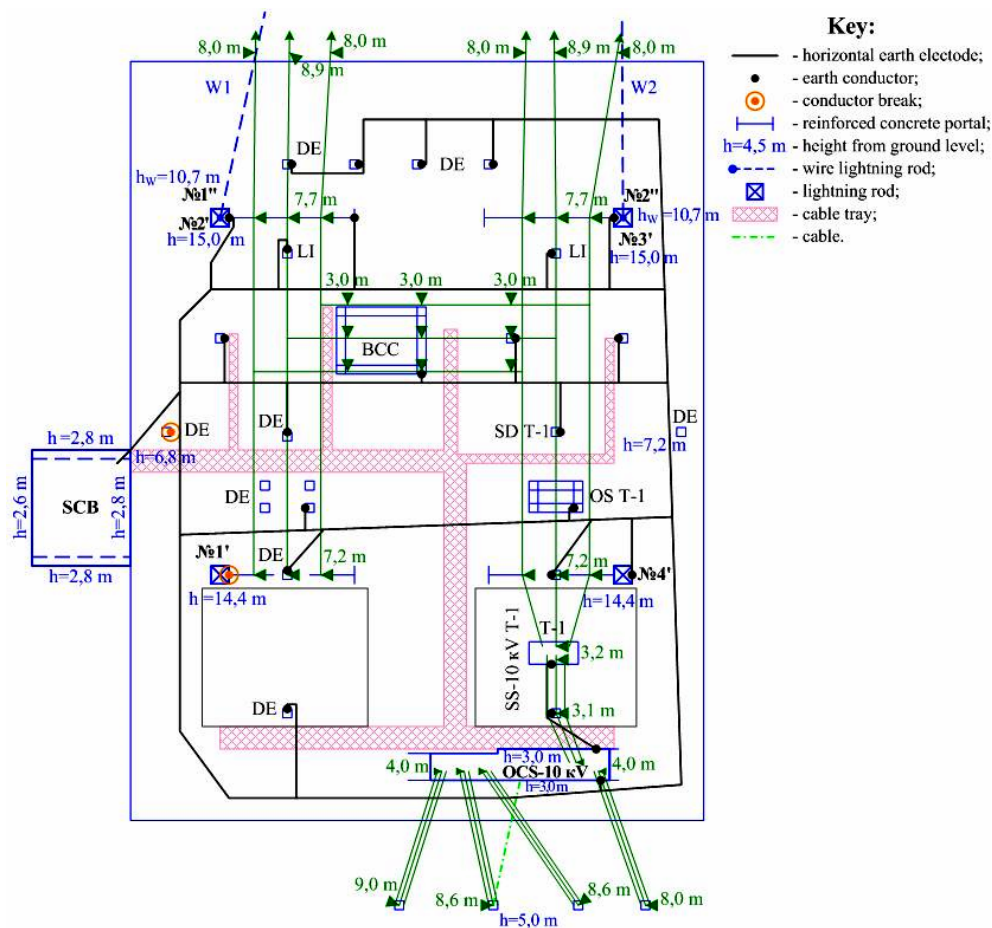
Fig. 1. Plan of the object and its LPS

2. Calculation stage. The calculation stage begins with determining the level of LPS, which is performed based on the calculation of the risk of lightning strikes to the object and the characteristics of the object. This is usually based on information provided by the operating organization and/or template calculations set out in some national annexes to IEC 62305 (e.g. in Germany).

Then, with the help of a special computer code, the calculation of the PZ of the LR is performed and the report is obtained in 2D and 3D form. To do this, first calculate the calculation scheme of the LPS is prepared, which includes the protected object. The scheme should take into account for the current time the following:

• LPS level (sphere radius is 20 m, 30 m, 45 m or 60 m for LPS of classes I, II, III or IV, respectively);

• location of the LR on the scheme (coordinates and height of each LR);

• location of buildings and structures of the protected object (coordinates and height).

To perform calculations, the method of determining the PZ of the LR using the rolling sphere method for one or 2-3 rod LRs of the same height [17] or computer codes to build the PZ of the LR of arbitrary heights and locations (e.g., Pentair, ERICO, Entegra, Primtech) can be used.

Experts of NTU «KhPI», using the mathematical apparatus given in [18], developed a computer system «LiGro», which is intended to calculate and design grounding and lightning protection systems. Regarding the calculation of the LPS the system consists of three logical parts:

• graphic editor, which allows to place on the scheme as many large numbers as you like of buildings, structures

and LR of any shape on a real scale using a graphical interface (location and size);

• 2D report, with which it is possible to analyze the results of the calculation of the PZ of the LR on the plane;

• 3D report for the analysis of the results of the calculation of the PZ of the LR in space.

Figure 2,a shows the object and its LPS in 3D, and in Fig. 2,b presents the result of the calculation of the PZ of the external LPS of the substation with the system «LiGro» in 3D in accordance with [1] and marks places that are outside the protection zone: 10 kV busbars (1); part of the fence (2); KRUZ-10 kV (3) and busbar 35 kV (4). Therefore, to protect the object from direct lightning strikes, it is necessary to develop recommendations (install additional LRs of the required height).

3. Stage of analysis and development of recommendations. The calculation scheme does not change if it is recommended to use only a protective grid made in accordance with the requirements of the regulatory document [1] to protect the object (or part of it).

If the object is not protected from direct lightning strikes, i.e. it or its parts are outside the PZ of the LR system, then the recommended LRs needed to protect the entire object should be added to the calculation scheme. The location, height and design of the recommended LRs should be chosen taking into account the economic feasibility and technical feasibility. Therefore, the development of recommendations for the installation of additional LRs is iterative in nature, aimed at finding optimal solutions: the installation, if possible, of typical LRs with the minimum required number and height. After

that it is necessary to check that all constructions are inside the PZ of the LR system, and also to analyze the constructive implementation of the LPS. If necessary, provide recommendations for bringing the constructive implementation of the LPS to the requirements of regulatory documents with the subsequent registration of all stages of work in the form of reporting documentation.

Thus, the assessment of the current state of the LPS of the existing energy facility can be represented as an algorithm (Fig. 3).
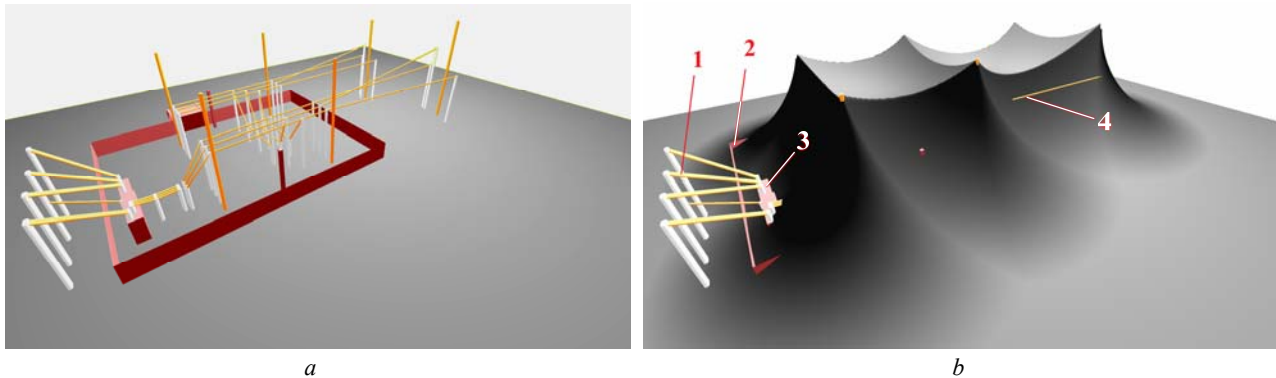

a   *b*
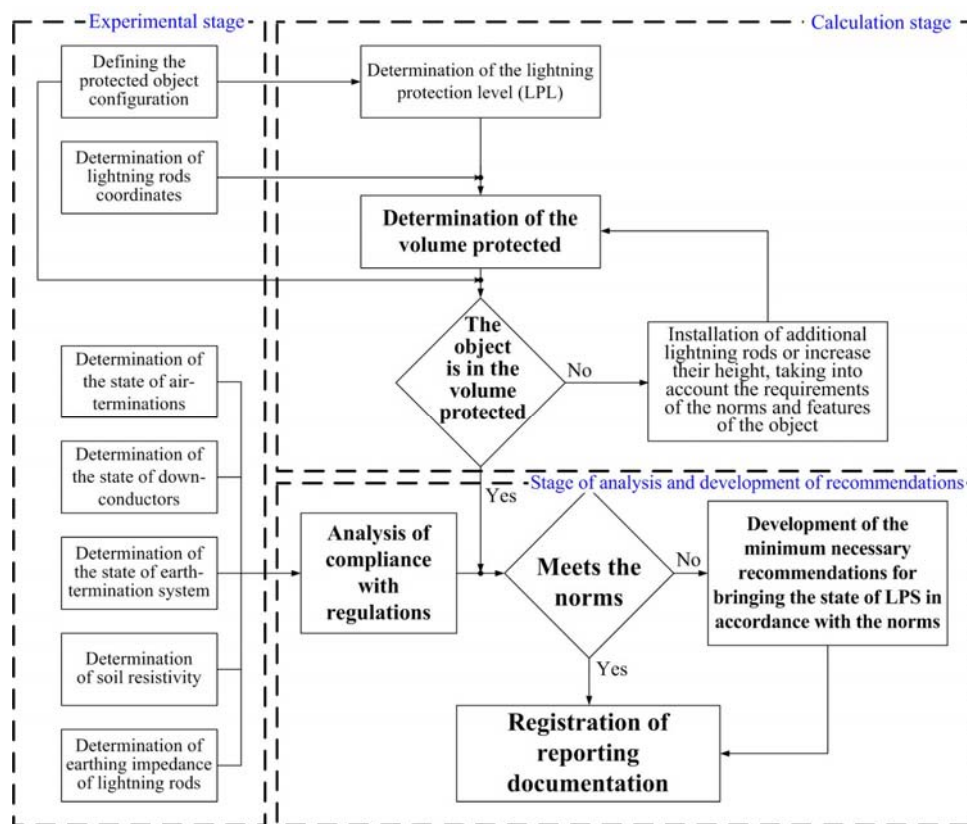
Fig. 2. Report in 3D

Fig. 3. Algorithm for estimating the current state of the LPS

The developed algorithm was successfully used at more than 200 power plants and substations of voltage classes of 35-750 kV. According to the results of the analysis of the current state of the LPS, standard remarks were formed to:

- security of objects (buildings and structures or their parts are outside the PZ of the LR; antennas and other communication devices that are sensitive to lightning surges, which are installed on lightning rods and buildings/structures that are not protected from direct lightning);
- lightning rods (the cross section is smaller 50 mm^2; no galvanic connection to the current drain; corrosion damage; deformation of the structure);
- current drains (no artificial current drains; the cross-section is less than 50 mm^2; the natural current drain has

no galvanic connection with the lightning rod and grounding device; corrosion damage);

- grounding device (resistance exceeds the regulated value; design and/or cross-section does not meet the requirements of regulatory documents);
- installation of lightning rods (performed in violation of the requirements of regulatory documents – the distance to the current carrying parts, grounded structures and grounding device of the substation is less than regulated one);
- electrical wiring (cables are laid in violation of regulatory requirements; cables from lighting equipment installed on the LR go to buildings/structures, which can lead to high potential during lightning strikes in the LR; cables that go from buildings/structures to the territory of the protected object, are outside the PZ of the LR, which

can lead to the entry of high potential into the building/structure during a lightning strike in these cables outside the territory of the protected object).

In order to eliminate remarks and bring the state of the LPS in accordance with the requirements of regulatory documents, the recommendations based on the results of the analysis of the state of the LPS of energy facilities may include the following items:

1. Installation of additional rod lightning rods or LRs of the required height:
- located separately;
- on portal constructions;
- on a building or structure.

2. Laying current leads from lightning rods to grounding conductors.

3. Ensuring galvanic connection of the cable lightning rod with the cable stand.

4. Laying additional horizontal grounding conductors in the recommended LRs to ensure the spread of lightning current by the grounding conductor in accordance with the requirements of regulatory documents.

5. Connection to the common GD of the substation of portal structures with rod and cable LRs, searchlight masts and lighting towers.

6. Connection to the common GD, if necessary, of the LR with a separate grounding conductor.

7. Installation of vertical electrodes in accordance with the requirements of regulatory documents.

8. To protect the buildings at the substation from direct lightning strikes – laying a protective net around the perimeter of the roof (as close as possible to its edge). To prevent thermal destruction of the roof waterproofing coating (roofing felt), it is recommended to secure the protective net conductors with roof holders (stands) made of heat-resistant material (e.g. concrete, clay, etc.).

9. Execution of electrical wiring to lighting equipment installed on floodlight masts in accordance with the requirements [14].

10. Replacement of corroded LPS components.

Then the results of all stages are systematized with registration in the form of documentation for external LPS (protocol, passport, report, etc.).

The documentation (in any form) must contain an explanatory note and graphic material.

Conclusions.

1. The paper describes for the first time the stages of analysis of the current state of the LPS of operating energy facilities of Ukraine and its components, an evaluation algorithm is developed, and methods for performing each of the stages are proposed.

2. The standard remarks to the LPS of the objects which are in operation are analyzed and systematized.

3. Possible measures are provided to eliminate the shortcomings identified in the process of analysis of the state of the LPS.

REFERENCES
1. State standard of Ukraine EN 62305:2012 Protection against lightning. (IEC 62305: 2011, IDT). Kyiv, State Standard of Ukraine, 2012. 419 p. (Ukr).
2. Guidelines for installation of lightning protection systems for buildings and structures (RD 34.21.122-87). Moscow, Energoatomizdat Publ., 1989. 56 p. (Rus).
3. DSTU B V.2.5-38:2008 Lightning protection device for buildings and structures (IEC 62305:2006 NEC). Kyiv, Minrehionbud Ukraine Publ., 2008. 63 p. (Ukr).
4. Lyutarevich A.G., Basmanovskiy M.A., Sershanskiy V.P., Zhilenko E.P. Investigation of lightning protection of open switchgears of power stations and substations. *Omsk Scientific Bulletin*, 2018, no. 162, pp. 61-66. **doi: 10.25206/1813-8225-2018-162-61-66.**
5. Dyakov A.F., Kuzhekin I.P., Maksimov B.K., Temnikov A.G. *Electromagnetic compatibility and lightning protection in the power*. Moscow, MEI Publishing House, 2009. 455 p. (Rus).
6. Rizk F.A.M. Modeling of substation shielding against direct lightning strikes. *IEEE Transactions on Electromagnetic Compatibility*, 2010, vol. 52, no. 3, pp. 664-675. **doi: 10.1109/TEMC.2010.2046903**.
7. Kazanskiy S.V, Maltsev V.V 3D-modeling of lightning Protection systems of electrical network. *Power engineering: economics, technique, ecology*, 2014, no. 4 (38), pp. 78-83. (Ukr).
8. Analysis of modern foreign and domestic experience in the installation of lightning protection systems of the electrical objects. Kyiv, National Power Company «Ukrenergo», 2012. 75 p. (Ukr).
9. Kern R. *Wissenschaftliche Instrumente in ihrer Zeit/Band 4: Perfektion von Optik und Mechanik*. Cologne, 2010, pp. 349-360. (Ger).
10. IEEE Std 81-2012 Guide for Measuring Earth Resistivity, Ground Impedance, and Earth Surface Potentials of a Grounding System. New York, IEEE, 2012. 86 p. **doi: 10.1109/ieeestd.2012.6392181**.
11. Koliushko D.G., Rudenko S.S. Analysis of methods for monitoring of existing energy objects grounding devices state at the present stage. *Electrical engineering & electromechanics*, 2019, no. 1, pp. 67-72. **doi: 10.20998/2074-272X.2019.1.11.**
12. National Standard of Ukraine SOU 31.2-21677681-19:2009. Test and control devices, electrical grounding. Standard instruction. Kyiv, Minenergovugillya Ukrayiny Publ., 2010. 54 p. (Ukr).
13. Koliushko G.M., Koliushko D.G., Rudenko S.S. On the problem of increasing computation accuracy for rated parameters of active electrical installation ground grids. *Electrical engineering & electromechanics*, 2014, no. 4, pp. 65-70. (Rus). **doi: 10.20998/2074-272X.2014.4.13**.
14. Electrical installation regulations. Kharkiv, Fort Publ., 2017. 760 p. (Ukr).
15. Grcev L., Markovski B. Impulse impedance and effective area of grounding grids. *IEEE Transactions on Power Delivery*, 2020, pp. 1-10. **doi: 10.1109/tpwrd.2020.3003427**.
16. Koliushko D.G., Rudenko S.S., Plichko A.V., Shcherbinin V.I. Modernization of the complex type IK-1U for measuring the impedance of the grounding device of a lightning arrester and supports of transmission lines. *Electrical engineering & electromechanics*, 2019, no.3, pp. 55-58. **doi: 10.20998/2074-272X.2019.3.09.**
17. Petcharaks N. Lightning protection zone in substation using mast. *KKU engineering journal*, 2013, vol. 40, no. 1, pp. 11-20. **doi: 10.5481/kkuenj.2013.40.1.2.**
18. Koliushko D.G., Istomin O.Y., Rudenko S.S., Kiprych S.V. Mathematical model of the protection zone during an arbitrary configuration of the air-termination rods location. *Technical Electrodynamics*, 2020, no. 1, pp. 3-9. (Ukr). **doi: 10.15407/techned2020.01.003.**

D.G. Koliushko[1], *Candidate of Technical Science, Senior Research Scientist,*
S.S. Rudenko[1], *Candidate of Technical Science, Senior Research Scientist,*
S.V. Kiprych[1],
[1] National Technical University «Kharkiv Polytechnic Institute», 2, Kyrpychova Str., Kharkiv, Ukraine, 61002,
e-mail: nio5_molniya@ukr.net

Передплатний індекс: 01216